POLITECNICO DI MILANO
Scuola di Ingegneria Civile, Ambientale e Territoriale
Corso di Laurea Magistrale in Ingegneria Civile

AN ENGINEERING APPROACH TO THE MULTISCALE MODELING OF THE LYMPHATIC SYSTEM

Relatore: Prof. Ing. Riccardo Sacco
Correlatore: Prof. Ing. Giovanna Guidoboni
Correlatore: Ing. Raul Pirovano

Tesi di laurea Magistrale di:
Nicholas Mattia Marazzi 883144

Anno accademico 2017/2018

Ringraziamenti

Desidero innanzitutto ringraziare il Professor Sacco. Gli spunti di riflessione e l'interesse suscitato dalle Sue lezioni sono state la spinta ad affrontare questo cammino di tesi e spero un giorno di poter fare tesoro dei preziosi insegnamenti ricevuti in questi mesi.

Vorrei ringraziare profondamente Giovanna. La tua guida scientifica e umana è stata per me un fondamentale riferimento e mi auguro di poter continuare ad apprendere con la stessa passione con cui mi hai seguito e accompagnato nelle sfide di questa ricerca.

Un ringraziamento va a tutto lo staff di XC-engineering, che ho avuto la fortuna di incontrare durante il tirocinio in cui si è ulteriormente sviluppato il presente elaborato. Vorrei in particolare ringraziare Raul, che mi ha affiancato e guidato alla conoscenza di FLOW-3D dedicando numerose ore allo sviluppo della tesi.

Questa tesi rappresenta il momento finale di un percorso iniziato cinque anni fa. Tale cammino non sarebbe stato possibile senza il supporto dei miei genitori, coloro che hanno vissuto più da vicino quest'avventura sostenendomi ed aiutandomi in ogni situazione. Spero un giorno di potervi restituire una piccola parte di tutto quello che avete fatto per me. Un ringraziamento speciale va a mia sorella Arianna, la persona che mi ha aiutato a ritrovarmi nei momenti più intensi e che continua ad insegnarmi con enorme semplicità la leggerezza delle emozioni. Vorrei che il giorno della laurea fosse presente mio nonno Oreste, la persona che con una frase mi ha fatto capire più di quanto avessi cercato di comprendere per anni. Alla nonna Angela, che tante volte mi ha aspettato e sopportato nei pomeriggi di studi con la sua incredibile gioia e gentilezza. Ai nonni Anna ed Arturo, con cui 18 anni fa muovevo i primi passi alle scuole elementari e che ancora sono vicini a me in ogni momento e in ogni nuova sfida.

Abstract

The lymphatic system constitutes a one-way transport route that operates in conjunction with the cardiovascular system. Its primary function is to maintain overall fluid balance in the human body. In this thesis, we develop two mathematical models, based on fluid-dynamic principles, to characterize the role of the lymphatic system in regulating fluid homeostasis. Although the lymphatic system has a vital role in human health, several mechanisms of this system still need to be elucidated.

Our current work is motivated by this limited knowledge as well as the repercussions of impaired lymphatic function, which can lead to pathological conditions such as lymphedema or tumor metastases. Mathematical models can be used as a virtual laboratory where hypotheses can be tested to advance the quantitative understanding of the lymphatic system.

In the first part of this thesis, we develop a lumped parameter model to simulate fluid balance in the human body. The challenges in the design of this model stem from the uncertainty affecting the physiological knowledge of the regulatory mechanisms of the lymphatic system. Thus, our virtual laboratory offers the possibility of formulating different hypotheses to verify the impact of the lymphatic system on a large scale. The proposed formulation reproduces the main features of the cardiovascular system and has the novelty of embedding both the filtration process and the lymphatic system into a systemic computational framework. Moreover, the model emphasizes the systemic importance of a component of the lymphatic system, known as lymphangions, in the controlled transport of fluid that the lymphatic system must accomplish to maintain homeostasis.

In the second part of the thesis, we analyze the behavior of the lymphangions at a finer scale resolution. To this purpose, we develop a CFD simulation with the commercial software ***FLOW-3D*** aimed at studying the fluid-dynamic behavior of this component. We analyze two different configurations. Initially, we studied a single lymphangion and highlight a tight relation between the time-rate of change of pressure stems and valve dynamics. Then, we study a scenario composed of several lymphangions with which we examined the fluid-dynamic quantities in a lymphangions chain and provide a theoretical explanation to justify the observed behavior.

Sommario

Il sistema linfatico costituisce una via di trasporto ad un solo verso che opera in collaborazione con il sistema cardiovascolare. La funzione principale di questo sistema è il mantenimento del volume ematico. In questa tesi vengono proposti due modelli matematici, basati su principi fluidodinamici, per la caratterizzazione del ruolo del sistema linfatico nella regolazione dell'omeostasi dei fluidi.
Il nostro lavoro attuale è motivato dalla limitata conoscenza dei meccanismi fisiologici dello stesso sistema e dalle ripercussioni di una funzionalità linfatica alterata, che può portare all'insorgenza di patologie come linfedema o metastasi tumorali. In tal senso, i modelli matematici possono essere utilizzati come un laboratorio virtuale in cui è possibile testare ipotesi per far aumentare la comprensione quantitativa del sistema linfatico.
Nella prima parte di questa tesi, viene sviluppato un modello a parametri concentrati per simulare il bilancio di fluidi nel corpo umano. La complessità nella definizione quantitativa di questo modello deriva dall'incertezza riguardo i meccanismi regolatori del sistema linfatico. Pertanto, il laboratorio virtuale offre la possibilità di formulare diverse ipotesi per verificare l'impatto del sistema linfatico su larga scala. Il modello proposto descrive le principali caratteristiche del sistema cardiovascolare, del processo di filtrazione e del sistema linfatico in un quadro computazionale sistemico. Questo modello enfatizza l'importanza sistemica di un componente del sistema linfatico, noto come linfangione, nel trasporto controllato del fluido che il sistema linfatico deve realizzare per mantenere l'omeostasi nel corpo umano.
Nella seconda parte della tesi viene analizzato il comportamento dei linfangioni ad una scala locale tridimensionale. A questo scopo, viene sviluppata una modello numerico CFD con il software commerciale FLOW-3D finalizzata allo studio del comportamento fluidodinamico di questo componente. Si sono considerate due diverse configurazioni. Inizialmente si è sviluppata una simulazione ad un unico linfangione con la quale si è evidenziato la dinamica delle pressioni e del movimento delle valvole. A partire dall'osservazione di questo modello, si sono simulate più linfangioni. E' stato così possibile osservare comportamento fluidodinamico in questa condizione e si è fornita una spiegazione teorica del comportamento osservato.

Contents

List of Figures

List of tables

CHAPTER 1
INTRODUCTION

1.1 An interdisciplinary approach to the modelling of the lymphatic system

Human body has two major circulatory systems: the cardiovascular and the lymphatic system. Although both systems were initially described by Hippocrates and share many functional, structural, and anatomical similarities, the understanding of each system proceeded at a very different rate [1].

While the cardiovascular system has been extensively studied, the lymphatic system has been largely neglected [2]. Even after its rediscovery in 1627, the latter system was considered a secondary vascular system supporting the cardiovascular system.

However, in the last decade, scientific attention to the lymphatic system has been growing due to the reevaluation of its essential role in human health and well-being. Interest in lymphatic research was boosted by the growing evidence that this system contributes to several diseases, such as lymphedema, cancer metastasis and different inflammatory disorders [1] [2] [3][4].

However, the physiological mechanisms of the lymphatic system are still unclear [1], [2], [4], [5] because of the difficulty of obtaining experimental measurements.

Few non-invasive methods have been developed to test human lymphatic activity [5] whereas the mouse has increasingly become the default animal model for lymphatic studies. Mouse lymphatic measurements have inspired several computational models [6] [7] [8] which are useful for investigating the physiological mechanisms of the lymphatic system.

Compared to an experimental set-up, a virtual laboratory has the capability of simulating multiple scenarios where all variables are under control and can be tested and, at the same time, it can help design new experimental tests to obtain data on which models can be validated.

For instance, due to the small dimension of lymphatic vessels (in the order of magnitude of mm) it is very complex to measuring the flow rate is very complex.
In this context, the target of our thesis is to develop two computational environments which enable us to study the fluid dynamic features of the lymphatic system as illustrated in Figure 1.1.

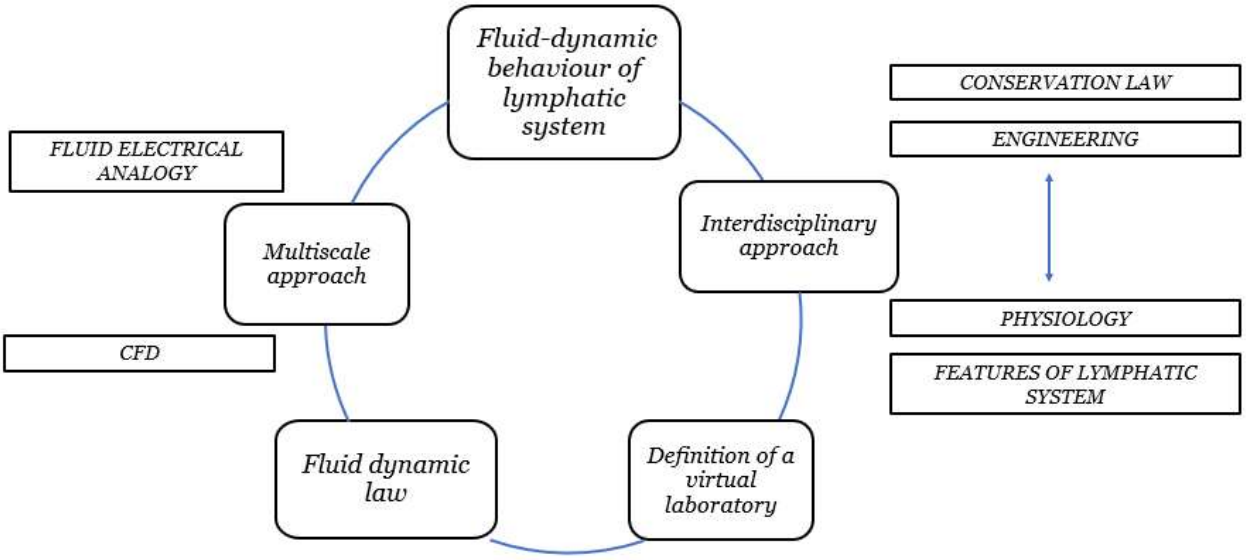

Figure 1.1: Conceptual structure of the problem of interest

To define the virtual laboratory, we consider an interdisciplinary approach involving both physiology and engineering.
In this chapter, we will provide an overview of the physiology of the lymphatic system, which is needed to define the theoretical basis of the problem as well as to elucidate challenges and open questions involved in its modeling.
Then, in Chapter 2, we will describe the mathematical framework of conservation laws of fluids on which our thesis is based. Specifically, we will describe two model reduction approaches of the latter equations which will provide two different perspectives of the problem at hand. In Chapters 3 and 4, we will consider a systemic perspective of the lymphatic at the scale of the human body employing a lumped parameter model based on fluid-electrical analogy. Based on the observations of this model, in Chapter 5 and 6, we will investigate the hydraulic behavior of a crucial component of the lymphatic physiology, called lymphangion, with a CFD approach. Finally, we will describe the conclusions and the perspectives of this work.

1.2 Lymphatic system

The lymphatic system is an organized network of several organs, tissues and vessels.
The lymphoid organs include the spleen, thymus and tonsils. Additional vital parts include the bone marrow, where white blood cells are produced, and lymph nodes, which are small bean-shaped glandular nodules where white blood cells can proliferate.

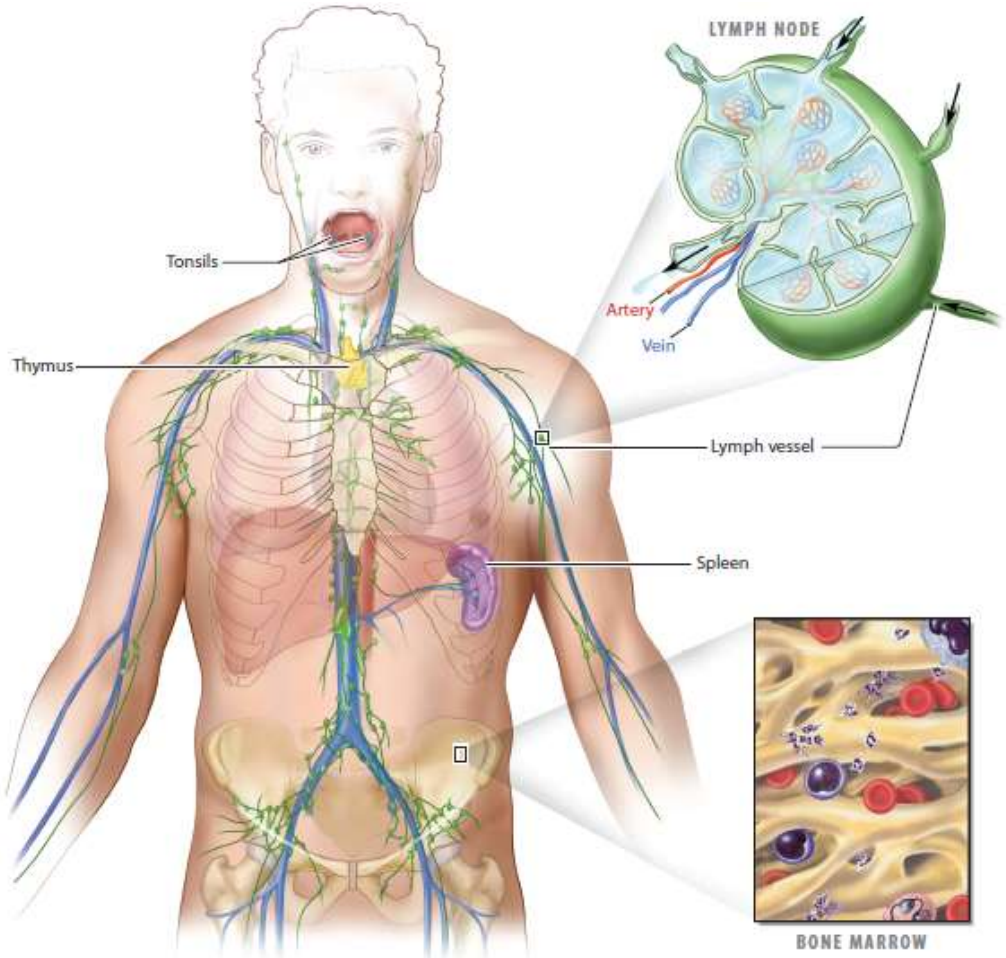

Figure 1.2: Lymphoid organs in the human body

The focus of this thesis is on the fluid-dynamic behavior of the lymphatic vascular system, which comprises a network of vessels extending to almost every organ, including the brain [4].
Lymphatic vessels carry lymph, which is a fluid containing mainly water, along with suspended proteins and immune cells. The anatomical region where lymph is formed is the intercellular space. Then, this network runs in parallel to the venous system and returns to the blood circulation through the thoracic ducts.
As can be observed in Figure 1.3, the cardiovascular system is a closed system where fluid leaves and returns from the same organ (the heart). Conversely, the lymphatic system begins at the interstitial space before returning to the blood circulation (it is called a blunt-ended linear system).

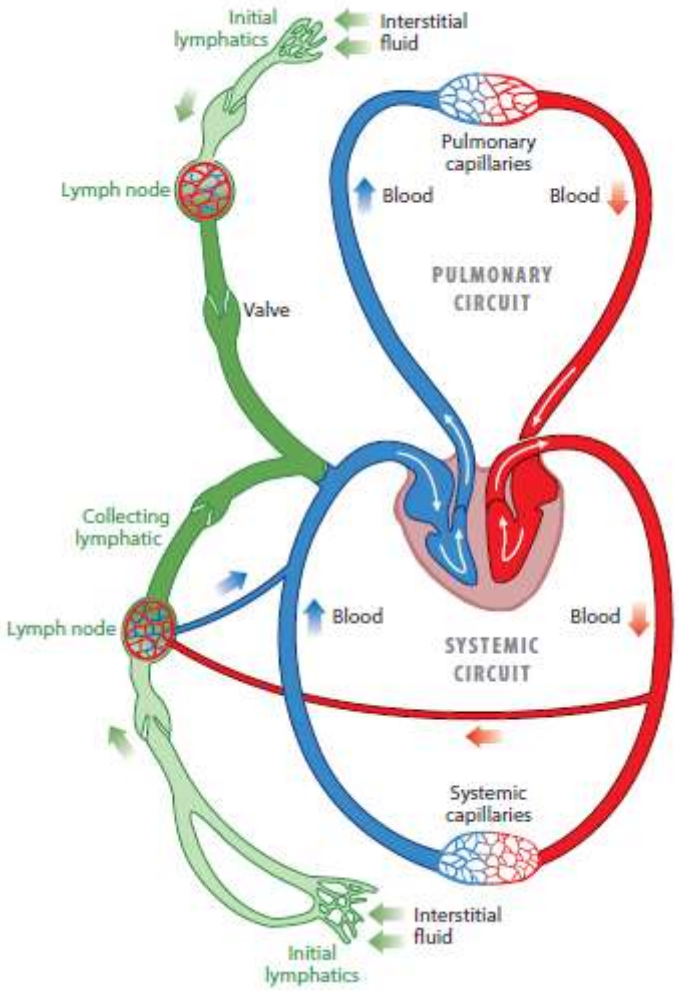

Figure 1.3: Schematic representation of the lymphatic system

1.2.1 Tasks of the lymphatic system

The lymphatic system was initially recognized solely as a network of transporting pathways for the removal of tissue products. After the discovery of the filtration process from the capillaries, the role of the lymphatic system in the maintenance of fluid-homeostasis by controlling extracellular fluid volume became more evident.

Specifically, the lymphatic system regulates both tissue fluid and transport of macromolecules, such as proteins, to blood, gathering them from the interstitial space and returning them to the blood system.

Owing to this function, Guyton defines the lymphatic system as a “scavenger” system [9]. Note that without the return of proteins to the blood from the interstitial space, we would die in 24 hours [9]. Moreover, although the lymphatic vasculature is not considered a formal part of the immune system, it is critical to immunity. One of its major roles is in the coordination of trafficking antigen and immune cells.

1.2.2 Lymphatic vascular system

The lymphatic transport system is composed of a hierarchy of vessels of increasing size which originates in the interstitial space with the initial lymphatic, or lymphatic capillaries, which are depicted in Figure 1.4.

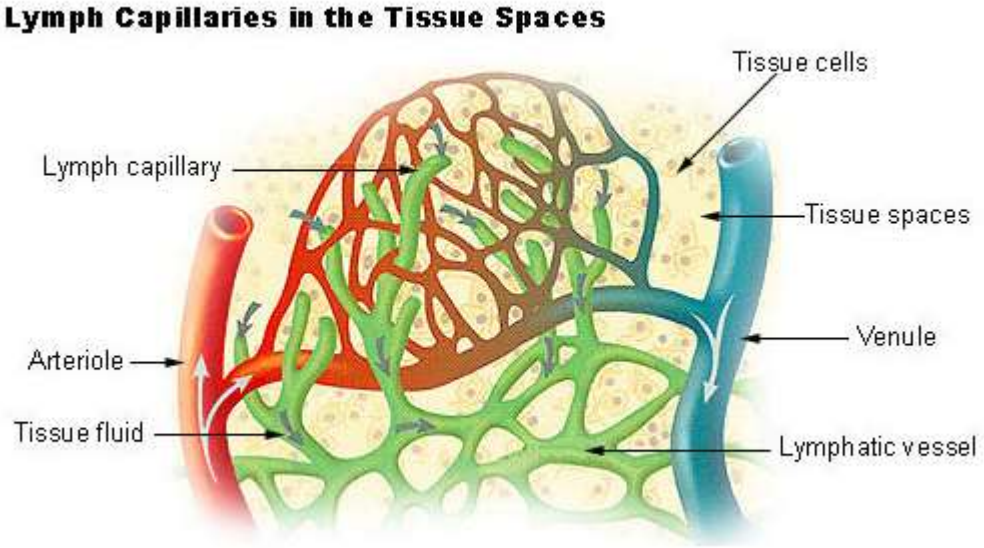

Figure 1.4: Lymphatic capillaries

Lymphatic capillaries are supported by anchoring filaments and function as a one-way valve system to prevent back-flow. The small lymphatic capillaries gradually combine to form larger diameter vessels, called pre-collectors. They contain layers of smooth muscle and are capable of performing spontaneous contraction. Furthermore, pre-collectors have the task of collecting substances from the interstitial space and propelling them towards larger vessels, called the collecting lymphatic.
The structure of the collecting lymphatic is similar to that of blood vessel, and they contain another type of valve, called the secondary valve. The segment of the collecting lymphatics between valves is termed lymphangion and is represented in Figure 1.5.

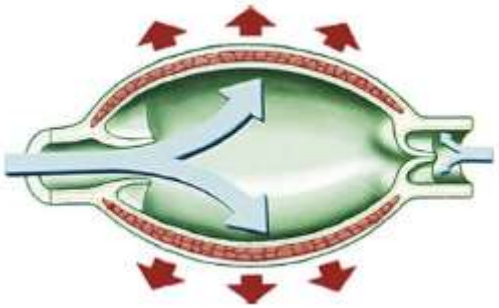

Figure 1.5: Lymphangion

The peculiarity of the latter element is that it can perform rhythmic contractions with which the lymph is propelled. Interestingly, the lymphatic transport system performs this pumping function in the absence of a central pulsatile organ.

1.2.3 Physiology of the lymphatic system

The lymphatic vascular system works in conjunction with the cardiovascular system and their relationship is schematically represented in Figure 1.6.

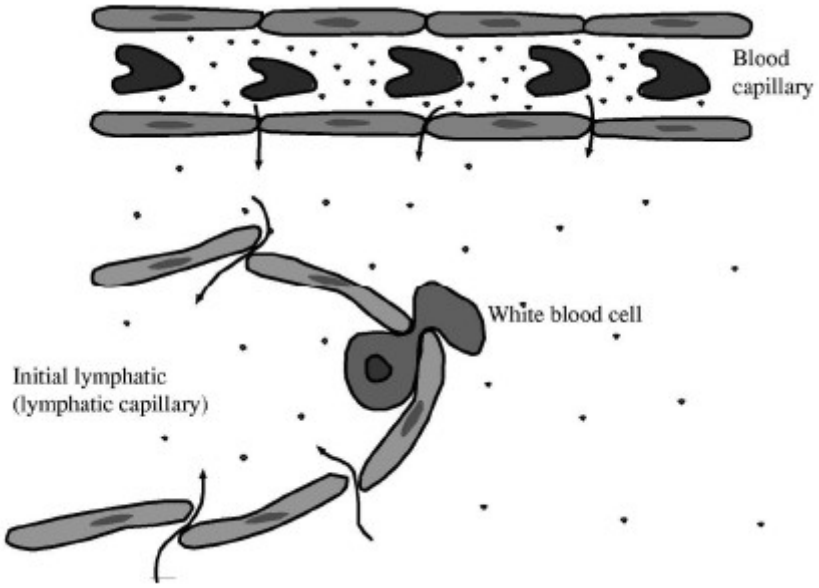

Figure 1.6: Relationship between the cardiovascular and the lymphatic system

As blood arrives at the capillary bed, it is forced out of the leaky barrier of these vessels.
Most of the exudate gets reabsorbed into the blood circulation, but there is an excess of fluid which filtrates into the interstitial space. For the maintenance of fluid homeostasis, this net flux must be acquired by the lymphatic system. Once the fluid enters the lymphatic system, it is propelled due to the rhythmic contraction of the lymphangions. The crucial importance of the contraction of lymphangions stems from the pressure boundary condition of the lymphatic flow pathways which can be observed in Figure 1.7.

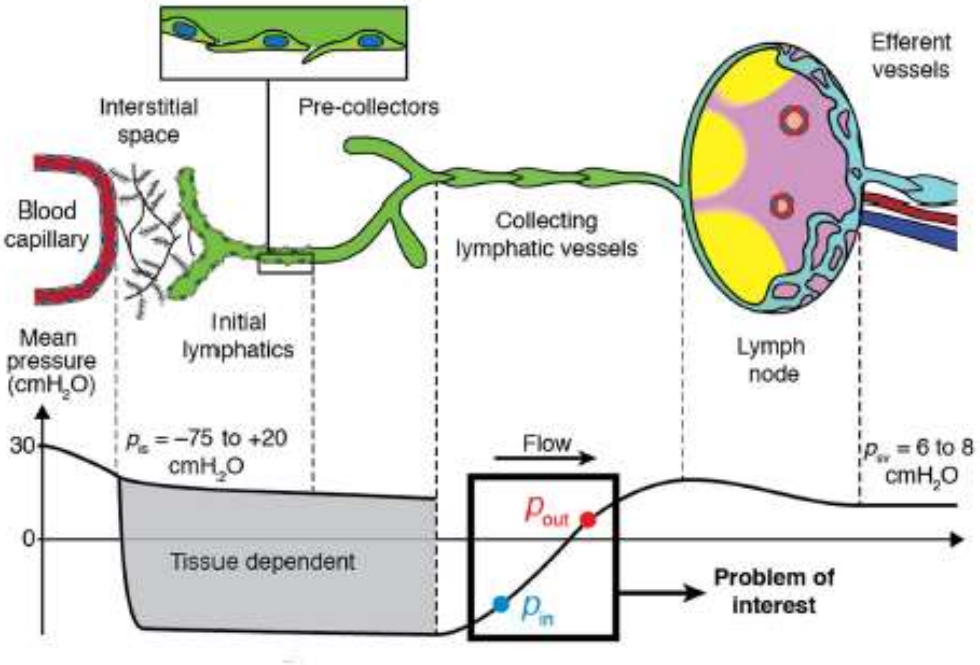

Figure 1.7: Lymph flow pathway from the interstitial space to the subclavian vein

The interstitial space represents the inlet of this network of vessels and is characterized by a subatmospheric pressure. In contrast, the outlet point of lymphatic vasculature is the venular side where pressure is positive (6-8 mmHg). Hence, a propulsion is needed to allow fluid movement against a hydrostatic pressure gradient.

The driving force is provided by the rhythmic contraction of lymphangions, whose effectiveness impacts not only the interstitial fluid but overall homeostasis [4][7].

Despite the crucial importance of this process, the physiological mechanisms underlying the contraction rate are still not completely elucidated in the literature. Similarly, also the process with which we have an uptake of interstitial fluid has been subject of much controversy [10].

1.3 Lymphatic system in diseases

In this section we illustrate several disorders in which lymphatic system is involved.

1.3.1 Lymphedema

One consequence of inadequate lymph transport is lymphedema. This disease is a progressive pathological condition of the lymphatic system leading to the accumulation of a protein-rich interstitial fluid in the tissue. It is a debilitating disease which significantly affects the quality of life. Lymphedema usually involves swelling of a limb, but other areas, including the head, neck and breast may be involved. It can be distinguished into primary lymphedema and secondary lymphedema.

The first occurs in childhood and leads to alterations in the structural features of the lymphatic system while secondary lymphedema stems from a complication of cancer treatment or parasitic infections, but it can also be linked to several genetic disorders.
Specifically, in advanced countries, the majority of secondary lymphedema is observed among cancer patients who undergo various radiation therapies. Although it is an essential practice, it inevitably destroys and obstructs lymphatic flows and thus exposes patients to a high increased risk of lymphedema. Studies report that 25%–56% of breast cancer patients develop mild-to-severe lymphedema after cancer treatment [1].
Although lymphedema has been described for centuries, there is no cure for lymphedema. Successful management of the disease, resulting in its limiting progression, can be achieved with early diagnosis. The therapies for lymphedema include massage, bandages, and, in the most severe cases, the surgical removal of the tissue.

1.3.2 Metastases

All of the deadliest forms of cancer spread because metastatic cells separate from the primary tumor and migrate to different locations of the body through the cardiovascular or lymphatic system. The immune system is capable of eliminating these rogue cells. Unfortunately, this defense system can be overwhelmed or subverted, resulting in the formation of secondary tumors in other parts of the body. These secondary tumors that are actually responsible for approximately 90% of cancer deaths [11].

1.3.3 Immune system disfunction

Transport along the lymphatic flow delivers crucial information to lymph node.
Without the lymph flow–mediated transport of immune cells and antigens, there could be no adaptive immunity in animals. Moreover, the physiological mechanism of the lymphatic system, such as the contraction, may play an integral role in the immune system as described in [12].

CHAPTER 2
GOVERNING EQUATIONS

The physical problem object of this thesis consists of investigating the fluid-dynamic behaviour in a biological system comprised of the lymphatic system in conjunction with the cardiovascular system within the human body. The biological system is schematically represented in Figure 2.1.

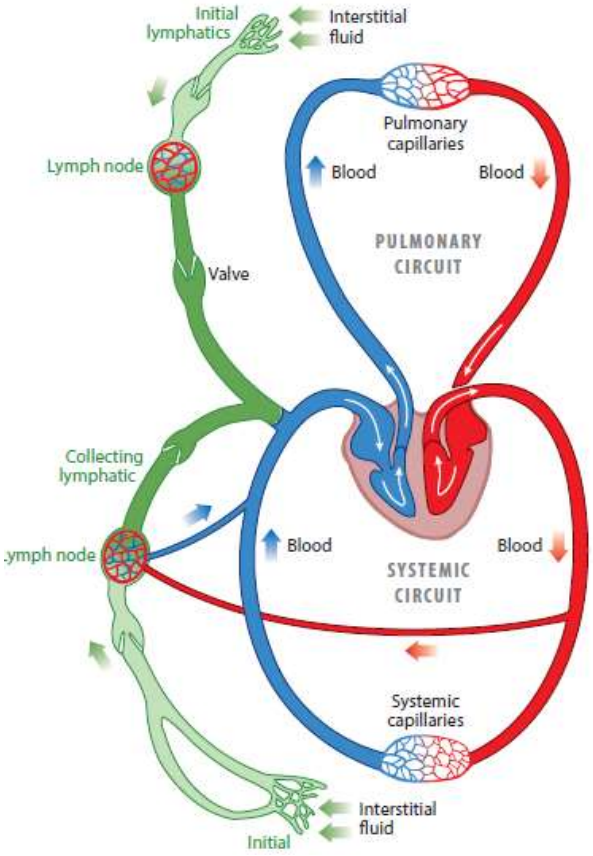

Figure 2.1: Cardiovascular and lymphatic system

In principle, to accomplish the target of this thesis we should study the following set of partial differential equations (PDEs).

$$\nabla \cdot \underline{v} = 0 \qquad \text{Eq(2.1)}$$

And

$$\frac{\partial \underline{v}}{\partial t} + \rho \underline{v} \cdot \nabla \underline{v} + \nabla p - \boldsymbol{div}(\mu \underline{\underline{\boldsymbol{D}}}(\underline{v})) = f \qquad \text{Eq(2.2)}$$

The Eq(2.1) is referred to as the mass conservation law and Eq(2.2) as the linear momentum balance law. The system of Eq(2.1) and Eq(2.2) is a closed set of equations whose unknowns are the three components of the fluid velocity $\underline{v}$ and pressure p.
The solution of model Eq(2.1)-Eq(2.2) at the scale of the human body is unaffordable by a computational point of view. Hence, we will consider two model reduction approaches at two different scale to reduce the computational complexity of the problem.

2.1 Lumped parameter model

In this section, we define the governing equations of the lumped parameter model, which can be derived by general conservation principles. In section 2.1.1, we will initially describe the one dimensional (1D) conservation equation. Then, we derive the governing equations of the lumped parameter model and the fluid-electric analogy.

2.1.1 One-dimensional conservation equation

Figure 2.2 represents a simple compliant tube considered as a model of a human vessel. We assume that the axis of the vessel is rectilinear and coincides with the x-axis.

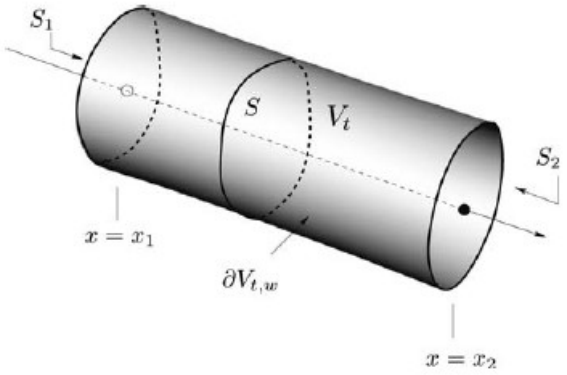

Figure 2.2 *Compliant tube*

Our goal is to obtain a one-dimensional form of mass and momentum balance along the x-axis.
The starting point for the derivation of the one-dimensional governing equation is Reynolds' transport theorem. If we consider an arbitrary control volume Vt with boundary ∂Vt and outer normal n, the one-dimensional transport theorem for a continuous function *f* reads as [13]

$$\frac{\partial(\overline{f}\,A)}{\partial t}+\frac{\partial}{\partial x}\left[(\overline{fv_3}\,A)\right]=\int_S\left[\left(\frac{\partial f}{\partial t}(\underline{x},t)\right)+\nabla\cdot(f\underline{v})\right]d\sigma+\int_{\partial S}\rho(\underline{w}\cdot\underline{n})d\gamma \qquad \text{Eq(2.3)}$$

where

- $\overline{f}$ is the area-averaged value of f

$$\overline{f}=\frac{1}{A}\int_S f\,d\sigma \qquad \text{Eq(2.4)}$$

- A is the cross-section area

$$A=A(x,t)=\int_S d\sigma \qquad \text{Eq(2.5)}$$

- $\overline{v_1}$ is the area-averaged value of the x-component of the velocity

$$\overline{v_1}=\frac{1}{A}\int_S v_1\,d\sigma \qquad \text{Eq(2.6)}$$

If we assume that the lumen is impermeable, i.e. $\underline{w}\cdot\underline{n}=0$ we get

$$\frac{\partial(\overline{f}\,A)}{\partial t}+\frac{\partial}{\partial x}\left[(\overline{fv_1}\,A)\right]=\int_S\left[\left(\frac{\partial f}{\partial t}(\underline{x},t)\right)+\nabla\cdot(f\underline{v})\right]d\sigma \qquad \text{Eq(2.7)}$$

One-dimensional conservation of mass is obtained considering by setting $f=\rho$ in Eq(2.7), namely

$$\frac{\partial(\overline{\rho}\,A)}{\partial t}+\frac{\partial(\overline{\rho v_1}\,A)}{\partial x}-\int_S\left[\left(\frac{\partial\rho}{\partial t}(\underline{x},t)\right)+\nabla\cdot(\rho\underline{v})\right]d\sigma=0 \qquad \text{Eq(2.8)}$$

If we assume that the density is constant and that the fluid is incompressible, i.e. $\nabla\cdot\underline{v}=0$, we get

$$\frac{\partial A}{\partial t}+\frac{\partial(\overline{v_1}\,A)}{\partial x}=0 \qquad \text{Eq(2.9)}$$

Similarly, one-dimensional momentum balance is obtained by setting $f=\rho v_1$ in Eq(2.7). The formal derivation is provided [13] [14] [15], here we report the result

$$\frac{\partial(\overline{v_1}\,A)}{\partial t}+\frac{\partial(\overline{v_1^2}\,A)}{\partial x}=\frac{A}{\rho}\left(\rho\overline{f_1}^{b}-\frac{1}{\rho}\left(\frac{\partial\overline{p}}{\partial x}\right)+\overline{d_1}\right) \qquad \text{Eq(2.10)}$$

where

- $\overline{f_1}^{b}$ represents the z-component of the external force;
- $\overline{d_1}$ d1 is the x-component of $\boldsymbol{d}$, where $\underline{\boldsymbol{d}}=\nabla\cdot\underline{\underline{\boldsymbol{D}}}$ and $\underline{\underline{\boldsymbol{D}}}$ represents the deviatoric stress tensor.

The system of the above one-dimensional equations can be rewritten as

$$\begin{cases} \dfrac{\partial A}{\partial t} + \dfrac{\partial(\overline{v_1}A)}{\partial x} = 0 \\ \dfrac{\partial(\overline{v_1}A)}{\partial t} + \dfrac{\partial(\overline{v_1^2}A)}{\partial x} = \dfrac{A}{\rho}\left(\rho\overline{f_1}^{b} - \left(\dfrac{\partial\overline{p}}{\partial x}\right) + \overline{d_1}\right) = 0 \end{cases} \qquad \text{Eq(2.11)}$$

The unknowns in the system are p, A and $\overline{v_1}$. Their number exceeds the number of equations and a common way to close the system is to find a relationship between pressure and area of the vessels [15].

2.1.2 Zero-dimensional equation

The governing equations of a lumped parameter model can be derived by averaging the 1D models. We will firstly reformulate Eq(2.11) by adding some hypotheses and modifying the notation.
Specifically:

- we will assume that external forces are negligible ($\overline{f_1}^{b} = 0$);
- area averaged velocity and pressure will be denoted as v and p respectively.

Moreover, we define the mass flux across a section as

$$Q = \int_S v_1 d\Omega = A\overline{v_1} = Av \qquad \text{Eq(2.12)}$$

Introducing the above notation into Eq(2.11) yields:

$$\begin{cases} \dfrac{\partial A}{\partial t} + \dfrac{\partial Q}{\partial x} = 0 \\ \dfrac{\partial Q}{\partial t} + \dfrac{\partial(\overline{v_1^2}A)}{\partial x} + \dfrac{A}{\rho}\left(\dfrac{\partial p}{\partial x}\right) + \overline{d_1}\dfrac{Q}{A} = 0 \end{cases} \qquad \text{Eq(2.13)}$$

Considering the blood vessels represented in Figure 2.2, we define its length as $l = |x_2 - x_1|$, we can define the mean volumetric flow rate over the whole vessel as

$$\hat{Q} = \frac{\rho}{l}\int_{\Omega} v_1\, dV = \int_{x_1}^{x_2}\int_S v_1\, dS = \frac{\rho}{l}\int_{x_1}^{x_2} Q(x)\, dx \qquad \text{Eq (2.14)}$$

Similarly, we define the mean pressure and area over the vessel as

$$\hat{p} = \frac{1}{l}\int_{x_1}^{x_2} P\, dx \qquad \text{Eq (2.15)}$$

$$\hat{A} = \frac{1}{l}\int_{x_1}^{x_2} A\, dx \qquad \text{Eq (2.16)}$$

Integrating the continuity equation along the axial direction, we obtain

$$l\frac{d\hat{A}}{dt} + Q_2(t) - Q_1(t) = 0 \qquad \text{Eq (2.17)}$$

Regarding the momentum equation, we add the following simplifying assumptions:

- the contribution of the convective term $\frac{\partial(\overline{v_1^2}A)}{\partial x}$ can be neglected [13], [15];
- the variation of A with respect to x is small compared to that of P and Q. We can replace A with a constant value for the area that in general is assumed to be the area at rest A_0.

Averaging along x direction we get

$$\frac{d\hat{Q}}{dt} + \frac{\overline{d_1}}{A_0}\hat{Q} + \frac{A_0}{\rho}(P_2(t) - P_1(t)) = 0 \qquad \text{Eq (2.18)}$$

where

$$P_1(t) = P_1(t, x_1) = 0 \qquad \text{Eq (2.19)}$$

Hence, the zero-dimensional format of the mass and balance conservation reads as

$$\begin{cases} l\frac{d\hat{A}}{dt} + Q_2(t) - Q_1(t) = 0 = 0 \\ \frac{d\hat{Q}}{dt} + \frac{\overline{d_1}}{A_0}\hat{Q} + \frac{A_0}{\rho}(P_2(t) - P_1(t)) = 0 \end{cases} \qquad \text{Eq(2.20)}$$

We again have again problem of closing the system by adding a wall mechanics law.
For instance, we can consider the relation proposed by [15]

$$\frac{d\hat{A}}{dt} = k_1\frac{d\hat{p}}{dt} \qquad \text{Eq (2.21)}$$

where

- $K_1 = \frac{\sqrt{A_0}}{\beta}$
- $\beta = \frac{\pi h_0 E}{(1-\nu^2)A_0}$

we get

$$\begin{cases} lk_1\frac{d\hat{p}}{dt} + Q_2(t) - Q_1(t) = 0 = 0 \\ \frac{d\hat{Q}}{dt} + \frac{\overline{d_1}}{A_0}\hat{Q} + \frac{A}{\rho}(P_2(t) - P_1(t)) = 0 \end{cases} \qquad \text{Eq(2.22)}$$

2.1.3 Fluid electric analogy

Equations such as Eq(2.22) are also found in the analysis of electrical circuits.
As a matter of fact, the fluid-dynamic behaviour of both cardiovascular system [16][22] and lymphatic system [18] has been studied relying on electric circuit analogs.
The advantage of this approach is that we can solve the fluid-dynamic behaviour of a hydraulic system exploiting Kirchhoff's laws of voltage and currents leading to a system of ordinary differential equation

(ODEs). Specifically, in this analogy, the blood (or lymph) flow rate is assimilated to the current, while pressure corresponds to voltage.

Starting, from this analogy, we can rewrite Eq(2.22) as

$$\begin{cases} C\dfrac{\partial \hat{p}}{\partial t} + Q_2 - Q_1 = 0 \\ L\dfrac{\partial \hat{Q}}{\partial t} + R\hat{Q} + P_2 - P_1 = 0 \end{cases} \qquad \text{Eq(2.23)}$$

where the coefficient R, L, C are associated to the following electric elements:

- C is the capacitance and it is associated with the capacitor represented in Figure 2.3

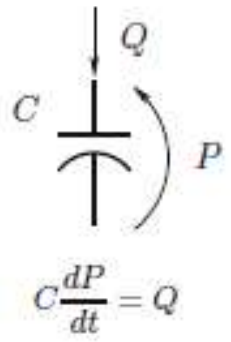

Figure 2.3: Capacitor

Specifically, based on fluid-electric analogy the capacitance C is defined as

$$C = k_1 l \qquad \text{Eq (2.24)}$$

and represents the mass storage term in the mass conservation law due to the compliance of the vessel.

- R is the resistance as depicted in Figure 2.4

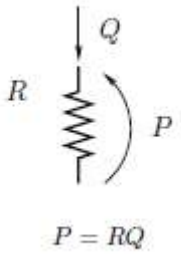

Figure 2.4: Resistor

It is defined as

$$R = \frac{\overline{d_1}}{{A_0}^2} \qquad \text{Eq (2.25)}$$

and represent the resistance exerted by blood viscosity to fluid flow. Different expression of R can be found according to the definition of the component d1 of the deviatoric stress tensor. For

instance, if we assume Poiseuille flow and that the vessel is a cylinder of constant circular cross section we have

$$R = \frac{8\pi\rho\nu l}{\pi^2 r_0^4} \qquad \text{Eq (2.26)}$$

- L is the inductance and it is associated to the inductor represented in Figure 2.3

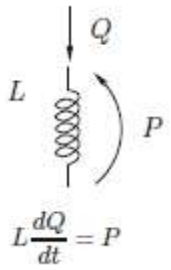

Figure 2.5: Inductor

It is defined as

$$L = \frac{\rho l}{A_0} \qquad \text{Eq (2.27)}$$

and represents the inertial term in the momentum equation.

2.2 THE CFD APPROACH

In section 2.1 we showed the lumped model parameter reduction. This approach has the advantage to provide a systemic discretization of the problem of interest. Another typology of model reduction is based on a CFD approach, where the target is a discretization of the equation system (2.1) – (2.2) at a local scale to investigate the fluid-dynamic behaviour of the problem at hand. Specifically, we will use a CFD commercial software, called ***FLOW-3D*** (described in Chapter 5), based on the finite volume that is described below.

We consider the balance law of the scalar quantity $u = u(x,t)$

$$\frac{\partial u}{\partial t} + \nabla \cdot \underline{F}(u) = \beta \qquad \text{Eq (2.28)}$$

The flux $\underline{F}$ accounts for two contributions

$$\underline{F}(u) = \underline{F}_{adv}(u) + \underline{F}_{diff}(u) \qquad \text{Eq (2.29)}$$

where

$$\underline{F}_{adv}(u) = \underline{v} \cdot u \qquad \text{Eq (2.30)}$$

and

$$\underline{F}_{diff}(u) = -D\,\nabla u \qquad \text{Eq (2.31)}$$

The flux Eq(2.30) is an advective flux whereas Eq(2.30) is a diffusive flux, and D js the diffusion coefficient.

The model Eq(2.29)- Eq(2.30)- Eq(2.31) is the scalar version of the flux in the momentum balance equation Eq(2.2) written in the conservative form. The function $\beta = \beta(x,t)$ is the net production rate.
The balance law Eq(2.28), with the constitutive relations Eq(2.29)- Eq(2.30)- Eq(2.31), must be solved in a domain $\Omega_t \subseteq \mathbb{R}^d$, d =1,2,3, and in a time interval $I_T = (0,T)$, $T > 0$ supplied by initial and boundary condition.
To proceed with the finite volume method we assume that Ω is a polygon in $\mathbb{R}^2$ and we partition Ω into a finite number of rectangular elements K

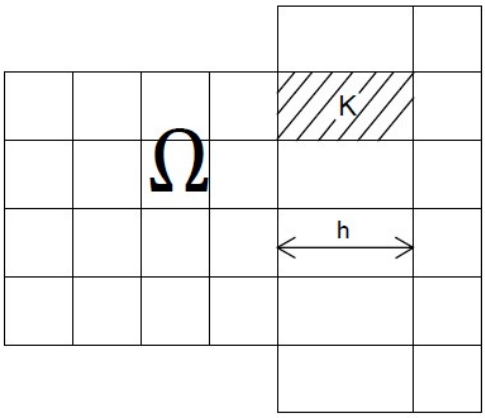

Figure 2.6: Computational domain Ω and partition ζ_h

We denote by ζ_h the minor of the element K, $h > 0$ being the discretization parameter. This latter is defined as the longer edge of ζ_h
Then we integrate the balance law Eq(2.28) over each element K

$$\int_K \frac{\partial u}{\partial t} dK + \int_K \nabla \cdot \underline{F}(u)\, dK = \int_K \beta\, dK \qquad \forall K \in \zeta_h \qquad \text{Eq (2.32)}$$

This is the integral form of the balance law over the element K.
The second integral on the left-hand side of Eq(2.32) is treated using the divergence theorem to obtain:

$$\int_K \frac{\partial u}{\partial t} dK + \int_{\partial K} \underline{F}(u|_{\partial K})) \cdot \underline{n}_{\partial K}\, d\gamma = \int_K \beta\, dK \qquad \forall K \in \zeta_h \qquad \text{Eq (2.33)}$$

where $\underline{n}_{\partial K}$ is the outward unit normal vector on ∂K and $u|_{\partial K}$ is the restriction of u to the boundary ∂K (see Figure 2.7).

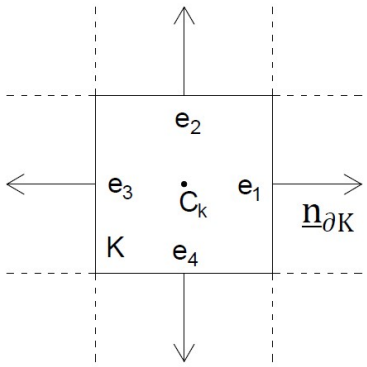

Figure 2.7:The element K and outward normal

The finite volume method is the numerical approximation of Eq(2.33) and is constructed by replacing $u|_K$ with a constant u_h^K the source term β with its value β_K at the baricenter C_k and the normal component of $\underline{F}$ on each edge $e_i, i = 1,..,4$ with the constant f_i where

$$f_i = f_i\,(u_h^k, u_h^{k_i}) \qquad \text{Eq (2.34)}$$

K_i being one of the four neighbouring element of K with respect to the edge e_i.
The finite volume formulation leads to the following system of ordinary differential equation

$$\frac{du_h^k}{dt} \cdot |k| + \sum_{i=1}^{4} f_i\,(u_h^k, u_h^{k_i}) \cdot |e_i| = \beta^K |k| \qquad \forall K \in \zeta_h \qquad \text{Eq (2.35)}$$

that has to be integrated on the time interval I_T, given an initial datum $u_{h,0}^k$, $\forall K \in \zeta_h$, the boundary condition and a constitutive equation for f_i.
System Eq(2.35) is the analog of the equation system of ODEs Eq(2.22) in the case of the model balance law.The approach discussed above is implemented in the package ***FLOW-3D*** and we refer to [Manuale FLOW-3D] for a documentation on the software.
We refer to [47] for a general description of the approximate normal component f_i and the analysis of the scheme.

CHAPTER 3
A SYSTEMIC LUMPED PARAMETER MODEL OF FLUID BALANCE IN THE HUMAN BODY

The aim of the first part of the thesis is to develop a numerical environment to study the role played by the lymphatic system in maintaining a homeostasis condition in the human body. To pursue this target, we will provide a systemic description of human fluid balance which will constitute the global framework to investigate the impact of the lymphatic system. Owing to the scale of the problem, the adopted formulation is a lumped parameter model of the cardiovascular and lymphatic system based upon the equivalence of fluid and electric variable described in Chapter 2.
Concerning the cardiovascular system, we will illustrate a possible electric description of the arterial and venous network and of the heart. Then, we will describe the numerical implementation of the proposed formulation of the cardiovascular system with two different software (MatLab and OpenModelica).
Finally, we will introduce the electric counterpart of both filtration process and the interstitial space, which will enable us to characterize lymphatic system and study human fluid balance in Chapter 4.

3.1 Lumped parameter modeling of fluid balance in the human body

In this chapter we illustrate the features of the computational environment to study the interaction between the lymphatic system and the cardiovascular system. These two systems work in conjunction to maintain a homeostasis condition in the global balance of fluid circulating in the human body and they are the key components of our model.

3.1.1 Structure of the model

A lumped parameter model of a hydraulic system is based on the key concept of compartment, which is a spatially homogeneous unit function of the sole time variable and characterized by a pressure and a flow rate. The model proposed in the present thesis comprises eight connected compartments, as depicted in Figure 3.1. Specifically, the compartment of heart, arteries, veins and capillaries describe the cardiovascular system whereas the interstitial space and the lymphatic system define the systemic microcirculation. Overall, each compartment collaborates in maintaining human fluid balance.

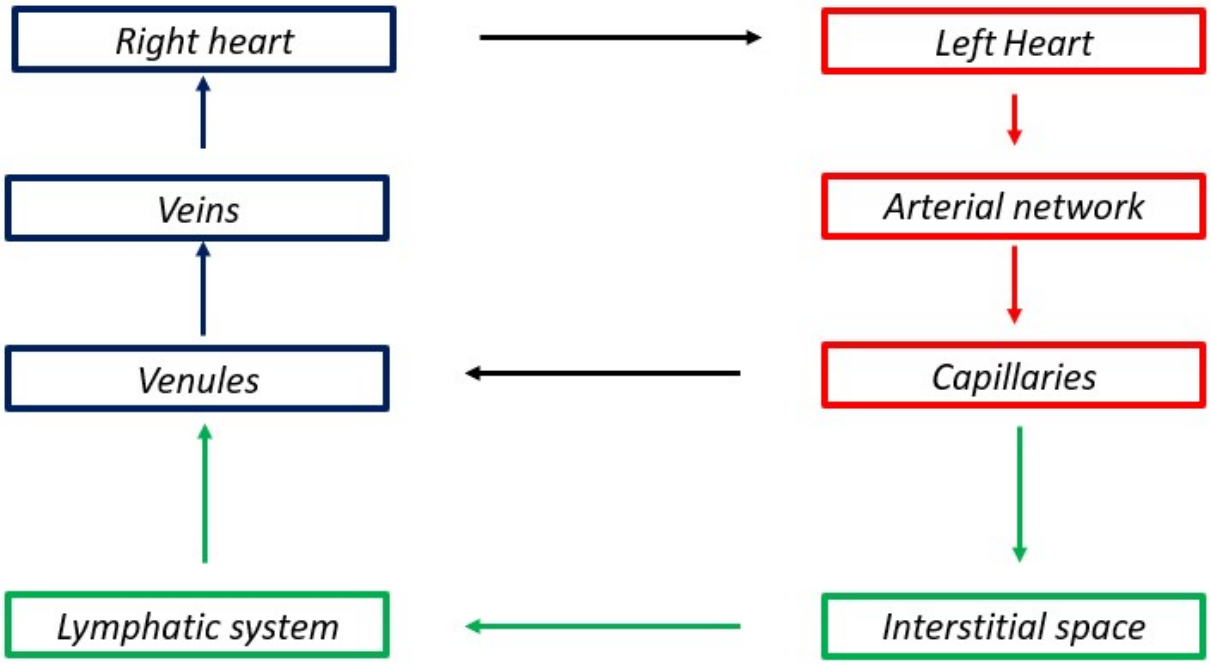

Figure 3.1:Block diagram of the proposed model of human fluid balance

The hemodynamic features of each compartment in the scheme of Figure 3.1 can be described with a combination of electrical elements based on the fluid-electric equivalence already treated in Chapter 2. Moreover, the block diagram depicted in Figure 3.1 is the mathematical counterpart of the cardiovascular system and lymphatic system illustrated in Figure 3.2.

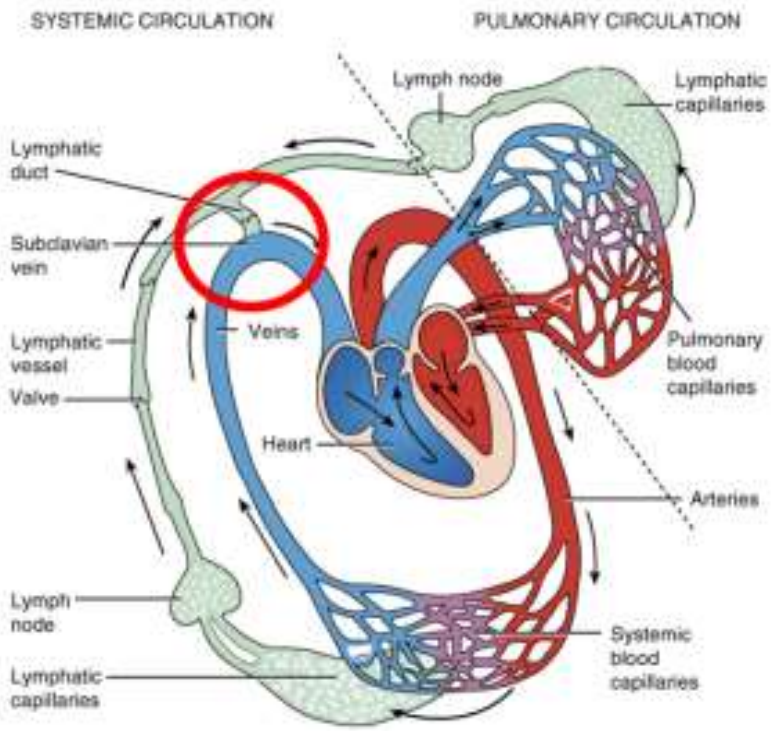

Figure 3.2:Cardiovascular and Lymphatic system

The objective of these chapters is the definition and the calibration of a proper representation of the physiology of each compartment to construct a model comprising of:

- Cardiovascular system;
- Filtration/reabsorption process taking place at the capillary side of systemic circulation;
- Interstitial space.

This formulation will represent fluid balance in a healthy physiological condition.
In the next section we present a review of the lumped parameter modeling of the arterial and venous tree, that will be used to develop the global lumped model describing human fluid balance.

3.1.2 Single and multi-compartment models of arterial and venous trees

The cardiovascular system has been the first element of human physiology studied with electric components since the 19th century. Frank Windkessel in 1899 formulated the first model, called 2 element WK, to describe the hemodynamic property of arterial network [19]. The model comprises a resistor connected in parallel with a capacitor, as depicted in Figure 3.3. It accounted for the total resistance of the systemic vasculature and the elasticity of large arteries.

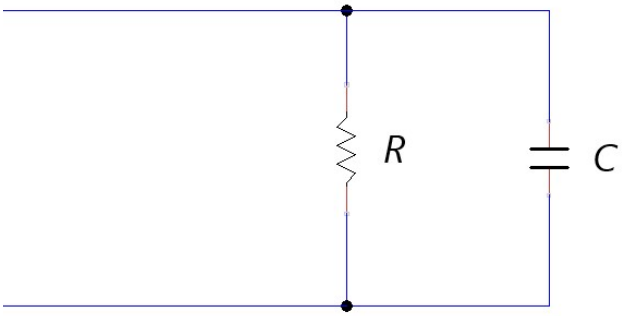

Figure 3.3: 2-element WK model

The 2 element WK is appropriate to describe aortic pressure decay in diastole, but it does not account properly for systole description [19]. Therefore, a characteristic impedance was introduced as an improvement of the classic two-element Windkessel formulation. This impedance has the same units as a resistor but has the role to describe wave traveling along the arterial system. The three-element Windkessel is represented in Figure 3.4.

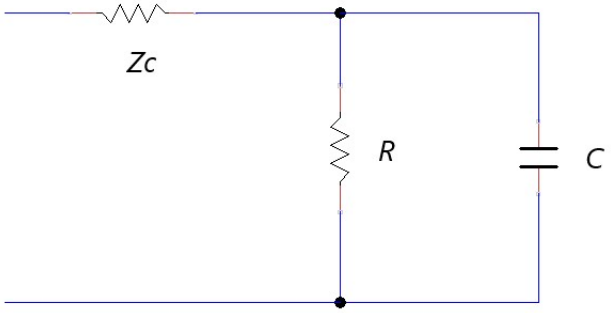

Figure 3.4: 3-element WK model

Later, Stergiopulos added an inductive element introducing the 4-element WK model reported in Figure 3.5. This fourth element represents the total arterial blood inertia of the cardiovascular system and corrects low frequency behaviour where the 3-element WK model fails to be accurate [47].

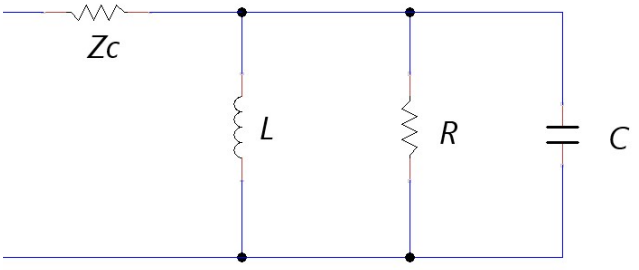

Figure 3.5: 4-element WK

Each of the above presented models is called single compartment and, as stated in [19], they "adequately describe pressure-flow relationship at the entrance of the system… but does not represent pressure in more

distal vascular system". To overcome this limitation, a multi-compartment model must be considered to partition the systemic circulation in several interacting units. This description enables us to calculate flow and pressure in different parts of the cardiovascular tree.

For instance, the arterial tree may be subdivided into large and small arteries. The first group includes the aorta, the main high-pressure pipeline connected to the heart left ventricle, and other main arteries such as the femoral and the brachial one. Large arteries are quite elastic vessels where blood flow is pulsatile. Thus, the full resistance, compliance, and inductance effects need to be considered [21]. The electric circuit describing these effects is reported in Figure 3.6 and is called RLC combination.

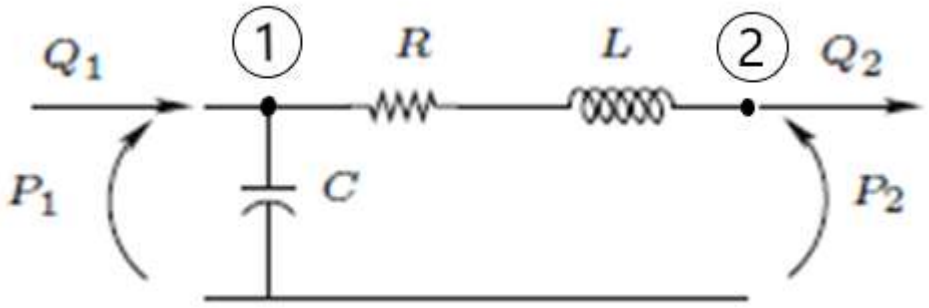

Figure 3.6:RLC combination

This circuit is mathematically described by:

$$\begin{cases} Q_1 = C\dfrac{dP_1}{dt} + Q_2 \\ P_1 - RQ_2 - P_2 - L\dfrac{dQ_2}{dt} = 0 \end{cases} \qquad \text{Eq(3.1)}$$

This system of equation (3.1) is found applying Kirchhoff's current law to node 1 and Kirchhoff's voltage law to the closed loop between node 1 and 2. The RLC combination is adopted in [22] and in [24] to describe large arteries within a multi-compartment model.

Moreover, in [25] a comparison between a linear and nonlinear formulations of the compliant element is presented. The conclusion of this work is that "no additional information is gained when a pressure-dependent, rather than a constant, compliance throughout the heartbeat is incorporated in the three-element Windkessel. Nor does the nonlinear model significantly improves the three-element Windkessel". In [21] the modeling choice of neglecting pressure dependency of large arteries is further justified by the fact that "the diameter changes in the arterial system are relatively small (order of 10%), and that the range of arterial pressures over the cardiac cycle is such that the material tends to operate in a relatively linear region of the stress-strain curve". Accordingly, we can conclude that a RLC combination with constant parameters can be considered a proper representation of these vessels.

Concerning small arteries, they comprise a network of vessels that extend throughout the body. As done in [22], the RLC combination can be used to describe hemodynamic features of this latter compartment.

To complete the description of the arterial tree we need also to consider the arterioles. Those vessels have a relatively rigid wall, the flow is steady and frictional loss is the dominant factor, thus a pure resistance element adequately describes the local flow dynamics [16]. Furthermore, one peculiar property of arterioles is autoregulation, which is the ability to maintain a relatively constant level of blood flow despite changes in perfusion pressure. Autoregulation is achieved by varying the vascular tone of smooth muscles, causing the vessels to constrict or dilate to adjust themselves to a variation of pressure and flow rate. We must account for autoregulation in a pathological condition and, from an electric point of view, it will result in a non-linear relation of the resistance describing this compartment.
Regarding the venous tree, these vessels provide a reservoir function for storing large quantities of extra blood that can be called into use whenever required elsewhere in the circulation [26]
The peculiar feature of veins is their distensibility ([27] reported the central veins to be 8 times as distensible as central arteries) and accordingly, the venous system is usually represented with a compliance. For instance, Figure 3.7 shows the modelling choice done in [15], where the venous system is represented by the capacitor C_v and it is included in a lumped parameter model of the whole cardiovascular tree.

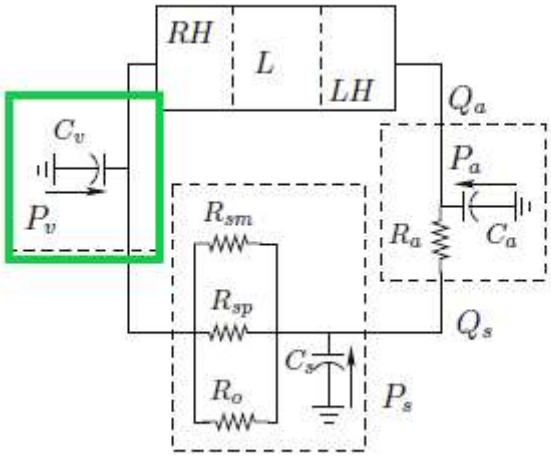

Figure 3.7: Lumped parameter representation of the venous system

Flow in veins is also pulsatile but in a more regular way than in the arteries and usually inertial effects can be neglected. For instance, this is the modeling choice done in [22] and [27] where the venous system is described with a capacitance and a resistance. Moreover, according to [21] when veins enter a collapsed state, we should consider the pressure dependency of these vessels. As in the case of autoregulation for arterioles, this property must be accounted for to describe a pathological condition.

3.2 Lumped parameter description of the heart and its contractile property

In this section we complete the overview of the cardiovascular circulation by illustrating the lumped parameter description of the heart. To pursue the target, initially we present a theoretical overview regarding the so-called PV loop, a physiological plot describing the contractile properties of ventricles, and the concept of elastance. Then, we will introduce the concept of time-varying elastance which provides a mathematical description of heart pumping function. Finally, we will illustrate the mathematical representation of this model proposed in [17].

3.2.1 Representation of the cardiac cycle through the PV loop

Cardiac cycle is the period required for one heartbeat. It is composed of a systole and of a diastole, which are the moments when heart contracts and relaxes causing its chambers to increase and decrease their stiffness, respectively. These two phases can be represented with the graph reported in Figure 3.8, called P-V loop (Pressure-Volume), which represents the instantaneous relationship between intraventricular pressure and volume through one cardiac cycle. Specifically, systole happens between point 1 and 4 whereas diastole between point 4 and 1.

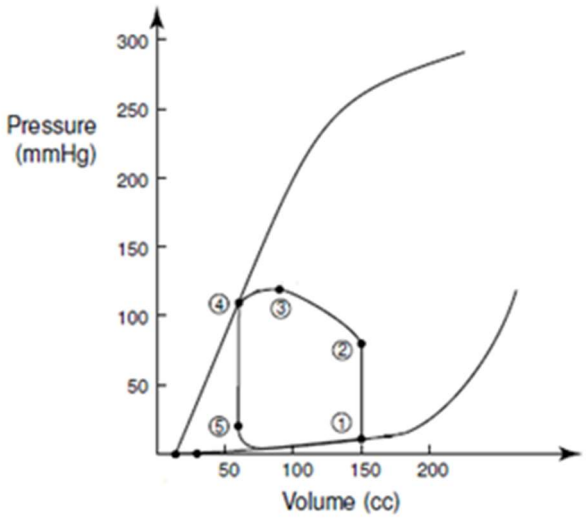

Figure 3.8: Cardiac Pressure-Volume Loop

This graph has been widely used to analyse cardiac mechanics. Specifically, contractile properties of ventricles can be represented with two pressure-volume curves in the P-V plane. The first one is the end-diastolic pressure-volume relationship (EDPVR), reported in Figure 3.9. This curve describes the passive filling of the ventricle and thus the passive properties of the myocardium.

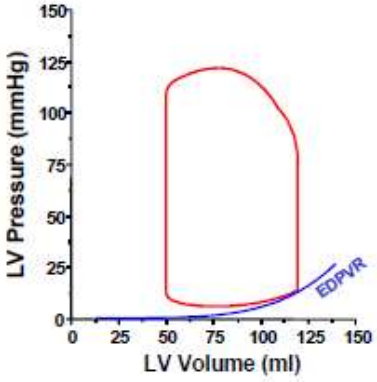

Figure 3.9: Graphical representation of the EDPVR

Quantitative analysis of the EDPVR curves has shown that pressure and volume are related by a nonlinear function, namely

$$EDPVR = P_0 + \beta V^{\alpha} \qquad \text{Eq(3.2)}$$

where V is the volume inside the ventricle, P_0 is the pressure asymptote at low volumes and α and β are constants specifying the curvature of the line depending on properties of the ventricle. The slope of the *EDPVR* at any point along this curve is the reciprocal of ventricular compliance and is called elastance. By a dimensional point of view, it is defined as

$$E(t) = \frac{[V]}{[P]} = \frac{[L^3]}{[M] \cdot [L^{-1}] \cdot [T^{-2}]} \qquad \text{Eq(3.3)}$$

At the opposite extreme of the cardiac cycle, when muscles are in their maximally activated state, we can define the second pressure volume relationship curve, called end-systolic pressure volume relationship (*ESPVR*). This curve describes the maximal pressure that can be developed at any given ventricular volume and is expressed by a linear relationship, namely

$$ESPVR = \frac{P_{es}}{V - V_0} \qquad \text{Eq(3.4)}$$

where *Pes* is the end-systolic pressure, *Vo* is a slightly positive volume remaining in the heart chamber at the end of the contraction and V is the volume. The slope of the *ESPVR* represents the end-systolic elastance, which provides an index of myocardial contractility and it can be considered an improved index of systolic function. These ESPVR and EDPVR are reported in Figure 3.10.

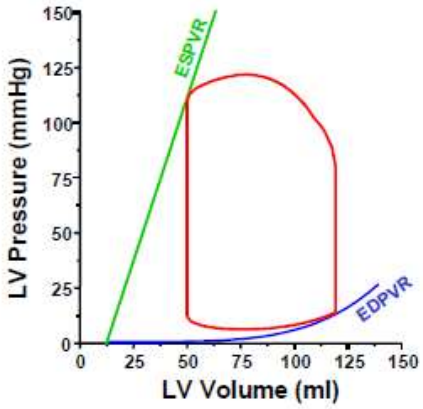

Figure 3.10: ESPVR and EDPVR in the PV plane

We can notice how the PV loop cannot cross over the line defining ESPVR for any given contractile state whereas EDPVR provides a boundary on which the PV loop falls at the end of the cardiac cycle.
Starting from these concepts we can describe the theory of the time-varying elastance.

3.2.2 Theory of time-varying elastance

The time-varying elastance model stems from the work performed by Suga and Sagawa in the early 1970s [28]. Starting from in-vivo experiments on an isolated canine left ventricle, these two authors analysed cardiac mechanics in the pressure-volume plane. Their experimental data reported in Figure 3.11 suggest how the left ventricle can be considered as a 2-state device.

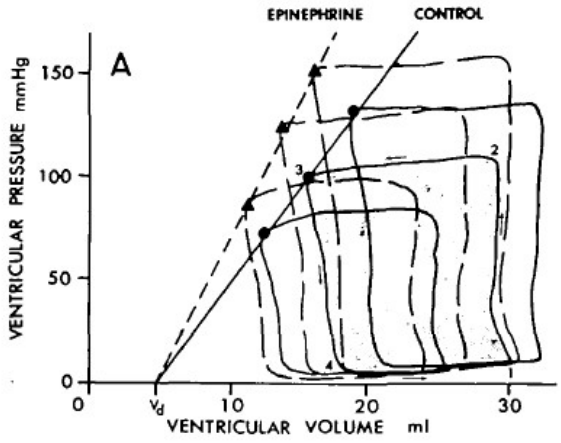

Figure 3.11: Time-varying elastance concept from [28]

As a matter of fact, in the diastole the heart behaves as an elastic chamber whose properties may be represented by a diastolic pressure-volume linear curve

$$V = V_d + C_d \cdot P \qquad \text{Eq(3.5)}$$

where C_d is the diastolic capacitance of the ventricle (the inverse of the elastance).

Similarly, during systole, the heart can be represented as a capacitor characterized by another linear pressure volume relation

$$V = V_d + C_s \cdot P \qquad \text{Eq(3.6)}$$

These relations are plotted below in the pressure-volume plane in Figure 3.12.

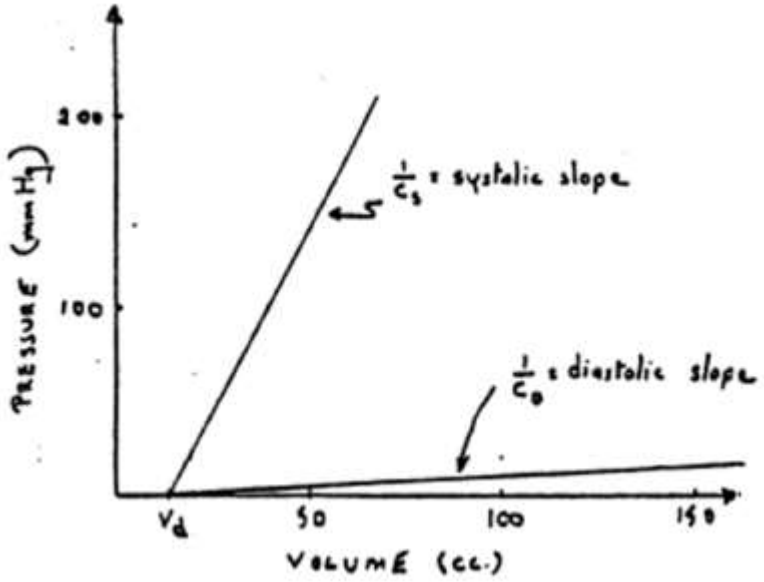

Figure 3.12: ESPVR and EDPVR in the time-varying elastance model

The previous analysis led to the definition of the time-varying elastance model [28], which relates the left-ventricular pressure P(t) and volume V(t) according to the following linear relationship:

$$E(t) = \frac{P_V(t)}{V_v(t) - V_0} \qquad \text{Eq(3.7)}$$

with E = elastance, a time-dependent slope, and V0, the fixed volume-axis intercept.
Since Eq (3.7) describes a linear dependence between pressure and volume, each time instant of the cardiac cycle in the PV loop can be described by a (generally different) value of the elastance. This concept is illustrated in Figure 3.13. Specifically, the time rate of change of elastance in the PV loop during systole and diastole is represented in the left and right panel, respectively.

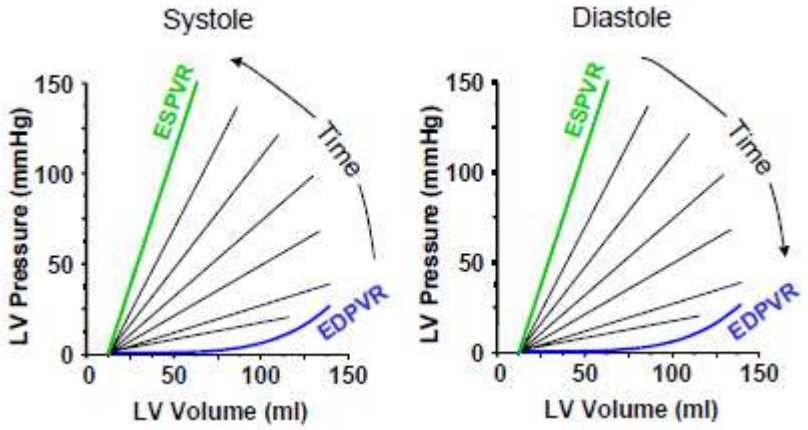

Figure 3.13: Time rate of change of elastance in the PV plane during systole and diastole

If we plot each value of the elastance as a function of time, we can observe a smooth transition during the cardiac cycle represented by the sinusoidal function depicted in Figure 3.14, called activation function.

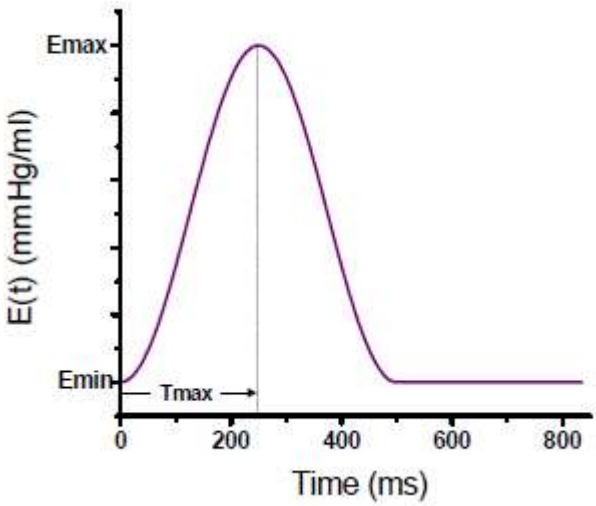

Figure 3.14:Activation function of the time-varying elastance

This function represents the time-varying elastance and it can be adopted to reproduce heart contractility. The peculiar properties of this model are that in the left ventricle the elastance function is independent of the load against which the ventricle ejects [28] and that this description included the effect of ventricular filling on ventricular contraction [29].As such, being independent of afterload and inherently containing the effect of preload, the time-varying elastance model can be considered as a constitutive equation for the ventricle that linearly relates ventricular volume to intracavity pressure according to Eq (3.7). Afterwards, it was demonstrated that, after normalizing the time-varying elastance curve, the shape was constant within one species and in a large range of cardiac diseases and it exhibited a smooth transition between ESPVR and EDPVR which is reported in Figure 3.15.

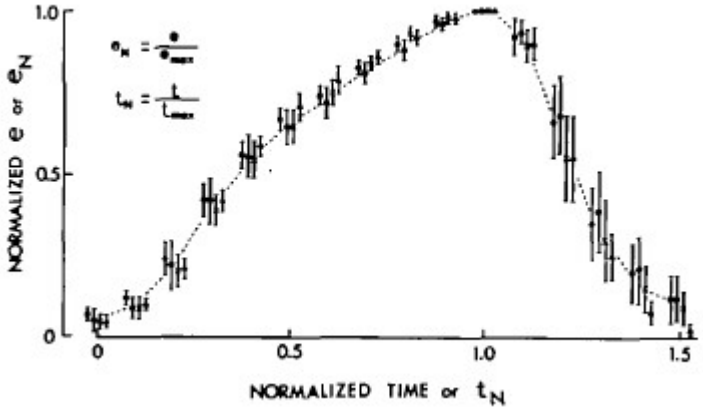

Figure 3.15:Normalized elastance

There are two implications of the described model:

- if one knows the function E(t) and the time course of volume changes during the cycle, it is possible to predict the time course of pressure changes throughout the cycle;
- Since the elastance is the inverse of a compliance, this model has been widely used to represent with a lumped approach the mechanical property of the heart as shown in the next section.

3.2.3 Lumped parameter description of the heart

One of the first lumped parameter model of the heart was developed by [30]. He represented the ventricle "as a two-component pressure source comprising an active contractile element and a series elastic element".

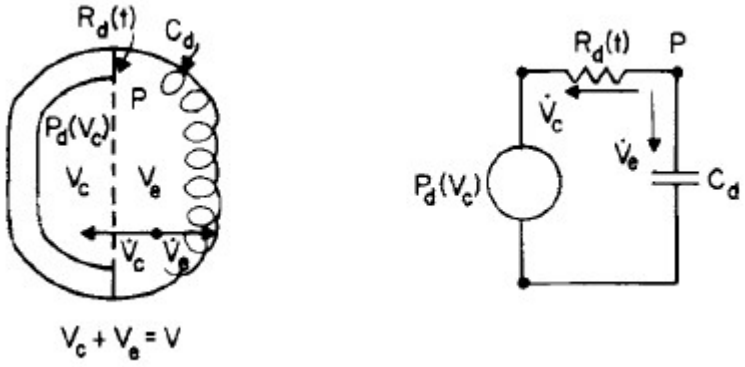

Figure 3.16: Grodins' lumped modeling of heart

In the work of Grodins the total ventricular blood volume is divided in two elements and the dynamic of the ventricle is described with a different combination of electric components in each phase of the cardiac cycle. The Frank-Starling mechanism is not embedded in this representation, i.e. the model does not reproduce the effect of an increase in the volume of blood in the ventricles.

After the appearance of the time-varying elastance model, several lumped formulation of the heart have been based on that concept. For instance, in [20] the heart contractile properties are described with a capacitor based on the observations of Suga et Al. We report in Figure 3.17 the representation of the left ventricle.

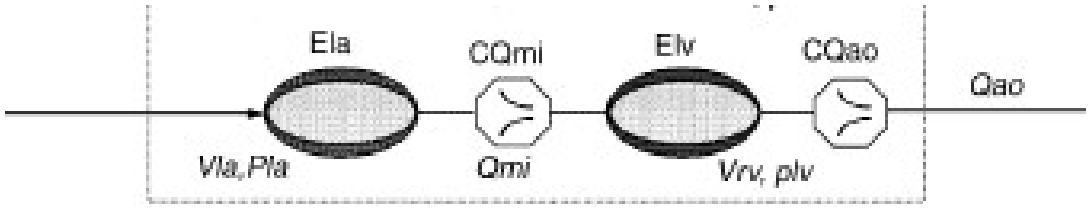

Figure 3.17:Lumped modeling of the left ventricle [from 31]

Specifically, the instantaneous volume change in the left ventricle is equal to the flow rate difference:

$$\frac{dV_{lv}}{dx} = Q_{in} - Q_{out} \qquad \text{Eq(3.8)}$$

and the pressure is computed

$$P_{LV} = P_{LV,0} + E(t) \cdot (V_{LV} - V_0) \qquad \text{Eq(3.9)}$$

where the elastance is defined as:

$$E(t) = E_{Lv,D} + \frac{E_{Lv,S} - E_{Lv,D}}{2} \cdot \bar{e}_{LV}(t) \qquad \text{Eq(3.10)}$$

$E_{Lv,S}$ is the slope of the ESPVR described before and $E_{Lv,D}$ is the slope of the linearized EDPVR while $\bar{e}_{LV}$ is the so-called activation function, which describes the contraction and the relaxation changes in the ventricular volume, and it is defined as:

$$\bar{e}_{LV} = \begin{cases} 1 - cos\left(\frac{t}{T_{s1}}\pi\right) & 0 \le t \le T_{s1} \\ 1 + cos\left(\frac{t - T_{s1}}{T_{s2} - T_{s1}}\pi\right) & T_{s1} \le t \le T_{s1} \\ 0 & T_{s1} \le t \le T_{s1} \end{cases} \qquad \text{Eq(3.11)}$$

where:
Ts1= time corresponding to the peak of systolic phase;
Ts2=time corresponding to the end of systolic phase;
T=heart period.

In the model it is also considered the possibility for the atrium to contract. Similarly with the ventricle, the atrium is modeled introducing the following variable elastance:

$$e_{LA}(t) = E_{La,min} + \frac{E_{La,max} - E_{La,min}}{2} \cdot \bar{e}_{La}(t) \qquad \text{Eq(3.12)}$$

In which the atrium activation function is defined as

$$\bar{e}_{LV} = \begin{cases} 0 & 0 \le t \le T_{pwb} \\ 1 - cos(\frac{t - T_{pwb}}{T_{pww}} 2\pi) & T_{pwb} \le t \le T_{pwb} + T_{pww} \\ 0 & T_{s1} \le t \le T_{s1} \end{cases} \qquad \text{Eq(3.13)}$$

In Figure 3.18 we report both the ventricular and atrium time-rate of change of elastances.

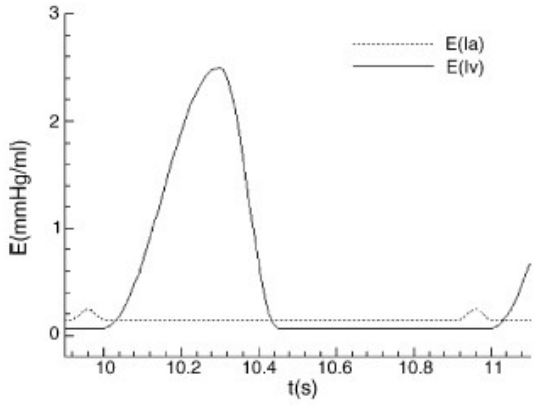

Figure 3.18: time-rate of change of elastances in the atrium and in the left ventricle [from 31]

Heart properties are described using the concept of time-varying elastance also in [22] and [16]. All these models are based on the observation of Suga et al but they are characterized by different assumptions in the derivation of the activation function.

Another possible lumped representation of the heart is described in Quarteroni [15], where a non-linear model is proposed as follows. As a first step, the authors introduce a relation linking internal pressure with the radius of an elastic spheric ball filled with fluid, namely

$$\pi R^2 P = 2\pi E h_0 R \left(\frac{R - R_0}{R_0}\right) \qquad \text{Eq(3.14)}$$

Then, using a linearization procedure, pressure can be expressed as

$$P = \frac{2E(t)h_0}{3R_0^2}\left(\frac{3}{4\pi}\right)^{1/3} V_0^{-2/3} \cdot (V - V_0) \qquad \text{Eq(3.15)}$$

Introducing the capacitance C(t)

$$C(t) = \frac{3R_0^2 V_0^{2/3}}{2E(t)h_0}\left(\frac{4\pi}{3}\right)^{1/3} \qquad \text{Eq(3.16)}$$

we can rewrite Eq (3.16) as follow

$$V(t) = C(t) \cdot P(t) + V_0(t) \qquad \text{Eq(3.17)}$$

Differentiating with respect to time yields

$$\frac{dV}{dt} = Q = \frac{dC}{dt}P + C\frac{dP}{dt} + M_Q(t) \qquad \text{Eq(3.18)}$$

Whose electric representation is reported in Figure 3.19

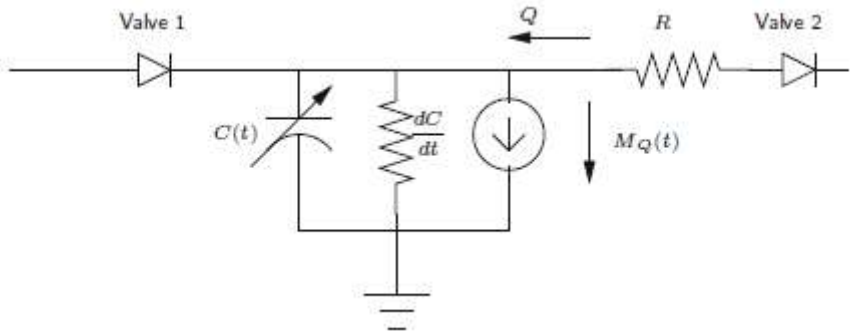

Figure 3.19: Electrical representation of heart model described in [15]

In Figure 3.19, the diodes are the electrical equivalent of valves and the resistance *R* accounts for additional resistance inside the ventricle. Throughout all the above described lumped descriptions of the heart, we consider in this thesis the model embedding the concept of time-varying elastance because of its physiological property described in Section 3.2.1. Specifically, we adopt the model of Avanzolini [17], [22] because of the detailed derivation of the time-varying elastance based on physiological concepts. In the next section we will describe its numerical derivation.

3.2.4 Mathematical description of the time-varying elastance

Avanzolini used the concept of time-varying elastance to describe an electrical analog for the two heart chambers based on a linearization of the pressure-flow relationship. The model is based on the following assumptions:

- the cardiac wall is a homogeneous medium with isotropic properties;
- thick-walled spherical geometry;
- passive pressure depends exclusively on ventricular volume;
- active pressure (tightly related to pumping functions) depends on the ventricular volume V and the rate of volume change $\dot{V}$;

Starting from these assumptions, the objective is the definition of a suitable linear approximation of the active pressure P_a with respect to V and $\dot{V}$, namely

$$P_a(t,V,\dot{V}) = P_v - P_p = a(t)\cdot P_0(V_0) + a(t)\cdot K\cdot(V-V_0) + a(t)\cdot R\cdot\dot{V} \qquad \text{Eq(3.19)}$$

where:

- P_v represents the pressure developed inside the ventricle chamber;
- P_p represents the passive pressure;
- $a(t)$ is the activation function;
- P_0 is the isometric peak active pressure related to the Frank-Starling mechanism;
- V_0 is the volume corresponding to P_0;
- K and R have the units of a stiffness and viscosity, respectively.

From a physical point of view $a(t)\cdot P_0(V_0)$ is the isovolumically developed active pressure while $\dot{V}$ is the rate of volume change representing the difference between atrial and aortic flow. This pressure description can be represented by the electrical analog circuit depicted in Figure 3.21

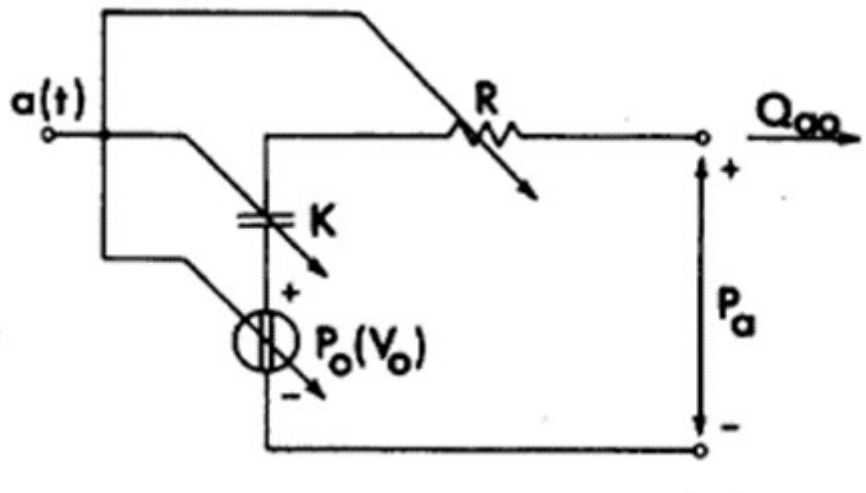

Figure 3.20:Electric analog of left ventricle (from [17])based on time-varying elastance

The left ventricle is described by three electric elements:

- an ideal voltage source describing the isovolumic pressure P_{is} ;

- a resistive element $a(t) \cdot R$ across which a pressure drop proportional to flow is developed;
- a capacitive element whose stiffness is $a(t) \cdot K$.

Both viscosity and stiffness vary with time in linear proportion to activation a(t), whereas R and K can be obtained through a calibration procedure. The similarity with the description of Suga, where the isovolumic pressure and the stiffness were combined to a single elastic element, can be observed defining

$$E(t) = a(t) \cdot K \qquad \text{Eq(3.20)}$$

and

$$V_1 = V_0 - \frac{P_0}{K} \qquad \text{Eq(3.21)}$$

By doing this, the model can be expressed as:

$$P_a(t, V, \dot{V_0}) = E(t) \cdot (V - V_0) + a(t) \cdot R \cdot \dot{V} \qquad \text{Eq(3.22)}$$

Eq(3.22) represents a classic time varying elastance model (the first-term on the right-hand side) with the addition of a time-viscous element (the second term on the right-hand side).
Finally, the ventricular pressure is given by:

$$P_V = \begin{cases} U + E_s (V - V_0) + R \dot{V} & systole \\ E_d (V - V_0) & diastole \end{cases} \qquad \text{Eq (3.23)}$$

where:

- V_0 is the reference volume;
- $U = a(t) \cdot P_0(V_0)$;
- $E = E_s + E_d$.

The activation function is described by the following sinusoidal function

$$a(t) = \begin{cases} \left[1 - cos\left(\frac{2\pi t}{t_c}\right)\right]/2 & systole \\ 0 & diastole \end{cases} \qquad \text{Eq (3.24)}$$

This model reproduces the effect of an increased in the volume of blood in the ventricle while the atrial pumping function are neglected. Moreover, based on the good fit with experimental data of this model, in [17] it is stated that "..interpretation of the success of this model is that the difference between isovolumic left ventricular pressure and pressure developed during an ejecting beat is accounted for by viscosity and stiffness, each of which varies with time in linear proportion to activation".
In a subsequent paper, the author embeds this model into a more general one representing a systemic description of the cardiovascular apparatus [22]. The more general formulation model will represent the foundation of the model proposed in this thesis.

3.3 Lumped parameter model of the cardiovascular system in a physiological healthy situation

In this section we will implement the computational model of the cardiovascular system. Initially, we will summarize the features of the reference model proposed in [22]. Then, we will modify this formulation to account for the filtration process, which will play a crucial role later in this thesis.
Finally, in section 3.3.3 we will implement the novel electrical circuit in both Matlab and OpenModelica computing environment.

3.3.1 Description and development of Avanzolini's model

We consider Avanzolini's model [22] as the starting point for the definition of the lumped model of the cardiovascular system. It is a multi-compartment model based upon fluid-electric analogy. The model is able to reproduce the main features of the cardiovascular system and consists of a closed loop.
The model is depicted in Figure 3.21.

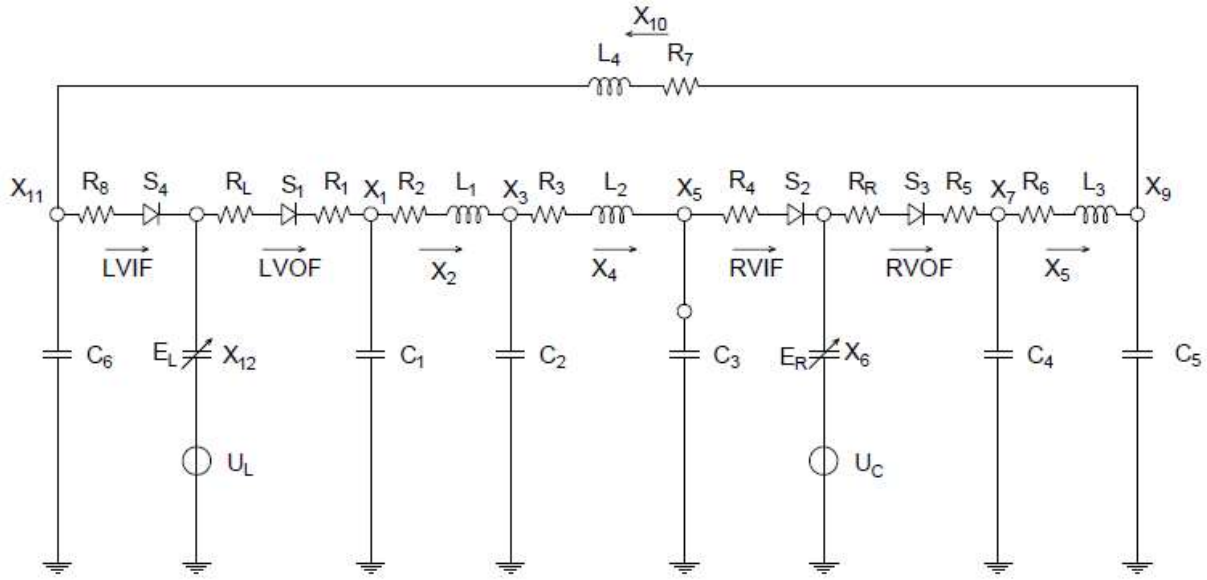

Figure 3.21: Lumped parameter model of the cardiovascular system

In the electrical circuit each node represents the pressure typical of a human compartment. We can match each electrical nodes with the corresponding physiological counterpart by comparing the pressure magnitude of each unit. For instance, we report below the range of the pressure in three nodes of the circuit from [22].

Node number	Range of pressure	Physiological compartments
X1	80-120 mmHg	AORTA
X3	75-105 mmHg	SMALL ARTERIES
X5	6-3 mmHg	VEINS

Table 3.1 :Pressure in arterial and venous trees from [22]

With a similar procedure, we describe the physiological compartments described in the model:

- large and small arteries, which are both described through a RLC combination;
- veins, modeled with a capacitor and a resistor;
- the heart is represented with the diodes, representing the valves, combined with a capacitor and a potential source embedding time-varying elastance model;
- Pulmonary circulation. which is described through an inductor and a resistor

These physiological compartments are highlighted in Figure 3.22.

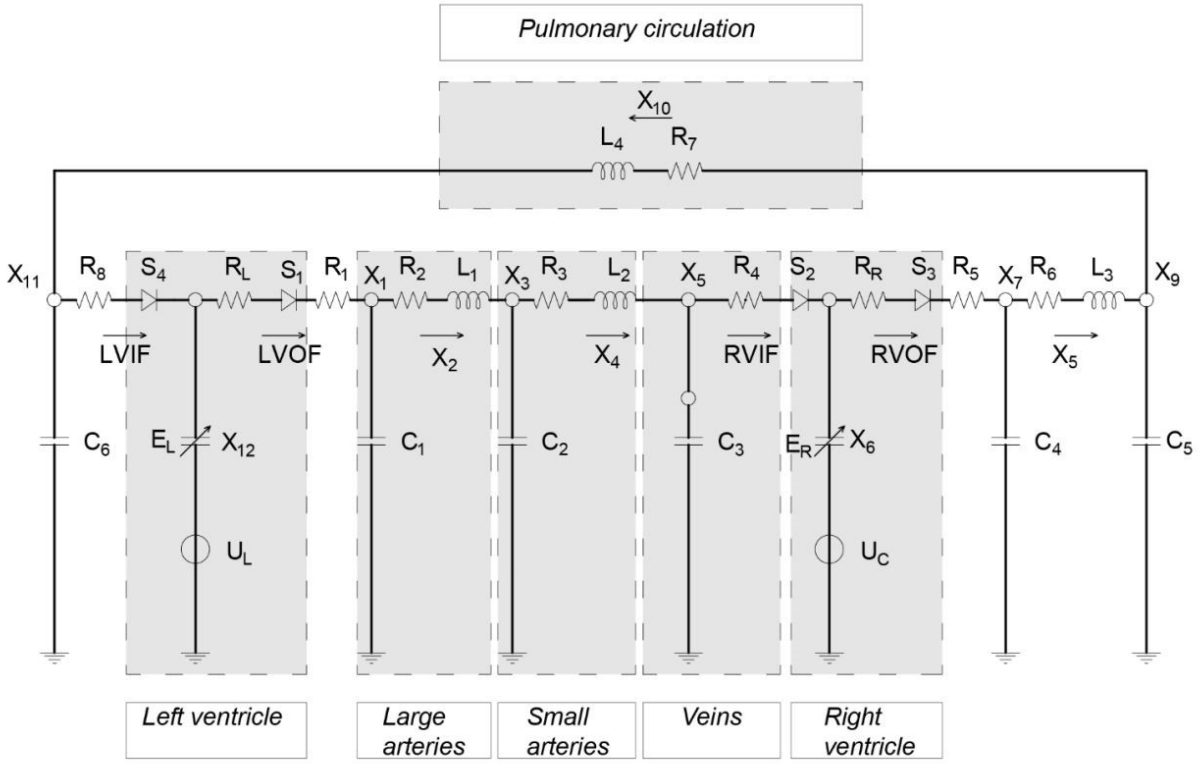

Figure 3.22: Physiological compartments described in the model of the cardiovascular system

Starting from the reference model of Avanzolini, we must address some issues to obtain a well-suited computational environment for our purposes. A first point is related to the level of physiological detail of the electrical circuit represented in Figure 3.22. As described in Section 3.1.1, we must reproduce process

of filtration/reabsorption of fluid from the vascular toward the interstitial compartment. However, the original model of Avanzolini does not comprise the capillaries, where filtration process takes place.
Hence, a first improvement is made introducing an additional electrical node representing these vessels.
To guarantee a symmetrical representation of the cardiovascular system, we add also the venules, which are blood vessels connecting capillaries with veins. The latter choice has the additional advantage to lead to a more gradual pressure drop within our proposed systemic description of human fluid balance.
By a computational point of view, we need to define the electrical counterpart of each introduced physiological compartment. Venules are characterized by a significant elastic behaviour. Thus, a capacitor is introduced to properly reproduce this feature. Additionally, we consider a resistor to model viscous losses during fluid movement. On the other hand, due to the small velocity of blood, inertial effects may be neglected and so inductors are not included.
To represent capillaries, we will introduce a resistive element because in these blood vessels the flow is steady and frictional loss is the dominant factor.
To add both the compartments of venules and capillaries in the closed loop represented in Figure 3.22, we pursue a calibration procedure of the value of their electrical parameters such as resistance and compliance. The objective is finding numerical values of the parameters that are able to provide a pressure range in both capillaries and venules in agreement with physiological expectation. Before entering in the mathematical details, we report in Figure 3.23 the graphical representation of the circuit with the additional compartments of capillaries and venules.

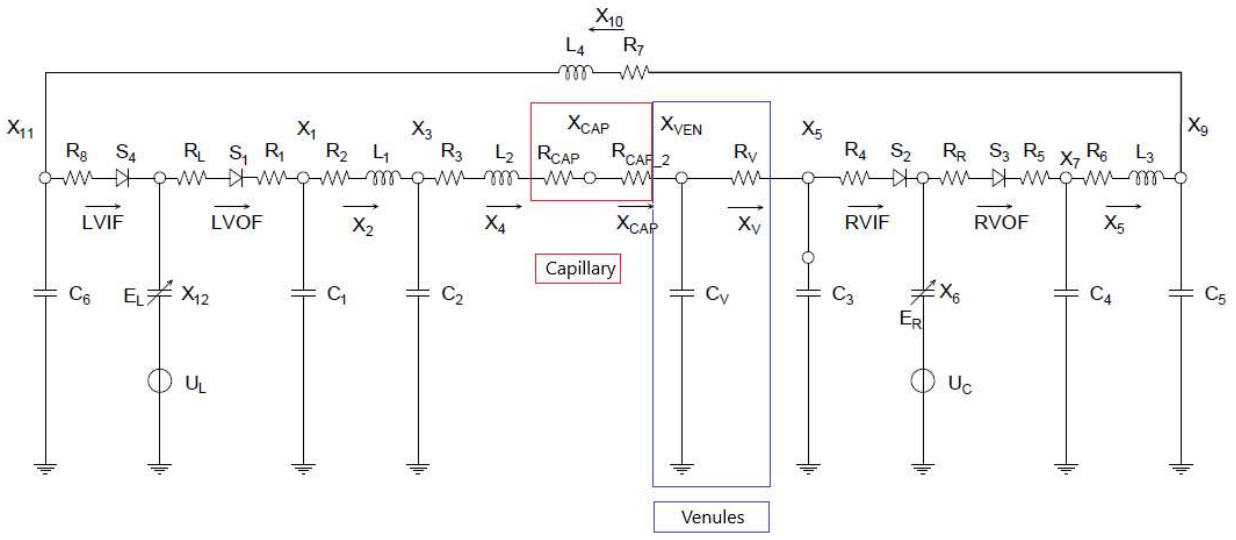

Figure 3.23: Lumped parameter model of the cardiovascular circulation comprising capillary and venules

3.3.2 Governing equation

An electrical circuit is represented mathematically through a system of ordinary differential equation and it can be solved in several ways. One of them is the state system procedure, which is illustrated for instance in [46] and leads to the following differential system:

$$\frac{d}{dt}\underline{x} = \underline{\underline{\boldsymbol{A}}}\underline{x} + \underline{b} \qquad \text{Eq(3.25)}$$

where:

- $\underline{x}$ represents the vector of the unknowns;
- $\underline{\underline{\boldsymbol{A}}}$ is the matrix of the parameters;
- $\underline{b}$ is the vector of source terms;

In our case the system reads as

$$\begin{cases}
\frac{dX_1}{dx} = \frac{S_1 \cdot U_L}{(R_L + R_1) \cdot C_1} + \frac{S_1 \cdot X_{12} \cdot E_L}{(R_L + R_1) \cdot C_1} - \frac{S_1 \cdot X_1}{(R_L + R_1) \cdot C_1} - \frac{X_2}{C_1} \\
\frac{dX_2}{dx} = \frac{X_1}{L_1} + \frac{R_2 \cdot X_2}{L_1} - \frac{X_2}{L_1} \\
\frac{dX_3}{dx} = \frac{X_4}{C_2} - \frac{X_2}{C_2} \\
\frac{dX_4}{dx} = \frac{X_3}{L_2} - \frac{R_3' \cdot X_4}{L_2} - \frac{X_{ven}}{L_2} - \frac{R_{cap} \cdot X_4}{L_2} \\
\frac{dX_V}{dx} = \frac{X_4}{C_{Ven}} - \frac{X_{ven}}{C_{Ven} \cdot R_{ven}} + \frac{X_5}{C_{Ven} \cdot R_{ven}} \\
\frac{dX_5}{dx} = \frac{X_{ven}}{R_{ven} \cdot C_3} - \frac{X_5}{R_{ven} \cdot C_3} - \frac{S_2 \cdot X_5}{R_4 \cdot C_3} + \frac{S_2 \cdot U_R}{R_4 \cdot C_3} + \frac{S_2 \cdot E_R \cdot X_6}{R_4 \cdot C_3} \\
\frac{dX_6}{dx} = \frac{S_2 \cdot X_5}{R_4} + \frac{S_3 \cdot U_R}{R_R + R_5} - \frac{S_3 \cdot X_6 \cdot E_R}{R_R + R_5} - \frac{X_7 S_3}{R_R + R_5} \\
\frac{dX_7}{dx} = \frac{S_3 \cdot U_R}{(R_R + R_5) \cdot C_4} + \frac{S_3 \cdot X_6 \cdot E_R}{(R_R + R_5) \cdot C_4} - \frac{S_3 \cdot X_7}{(R_R + R_5) \cdot C_4} - \frac{X_8}{C_4} \\
\frac{dX_8}{dx} = \frac{X_7}{L_3} + \frac{X_8 \cdot R_6}{L_3} - \frac{X_9}{L_3} \\
\frac{dX_9}{dx} = \frac{X_8}{C_5} - \frac{X_{10}}{C_5} \\
\frac{dX_{10}}{dx} = \frac{X_9}{L_4} - \frac{R_7 \cdot X_{10}}{L_4} - \frac{X_{11}}{L_4} \\
\frac{dX_{11}}{dx} = \frac{X_{10}}{C_6} - \frac{S_4 \cdot X_{11}}{R_8 \cdot C_6} + \frac{S_4 \cdot U_L}{R_8 \cdot C_6} + \frac{S_4 \cdot E_L \cdot X_{12}}{R_8 \cdot C_6} \\
\frac{dX_{12}}{dx} = \frac{S_4 \cdot X_{11}}{R_8} - \frac{S_4 \cdot U_L}{R_8} - \frac{S_4 \cdot E_L \cdot X_{12}}{R_8} - \frac{S_1 \cdot U_L}{R_1 + R_L} + \frac{S_1 \cdot E_L \cdot X_{12}}{R_1 + R_L} + \frac{S_1 \cdot U_L}{R_1 + R_L}
\end{cases} \qquad \text{Eq(3.26)}$$

where:

$-\sum X_i$ represents the n-unkwowns of our system (pressure and flow rate);

- C_i is the capacitance, L_i the inductance and R_i the resistance;

- S_i are parameters representing the state of the diode. They can be one or zero if the valve is diode is closed or open, respectively;
- E_i and U_i are the elastances and the isovolumic pressure of the time-varying elastance model described in Section 3.2.4.

Parameter value stemmed from [22] and the further calibration procedure and are reported in Table 2

Parameter	*Physiological compartment*	*Unit*
R1	0.003751	mmHg· s/cm³
C1	0.22000	cm³/ mmHg
R2	0.0675	mmHg· s/cm³
L1	0.000825	mmHg² · s/cm³
C2	1.4600	cm³/ mmHg
R3	0.75	mmHg· s/cm³
L2	0.0036	mmHg² · s/cm³
C3	20.000	cm³/ mmHg
R4	0.003751	mmHg· s/cm³
R5	0.003751	mmHg· s/cm³
C4	0.049	cm³/ mmHg
R6	0.003376	mmHg· s/cm³
RCAP	0.18	mmHg· s/cm³
RCAP_2	0.1	mmHg· s/cm³
RVEN	0.15	mmHg· s/cm³
L3	0.00075	mmHg² · s/cm³
C5	2.67	cm³/ mmHg
R7	0.1013	mmHg· s/cm³
L4	0.00308	mmHg² · s/cm³
C6	46.7	cm³/ mmHg
R8	0.003751	mmHg· s/cm³
RL	0.08	mmHg· s/cm³
RR	0.0175	mmHg· s/cm³
ER	0.03	mmHg/ cm³
EL	0.1	mmHg/ cm³

Table 3.2: value of parameter of lumped model of cardiovascular system

System 3.26 can be solved in two different ways which are described in the next section.

3.3.3 Implementation and system resolution with Matlab and Open Modelica

The ODE system (3.26) may be solved using both MatLab or OpenModelica. In Matlab, we use a code developed in 5 steps. By a numerical point of view, an implicit Euler method is used for time-discretization. We report below the flow chart representing the solving algorithm.

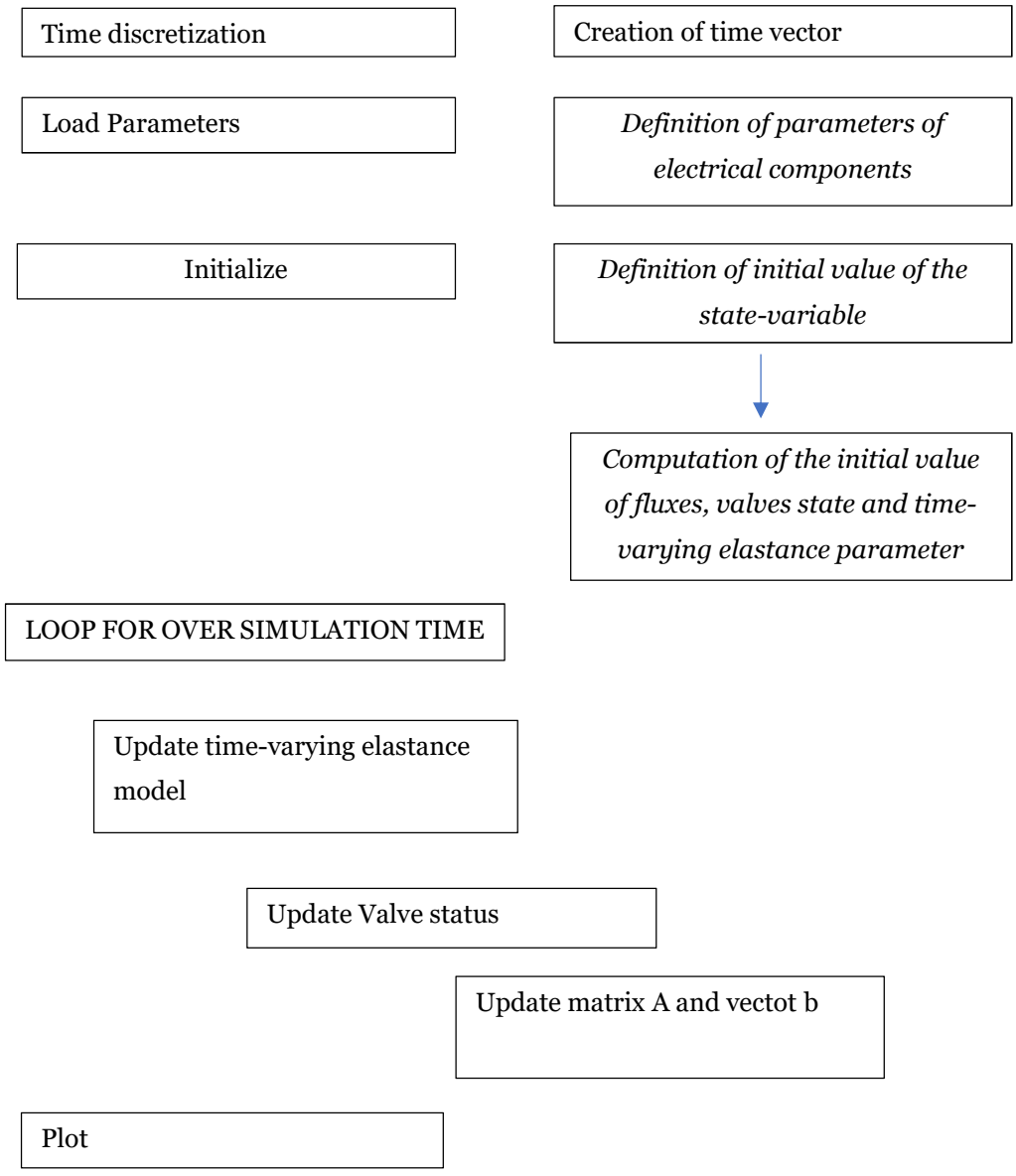

Table 3. 3: Matlab algorithm to solve the proposed lumped parameter model of the cardiovascular system

System 3.26 can also be solved with the equation-based language Open Modelica. In this environment, we introduce through a graphical interface the electrical objects constituting the circuit reported in Figure 3.23. Electric components are instances of Modelica classes and their properties are already implemented in the library of the software. We show in Figure 3.24 a practical example of the use of the graphical interface provided by OpenModelica.

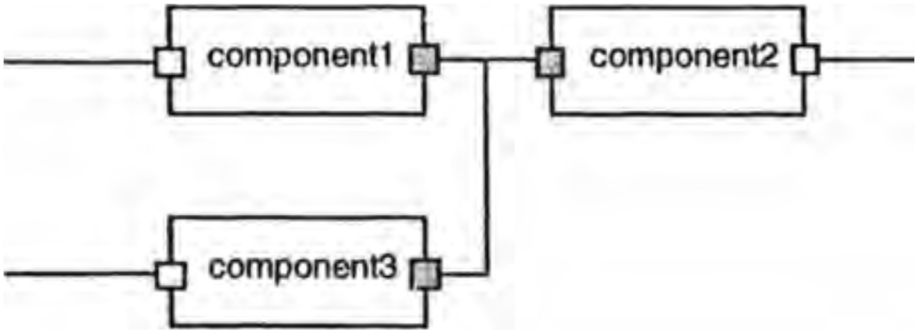

Figure 3.24: Connector and component in OpenModelica

Each rectangle in the diagram represents a physical component such as a resistor or a capacitor. They can exchange information through interface points which, in Figure 3.24, are represented as small square dots connected by lines representing real physical connection such as a wires or a cable. Once components and connectors are defined, the software will establish two different types of coupling according to the nature of the variables. If we have a nonflow variable, such as electric potential, the software forces an equality coupling, according to Kirchhoff's first law, while Kirchhoff's current law will be established between flow variables leading to a sum-to-zero coupling. We can better specify this concept with the example shown in Figure 3.25, where we have two instances of the class resistor R1 and R2

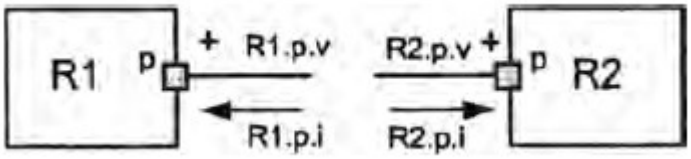

Figure 3.25: Connection between two resistors in Open Modelica

These two components interact thanks to the presence of an interface class (called pin) and a connection equation which is specified through the declaration "connect". Declaring "$connect(R1.p, R2.p)$", we actually connect the two components and this step is equivalent to imposing the following system of equation

$$connect(R1.p, R2.p)" = \begin{cases} R_1.p.v = R_2.p.v \\ R_1.p.i + R_2.p.i = 0 \end{cases} \quad \text{Eq(3.27)}$$

Accordingly, to reproduce the Avanzolini model in OpenModelica we must introduce the electrical components represented in Figure 3.23 and connect them in agreement with Kirchhoff's first law. Classes representing inductor, capacitor and resistance are already implemented in OpenModelica's library. However, to implement our proposed model we to define three new classes, that are described below.

Diode

A diode is the electrical component representing the valve. It is represented in OpenModelica as follow

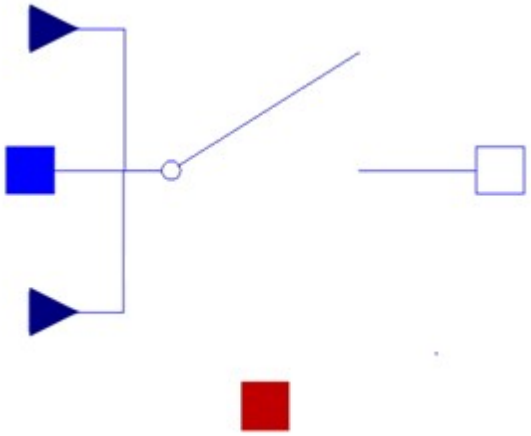

Figure 3. 26:Diode in OpenModelica

It is characterized by the presence of two interfaces Pin (the rectangle in Figure 3.26) needed to connect it with the other components of the model. The presence of the two interfaces Real (the triangle in Figure 3.26) allows us to specify the equation which will govern the behaviour of this object

$$off = noEvent\ (input1 - input2\ < 0) \qquad \text{Eq(3.28)}$$

where *off* means that the diode will be closed allowing the current to flow. Eq(3.28) makes valve open and close according to the pressure gradient established upstream and downstream the diode

Capacitor ventricle

The capacitor is the element which represents the isovolumic term in the electric representation of the time-varying elastance presented in section 3.2.2. It is defined as the following two state device described in Suga et Al

$$C = E_D + E_S \cdot a(t) \qquad \text{Eq(3.29)}$$

where $a(t)$ is the activation function defined as

$$(t) = \begin{cases} \left[1 - cos\left(\frac{2\pi t}{t_c}\right)\right]/2 & systole \\ 0 & diastole \end{cases} \qquad \text{Eq(3.30)}$$

Voltage ventricle

It describes the isovolumic pressure developed inside the ventricle according to:

$$P_{is} = U_o \cdot a(t) \qquad \text{Eq(3.31)}$$

Having introduced the above three new classes, we can solve Eq(3.27). The obtained results using both software are similar and agrees with physiological expectations. For instance, in Figure 3.27 we report pressure computed in the large arteries

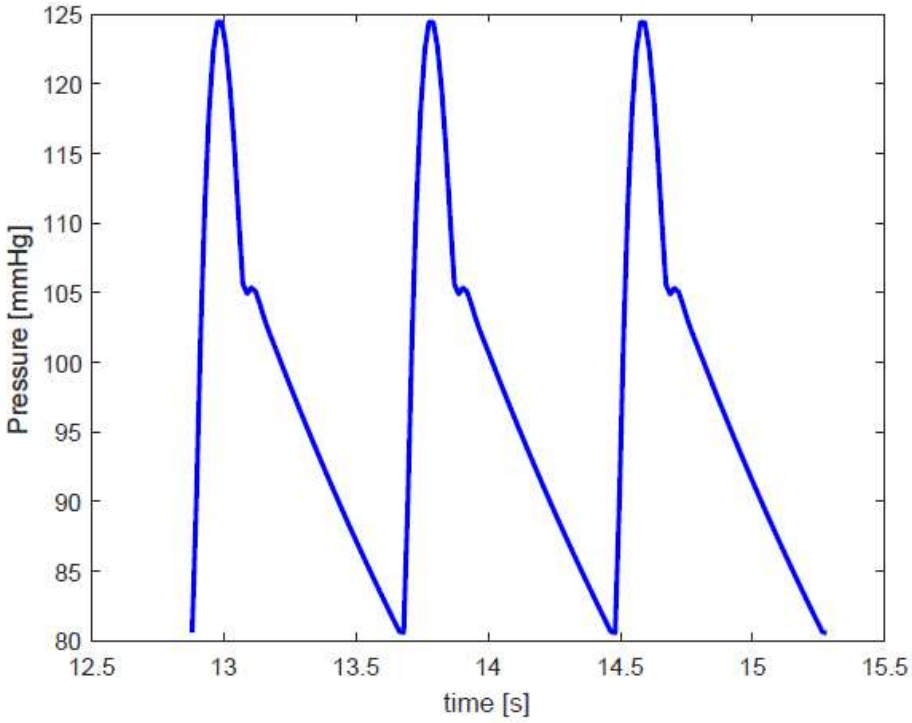

Figure 3.27: Computed time-rate of change of pressure in large arteries

In Figure 3.28 and 3.29 we report the pressure in the veins as well as in the capillaries and venules.

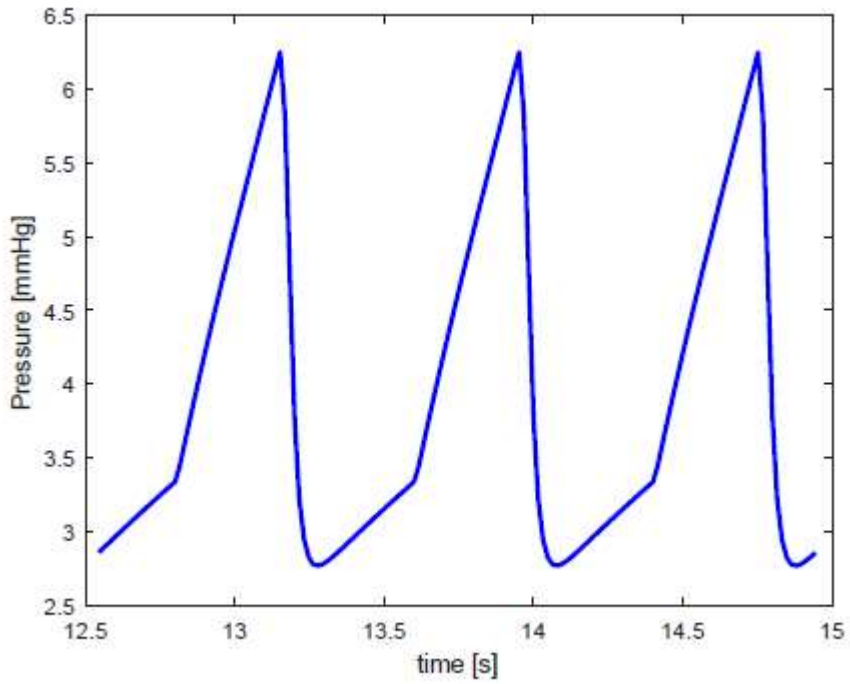

Figure 3.28: Computed time-rate of change of pressure in veins

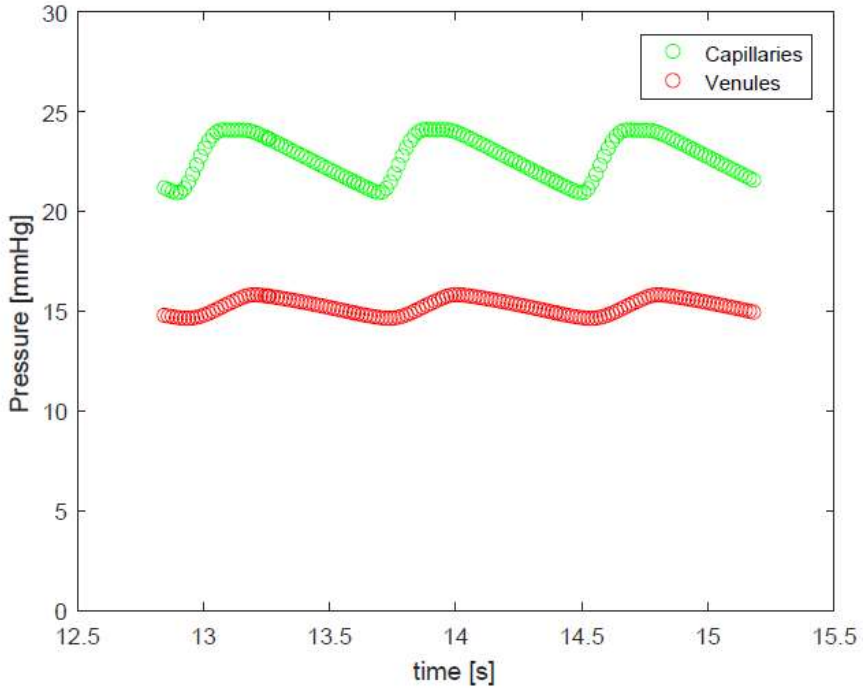

Figure 3.29: Computed time-rate of change of pressure in large arteries in capillaries and venules

We can observe a good agreement between model predictions and the physiological expected range at pressure and reported in Figure 3.30 [9]

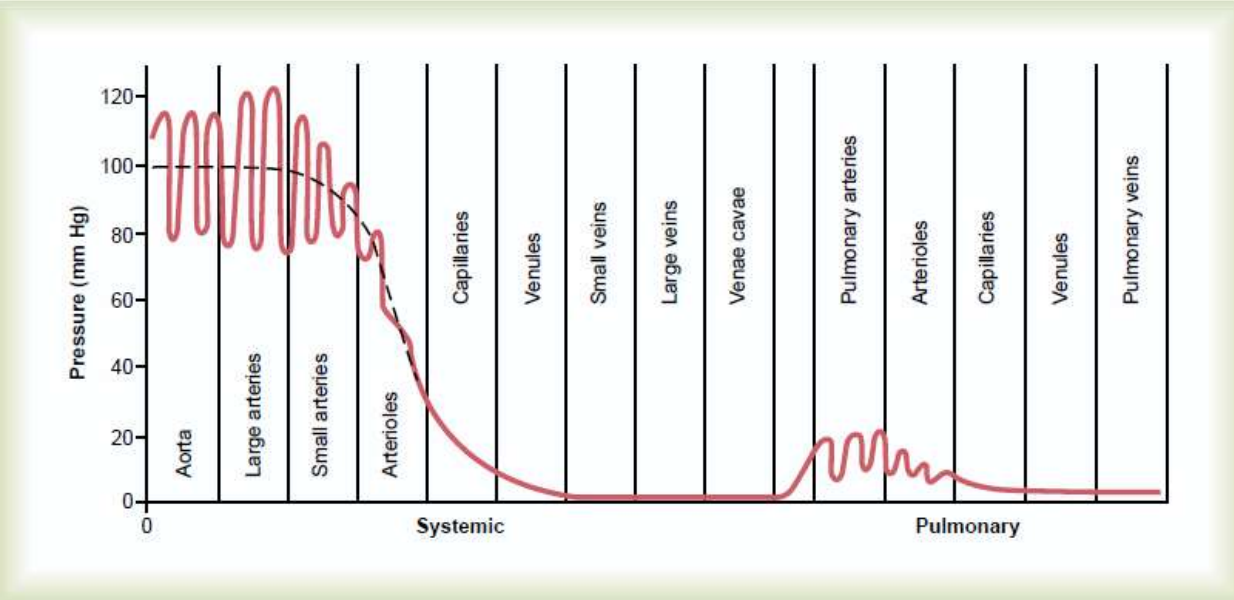

Figure 3.30:Pressure in the cardiovascular system

Based on the above results, we can conclude that the implemented circuit is able to correctly reproduce the main features of the cardiovascular system. Hence, the proposed model represents the mathematical framework for embedding the filtration process and later to study the lymphatic system. From now on, we will use Open Modelica which is more suited for the implementation of an electric network.

3.4 Filtration process and interstitial space

At this stage of the presentation, the lumped electric circuit representing cardiovascular circulation is characterized by the level of detail required for our purposes. However, to quantitatively investigate the role of the lymphatic system on human fluid balance we need yet to describe the process of filtration and the interstitial space. In section 3.4.1 and 3.4.2 we will summarize the key physiological concepts regarding the filtration process before introducing its lumped counterpart. Then, in section 3.4.3, the same procedure will be applied to the interstitial space.

3.4.1 Starling's law and filtration process

Filtration process is the mechanism through which we have a partition of fluid between the vascular and interstitial compartments. Specifically, once blood arrives at the capillaries side of the systemic circulation, there are forces (hydrostatic and oncotic) which lead to an exchange of fluid through those vessels [10].

In 1896 Starling proposed that passive factors such as surface area (S), and gradients in hydrostatic (ΔP) and oncotic (Δπ) pressure determine fluid exchange according to the following equation (with the assumption of steady-state conditions):

$$\frac{J_v}{S} = Lp[\Delta p - \sigma \Delta \pi] \qquad \text{Eq(3.32)}$$

Where

- $\frac{Jv}{S}$ is the fluid flux per unit surface area [ml s^{-1}]
- Lp is the hydraulic conductivity [ml s^{-1} $mmHg^{-1}$], which is a coefficient describing the leaky behaviour of the barrier to water;
- σ is the osmotic reflection coefficient, a dimensionless coefficient varying between 0 and 1;
- $\Delta\pi$ is the oncotic pressure gradient [mmHg];
- Δp is the hydrostatic pressure gradient [mmHg].

We now analyse more in detail the various operating at the capillary membrane.
ΔP represents the hydrostatic pressure difference between the capillaries (*Pc*) and the interstitium (*Pif*)

$$\Delta P = P_c - P_{if} \qquad \text{Eq(3.33)}$$

This term tends to force the fluid and its substances dissolved into the fluid through the capillary pores into the interstitial spaces, leading to a net filtration.
Conversely, Δπ represents the oncotic pressure difference between the capillary and interstitial compartments

$$\Delta\pi = \pi_c - \pi_{if} \qquad \text{Eq(3.34)}$$

Specifically, oncotic pressure π is a direct function of protein concentration, as can be seen from Onsager's law:

$$\pi = \varphi \cdot n \cdot C \qquad \text{Eq(3.35)}$$

where Φ is a correction coefficient, n is valence number, and C is molar concentration of the protein.
Throughout all the plasma proteins, albumin plays a dominant role because of its relative high concentration in the interstitial compartment compared to the vascular vessels. As a result, albumin leads to an inward fluid movement by osmosis in the capillaries which prevents significant loss of fluid volume. However, the actual magnitude of this oncotic force depends on the reflection coefficient σ. Specifically, σ indicates the likelihood that a molecule approaching a pore in a membrane will be reflected and retained in the vascular compartment [10].
When σ = 1, the barrier is a perfect semi-permeable membrane that allows the passage of the sole water and excludes the passage of all solutes; in the opposite condition, characterized by σ = 0, when none of the solutes is reflected at the barrier. If we represent graphically the volume flux per unit surface area (Jv/S)

against hydrostatic pressure, we obtain a straight line with slope equal to the hydraulic conductivity (Lp) and pressure axis intercept equal to σΔπ as reported in Figure 3.31.

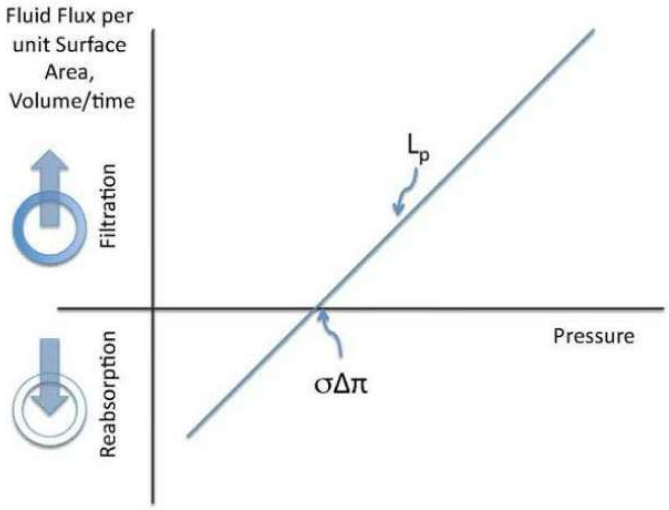

Figure 3. 31: Graphical representation of Starling's Law

Having highlighted the physical meaning of all terms in Eq(3.32), we can rewrite it as follows

$$J_v = K_f \cdot NFP \qquad \text{Eq(3.36)}$$

where

- $K_f = L_p \cdot S$
- $NFP = \Delta p - \sigma\Delta\pi$

This new formulation of the Starling law allows us to highlight a peculiar characteristic of the human filtration process. Under physiological conditions there is a slight imbalance in forces which leads to a positive *NFP*. Hence, we expect a net fluid movement from the capillary side of cardiovascular circulation into the interstitial space, whose magnitude is defined by Eq(3.36).
The net flux from the capillary is defined as trans-endothelial filtration and it is called J_v in Figure 3.32 and, in a physiological condition, must be equal to lymph flow (called J_{lymph} in Figure 3.32) [10].
This fluid removal from the interstitial space is crucial to maintain an equilibrium fluid condition in the human body.

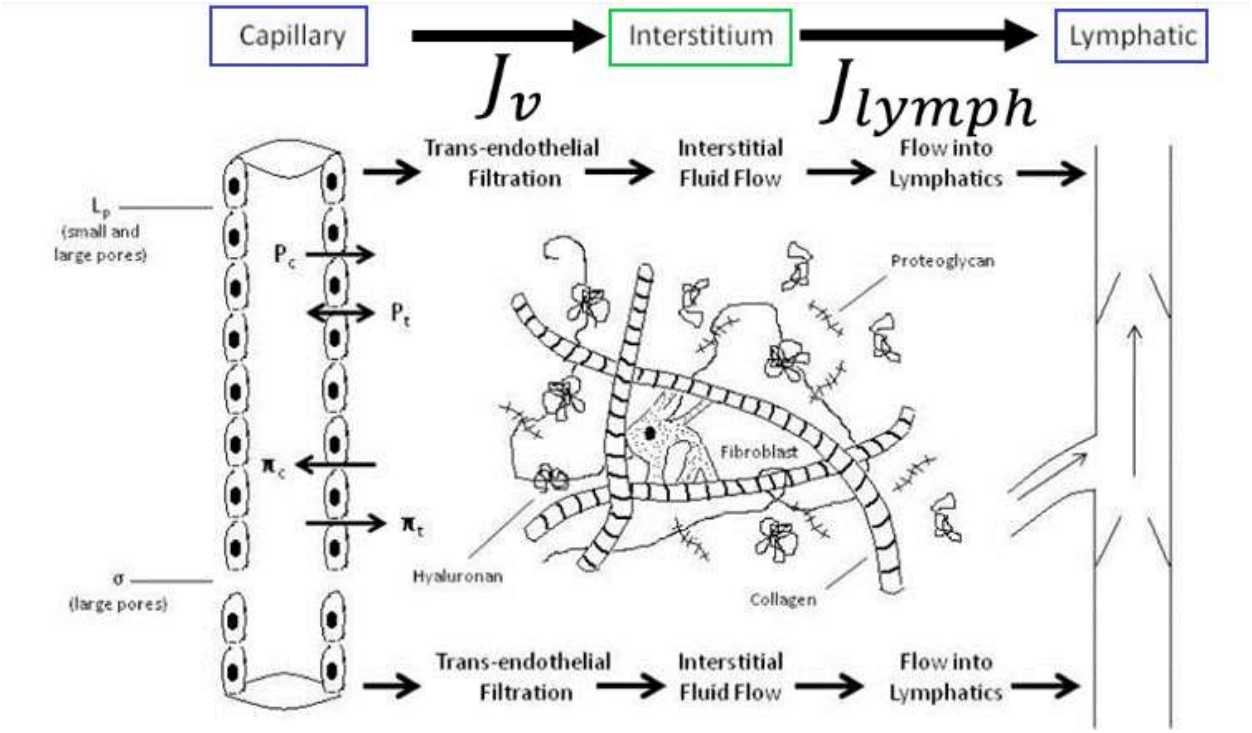

Figure 3.32: Trans-endothelial filtration process

3.4.2 Electric representation of the filtration process in healthy condition

Having described the physiological basis of the filtration process, we can now describe its electrical counterpart. Before doing that, a modeling assumption regarding the physiological compartments involved in this process is introduced. According to Huxley "… widely held perception on exchange are that capillaries are the primary site for volume flow" [10].

Hence, we will develop a lumped model of an equivalent capillary compartment that summarizes the whole filtration process, which is represented in Figure 3.33. This equivalent vessel includes both the hydrostatic and contribution of the Starling law and it will reproduce the several liters per day of water seep into the interstitium (J_v in Figure 3.32).

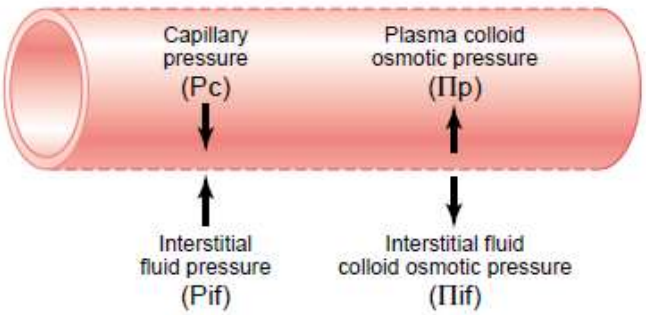

Figure 3.33: Lumped equivalent compartment of the capillary

The electrical counterpart of the filtration process is reported in Figure 3.34.

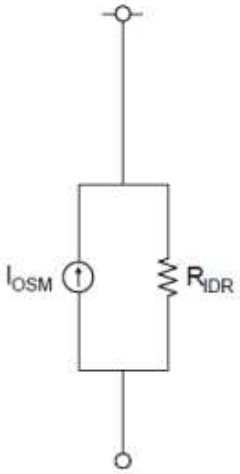

Figure 3. 34:Electrical equivalent of the filtration process

Specifically, we have an ideal current source as well as a linear resistor. The resistance, called RIDR, is defined as

$$RIDR = \frac{1}{L_p \cdot S} = \frac{1}{K_f} \qquad \text{Eq(3.37)}$$

and it is the electrical counterpart of filtration coefficient *Kf*. Hence, the resistor will describe the filtration caused by hydrostatic pressure. In contrast, the current source will describe contribute of osmotic pressure and it is defined as follows:

$$I\_OSM = Kf \cdot \sigma \cdot \Delta\pi \qquad \text{Eq(3.38)}$$

To compute the value of both R_IDR and I_OSM we must determine a value of $K_f, \Delta\pi$ and σ which is representative of the whole filtration process between the capillary and the venular side. As stated in [9], *Kf* can be computed based on the net fluid filtration and it is equal to 0.11 $cm^3/s/mmHg$.
However, if [9] provide an estimate of the overall daily filtration between 2 and 4 liters, according to [4] and [11] this quantity is expected to be between 8 and 12 liters, i.e. three times bigger.

Hence, we can consider, in agreement with this physiological uncertainty, a reasonable value of the total filtration coefficient in the interval between:

$$0.11 \leq Kf \leq 0.33 \qquad \left[\frac{ml}{mmHg \cdot s}\right] \qquad \text{Eq(3.39)}$$

Conversely, the ideal current generator will be characterized as follows.

$$I\_OSM = Kf \cdot \sigma \cdot \Delta\pi \qquad [ml] \qquad \text{Eq(3.40)}$$

According to [10] and in agreement with [49], a reasonable approximation of albumin's reflection coefficient, one of the main determinant of osmotic filtration process as described above, is 0.8 or above. Instead, $\Delta\pi = 20\ mmHg$ [9]. Hence, once Kf is calibrated, we can compute a physiological value of both R_IDR and I_OSM.

3.4.3 Interstitial space and its electric representation

Having introduced the electric counterpart of the filtration process, the last compartment we need to consider the interstitial space. This is part of the microcirculation (joint with capillaries) representing the spaces between cells and tissue-specific structures such as barrier membranes

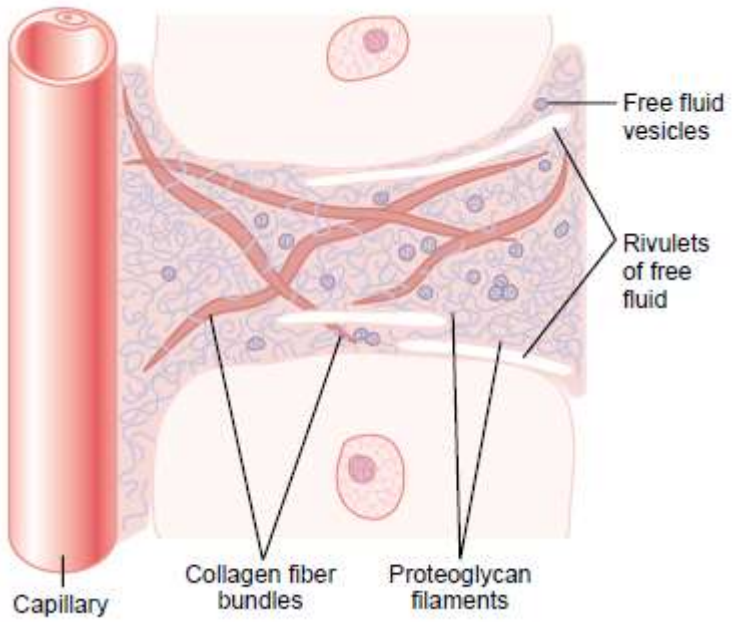

Figure 3.35: Interstitial space

The interstitial space is where fluid goes after the filtration process and both by a physiological and electrical point of view can be characterized through a compliance measuring the change in the interstitial fluid volume divided by the corresponding change in interstitial hydrostatic pressure, namely

$$C = \frac{\Delta V}{\Delta P} = \frac{\Delta IFV}{\Delta P} \qquad \text{Eq(3.41)}$$

Where ΔIFV is the volume of the interstitial space.The behaviour of this quantity can be represented as follow:

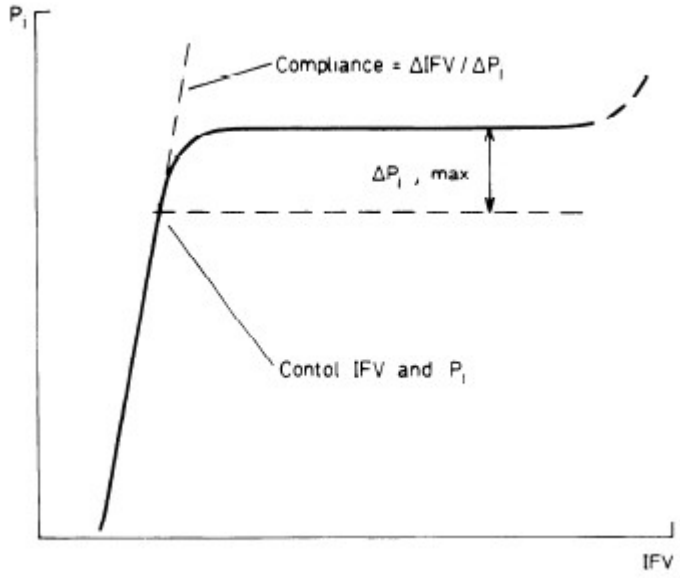

Figure 3.36:Interstitial compliance

The first studies and estimation about this quantity stemmed from Guyton and they demonstrated that it is linear in dehydration, around control and in the initial part of overhydration [40] while it remains practically constant as tissue volume increases over 50-100%.
Accordingly, since we are considering a physiological condition, the compliance will be characterized by a linear capacitor whose value will be obtained through a calibration procedure.

CHAPTER 4
LUMPED EQUIVALENT MODELING OF THE LYMPHATIC SYSTEM

In this chapter we will complete the description of the lumped parameter modeling of human fluid balance. In section 4.1 we will present a review regarding the lumped description of the lymphangions. Specifically, we will highlight an analogy of behaviour between this element and the pumping mechanism of the heart. Based on this similarity, we will define the electric counterpart of the lymphangion in our model.

Afterwards, we will investigate the connection among the latter compartment and the model of the cardiovascular circulation described in Chapter 3. This procedure is not straightforward because of several physiological open questions regarding the lymphatic system. The questions will be addressed through the use of the virtual laboratory proposed in the present thesis which, unlike in-vivo experiment, has the power of isolating each compartment from the whole structure.

In section 4.3 we will analyse the obtained results comparing them with the physiological literature.

4.1 Lumped parameter description of the lymphatic system

The main target of this chapter is the definition of a lumped model of the lymphatic system. The proposed formulation will be connected with the model of the cardiovascular system to reproduce fluid homeostasis in the human body as depicted in Figure 4.1.

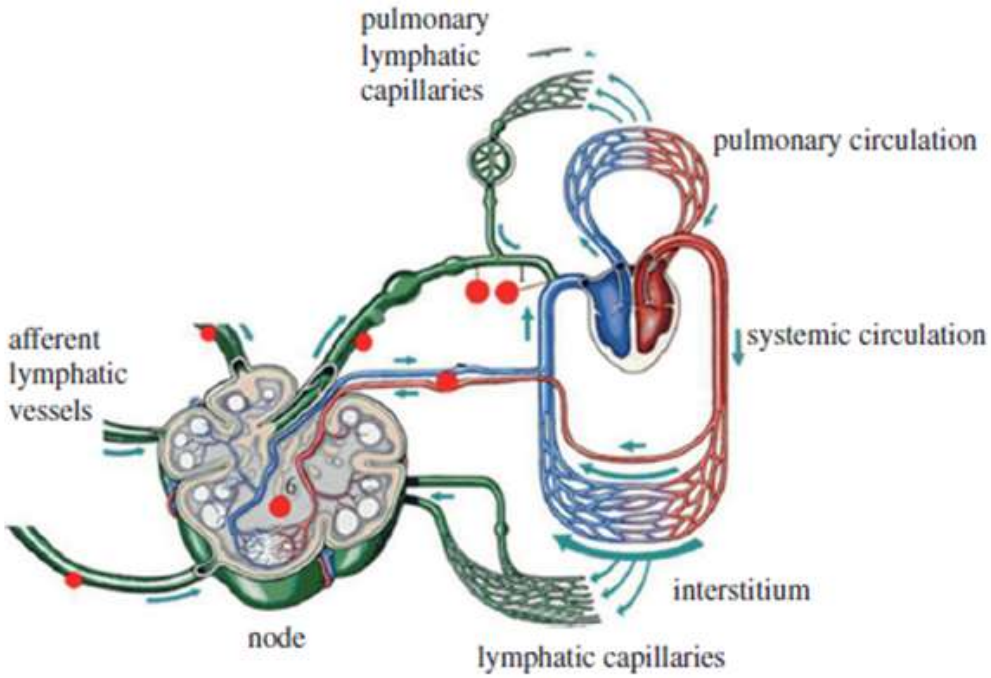

Figure 4.1: Lymphatic vascular network

To this purpose, we must describe the lymph flow pathways as shown in Figure 4.2

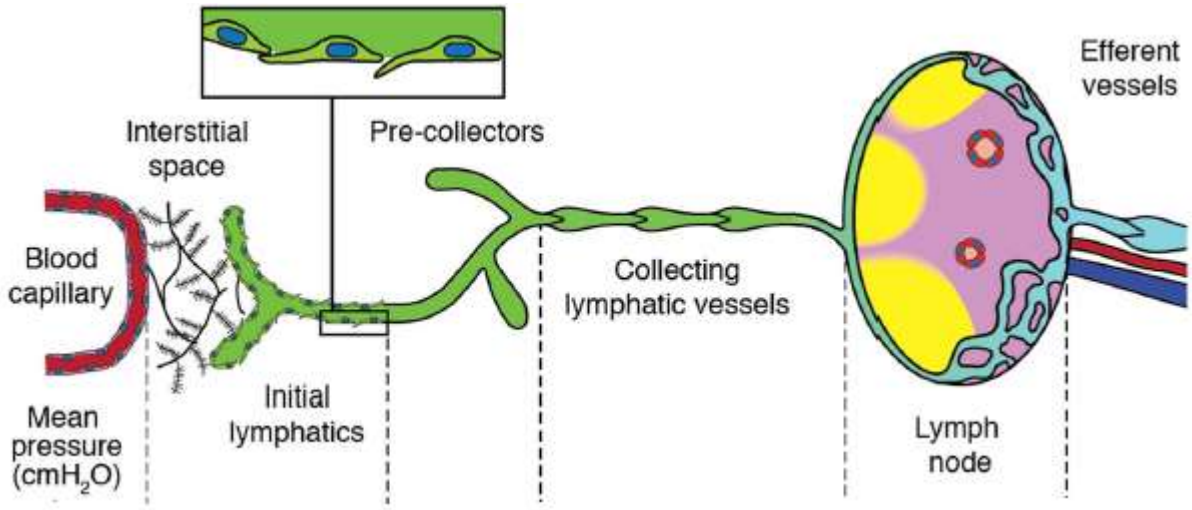

Figure 4.2: Lymph flow pathways

The lymph flow is the flow through the lymphatic system from the interstitial space toward the venous side of the cardiovascular circulation. The movement through this pathway occurs against a pressure gradient (as shown in the introduction). Hence, we must model the component of the lymphatic system which provides the driving force for the movement, called lymphangion. The peculiar property of this element, represented in Figure 4.3, is the contractility.

Owing to this property, lymphangions pump fluid and provide it the energy needed to move against a pressure gradient (as showed in the introduction). It is worth noting that without this element we are not able to connect the interstitial space with the venous system because it would cease fluid propulsion.

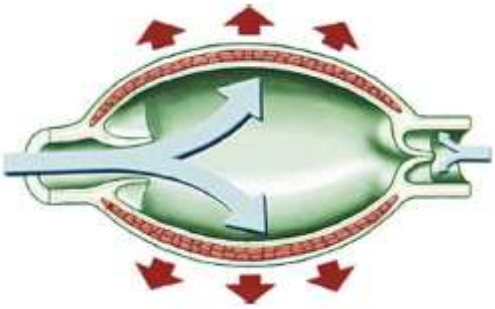

Figure 4.3: Lymphangion

In the next section we present a review of the lumped modeling of the lymphangion.

4.1.1 A review of lymphangion modeling

The first lumped model of a lymphangion was developed by Drake [33]. It consisted of a pressure source (called Pp in Figure 4.4) and a resistor representing an effective lymphatic resistance (R_L).
This model is empirical because both Pp and R_L weren't predicted from known properties of lymphatic vessels or anatomical structures such as length or radius, but they were obtained from a linear regression of measured data.

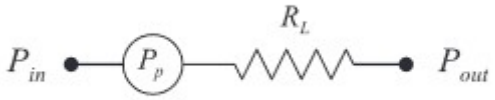

Figure 4.4: Lumped parameter model of a lymphangion (from [33])

A different approach was considered by Quick et al, who related lymph flow to the mechanical properties of lymphangions [34]. To define this model, they relied on the analogy of behaviour between the pumping characteristics of the heart and of these vessels, which has been analysed in several works such as [35], [36], [37]. For instance, in [36], it is reported how "several phases of systole and diastole were observed and plots of pressure versus volume yielded a counter clockwise loop highly reminiscent of the classic relation used to describe cardiac function".
Based on this similarity of pressure-volume relationship, they employed the time-varying elastance concept, originally formulated for the ventricles of the heart, to describe the mechanical property of the lymphangion. This modelling approach was further specified in [18].

The purpose of this work was to derive an algebraic equation predicting lymphangion flow from fundamental physical principles. The authors used the same electric description as in [33] and introduced the elastance concept to characterize both contractility and effective resistance of the vessels.

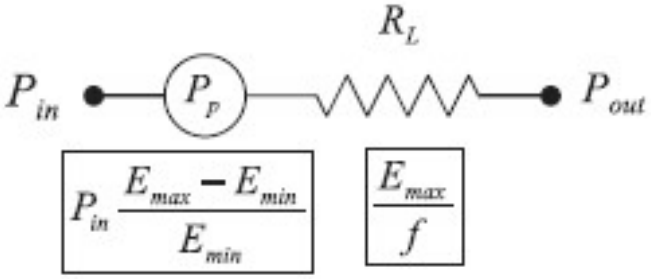

Figure 4. 5: Lumped parameter model of a lymphangion (from [34])

As can be seen, the pressure source in Figure 4.5 is a function of Pin and the relative change in the elastance, namely

$$P_p = P_{in} \cdot \frac{E_{max} - E_{min}}{E_{min}} \qquad \text{Eq(4.1)}$$

Introducing E_{min} and E_{max} they characterized both lymphangion tone (E_{min}) as well as the contractility (E_{max}).The value of the resistance is expressed as:

$$R_L = \frac{E_{max}}{f} \qquad \text{Eq(4.2)}$$

Where f is the contraction frequency.

This model related mean lymph pressure-flow relationship to mechanical properties of lymphangion and proved to be able to reproduce experimental results described in a previous work [37].

Then Venugopal et al[31] refined the time-varying elastance model using a bilinear approximation for the pressure–volume relationship. Their proposed hypothesis is that ".. lymphangions change behaviour depending on the magnitude of the transmural pressure: at higher transmural pressures, lymphangions become insensitive to it and maintain constant stroke volume" [31].

In [32], Gajani proposed another modeling to reproduce lymphangions' properties.

He introduced the following assumptions:

- Newtonian fluid
- Cylindrical vessel section of radius r and length l;
- Hydraulic resistance modeled using Poiseuille's law as:

$$R = \frac{8\mu l}{\pi r^4} \qquad \text{Eq(4.3)}$$

- Compliance for thin surface vessels

$$C = \frac{2\pi r^3 l}{sE} \qquad \text{Eq(4.4)}$$

-Inductance

$$L = \frac{lp}{\pi r^2} \qquad \text{Eq(4.5)}$$

Having introduced these values of the electrical parameters, Gajani et al [32] described the lymphangion through the following electrical circuit:

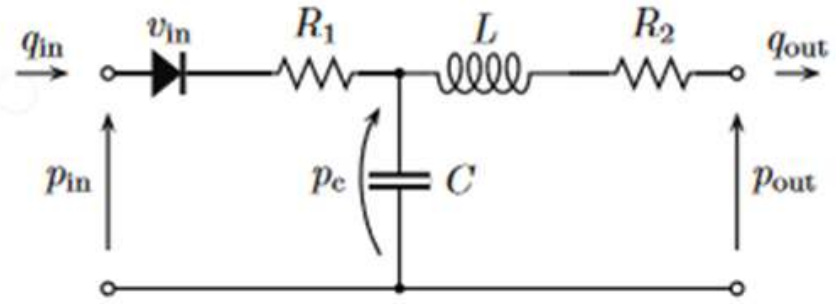

Figure 4.6: Model of a lymphangion from Gajani [32]

In this model all the parameters depend on the radius of the cylinder. For instance, the peculiar relationship of a capacitor

$$q = C \cdot V \qquad \text{Eq(4.6)}$$

is expressed as

$$i = \frac{dq}{dt} = \frac{d(C \cdot V)}{dt} = \dot{V} \cdot C + \dot{C} \cdot V \qquad \text{Eq(4.7)}$$

Then, the authors neglect the effect of the inertia. Hence, the circuit represented in Figure 4.6 is described mathematically by the following ordinary differential equation:

$$C\dot{p}_c + \left[\frac{p_c - p_{out}}{R_2}\right] = v_{in}\left[\frac{p_{in} - p_c}{R}\right] \qquad \text{Eq(4.8)}$$

Where pressure and volume are related by the compliance C described in Eq(4.2). Pin and pout represent the potential at the inlet and outlet while v_{in} is defined as:

$$v_{in} = \begin{cases} 0 & p_c > p_{in} \\ 1 & p_c \leq p_{in} \end{cases} \qquad \text{Eq(4.9)}$$

The above formulation is able to reproduce lymphatic property starting from anatomical structures (radius, length) and fluid-dynamic observations.

Another possible lumped representation is described in [23]. Starting from the analogy of behaviour between heart and lymphangions pumping characteristics, they proposed to use the ventricle model of Quartertoni described in Section 3.2.2 to investigate physiological characteristics of the lymphangion.

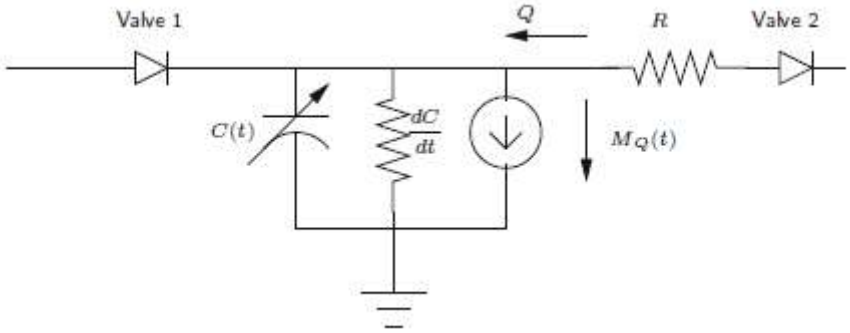

Figure 4. 7: Model of a lymphangion proposed by [23]

4.1.2 Lumped model of the lymphangion

Based on the review of models described in section 4.1.1, we now define a lumped parameter model of the lymphangion starting from the analogy of behaviour with the heart.

Specifically, we will rely on the approach defined by Quick et al [18] and later by Venugopal, i.e. we consider a time-varying elastance to describe pumping characteristics of this vessel.

Moreover, in [38], the authors observed how "An analytical description of the normalized elastance curves …. expressed as function of pressure and flow, may provide a solid basis for use in modeling lymphatic vessels". Interestingly, time-varying elastance model of Avanzolini (described in chapter 3.4) was developed starting from a linearization procedure applied to a pressure-volume relationship. Hence, we decide to use this latter model to study lymphangions' behavior. We will implement and adapt the formulation to reproduce the contractile property of these vessels. We will maintain the same structure only calibrating its parameters, which are expected to change because of the different pressure and volumes of the lymphatic system compared to the heart. Hence, we expect a different P-V loop and, consequently, different parameters in the elastance model (Eq 3.1).

It is worth observing that the presence of the hysteresis loop in the lymphangion is reported in a series of paper of Huxley and Scallan [7],[35] as well as in [39].For instance, in [39], they initially stated again how "lymphatic vessels share functional and biochemical characteristics with cardiac muscle".

Then, they isolated a single rat's lymphangion and pressurized it for an-vitro study. The authors recorded both pressure and diameter during each contractile cycle obtaining the graph shown in Figure 4.8.

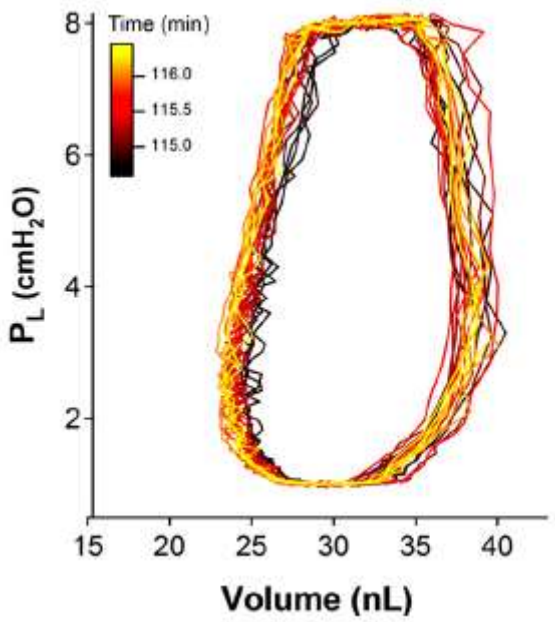

Figure 4.8: P-V loop in the lymphangions (from[39])

Figure 4.8 is useful to provide some qualitative insights regarding the expected shape of the P-V loop in the lymphangions. Specifically, we can observe how volumes involved are very small compared to the pressure. This is a typical feature of these contractile vessels, that can generate high pressure even though their small dimension.
Nevertheless, we can't use this P-V loop to calibrate our model because these measurements stem from rats while we are describing the human lymphatic system, where pressure and volume are different (see section 4.2.1). Unfortunately, human measurements on lymphatic system are very scarce so that we need again to face the difficulties of introducing and calibrating a numerical model.

4.1.3 Lumped parameter modelling of lymphangion contractility based on Avanzolini time-varying elastance

The objective of this section is to reproduce the contractility characteristics of lymphangions starting from Avanzolini time-varying elastance model of the heart. In this lumped description, the ventricle was able to generate its force of contraction thanks to the ideal potential source (called U_L In Figure 3.21). This element generates the isovolumic pressure U, defined as

$$U = a(t) \cdot P_0(V_0) \qquad \text{Eq(4.10)}$$

U(t) depends on the activation function and is characterized by the sinusoidal shape reported in Figure 4.9.

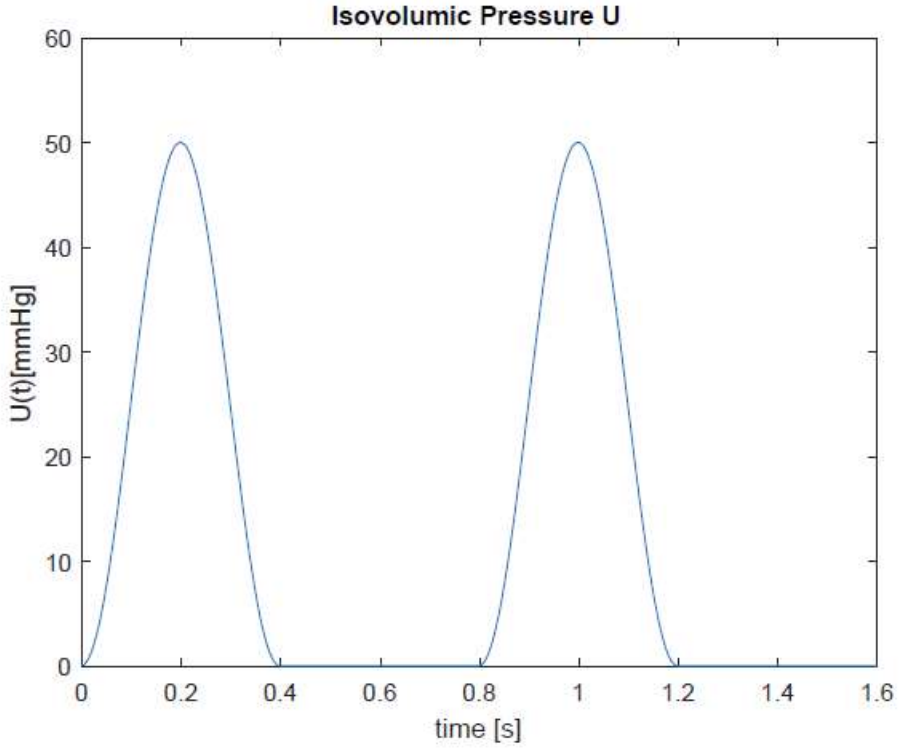

Figure 4.9: Isovolumic pressure in the heart

However, the force of contraction of the heart is different compared to the one of the lymphangions as can be seen for instance in the different P-V loop (Figure (3.8) and Figure (4.8)).
Hence, we must adapt the parameters of the ideal potential source to reproduce the contractility of the lymphangions. From [7], we can observe the characteristic shape of pressure experienced by a lymphangion during a contractile cycle (see Figure 4.10).

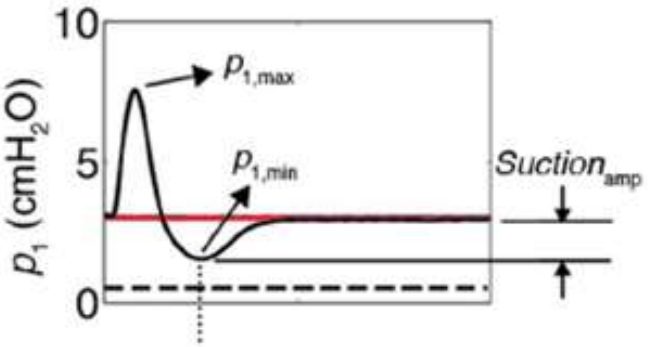

Figure 4.10: time rate of change of pressure inside a lymphangion

This curve is representative of the contractility of the lymphangions. Hence, we need to modify the ideal potential source of the model to reproduce this pressure waveform. To pursue this aim, we modify empirically the activation function a(t) as follows:

$$a(t) = \begin{cases} \left[1 - cos\left(\frac{2 \cdot \pi \cdot T_m}{T_s}\right)\right] \cdot \frac{1}{3} & systole \\ -\left[1 - cos\left(\frac{2 \cdot \pi \cdot T_m}{T_s}\right)\right] \cdot \frac{4}{3} & diastole \end{cases} \quad \text{Eq (4.11)}$$

As opposed to the one of the ventricle

$$a(t) = \begin{cases} \left[1 - cos\left(\frac{2\pi t}{t_c}\right)\right]/2 & systole \\ 0 & diastole \end{cases} \quad \text{Eq (4.12)}$$

Comparing Eq(4.11) with Eq(4.12), we can observe how the relaxation phase (diastole) of the lymphangion is modelled with a sinusoidal function. This second moment of the activation function enables us to reproduce the dip reported in Figure (4.6). The duration of both contraction and relaxation phases have been assumed to be equal. It is called T_s and is obtained from the following relationship (described in Avanzolini):

$$Ts = a + Tc \cdot b \quad \text{Eq(4.13)}$$

where

- a and b are two parameters which will be calibrated and that will define duration of both systole and diastole phase;
- Tc is the contraction phase (about 10 s according to [7],[40]).

Finally, the relationship characterizing the ideal source generator will be the

$$U(t) = \begin{cases} U_0 \cdot \left[1 - cos\left(\frac{2 \cdot \pi \cdot T_m}{T_s}\right)\right] \cdot \frac{1}{3} & systole \\ -U_0 \cdot \left[1 - cos\left(\frac{2 \cdot \pi \cdot T_m}{T_s}\right)\right] \cdot \frac{4}{3} & diastole \end{cases} \quad \text{Eq (4.14)}$$

All those elements will be calibrated later when this compartment will be introduced into the global model. This potential source will be coupled with a capacitor to define the pressure experienced by the lymphangion. Regarding the latter element, we maintain the same relationship of Avanzolini describing the capacitance as

$$C = E_d + E_s \cdot a(t) \quad \text{Eq(4.15)}$$

where E_d and E_s should represent the EDPVR and ESPVR of the P-V loop of the lymphangion.
However, given the lack of such plot for humans in the literature, we calibrated it empirically.
We must highlight that this empirical calibration is a consequence of the physiological uncertainty regarding mechanisms leading to lymphangions contraction.

4.2 Initial lymphatic and the interstitial space

In this section we will define the final configuration of the model of human fluid balance. Specifically, we must define the hydraulic connection between the compartment of the lymphangions with the interstitial space and the cardiovascular system as reported in Figure 4.11.

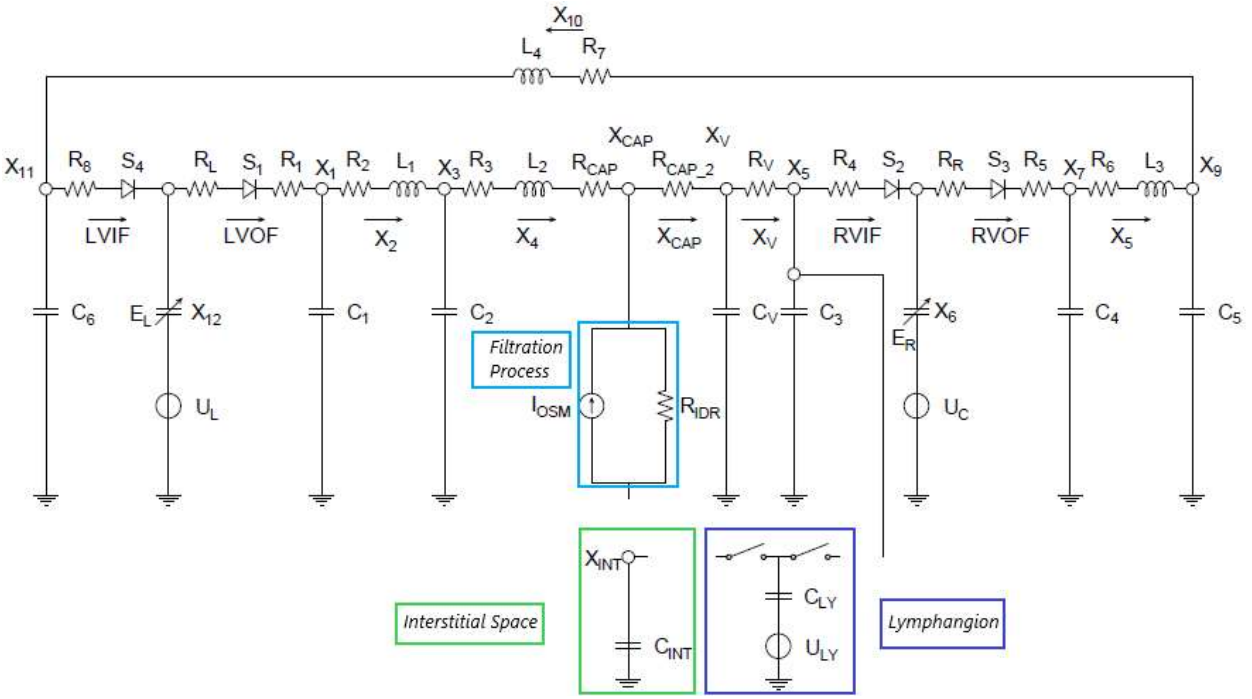

Figure 4.11: Connection of the lymphatic system with the cardiovascular space

However, this procedure is not straightforward because of the presence of open question in the physiological literature regarding both the lymphatic system and the interstitial space.
Specifically, the uncertainty stems from:

- The subatmospheric pressure in the interstitium [41]. Although this peculiar feature of the interstitial space was firstly observed experimentally in 1968 by Guyton, factors leading to this negative pressure are yet not clear [40], [41];
- Problem of lymph formation in the lymphatic system (see Figure 3.32). This term refers to the entry of fluid and protein into the initial lymphatics and according to "... the mechanism responsible for this process are poorly understood"[10].

These problems significantly affect our modelling effort. If we want to describe human homeostasis, the model should be able to product a flux from the interstitium toward the lymphatic system. Meanwhile, this flux must be established from a subatmospheric condition into the interstitial space. Hence, although the physiological uncertainty regarding those mechanisms, the objective is to find the combination of electric elements allowing us to:

- Observe a negative pressure in the interstitium;
- Connect the lymphatic system with the cardiovascular system.

In this perspective, our proposed model will provide a general framework to investigate the interaction between compartments. Specifically, we will test different hypotheses and verify their impact by a systemic point of view.
Hence, throughout this section, we will test two different configurations to connect the lymphangions with both cardiovascular circulation and the interstitial space and we will verify the systemic impact of our modeling. The implemented electric circuit will be solved in OpenModelica.

4.2.1 Connection between lymphatic and interstitial space based on passive elements

To model the complex interaction between the lymphatic system and the interstitial space, we initially consider only passive elements as represented in Figure 4.12.

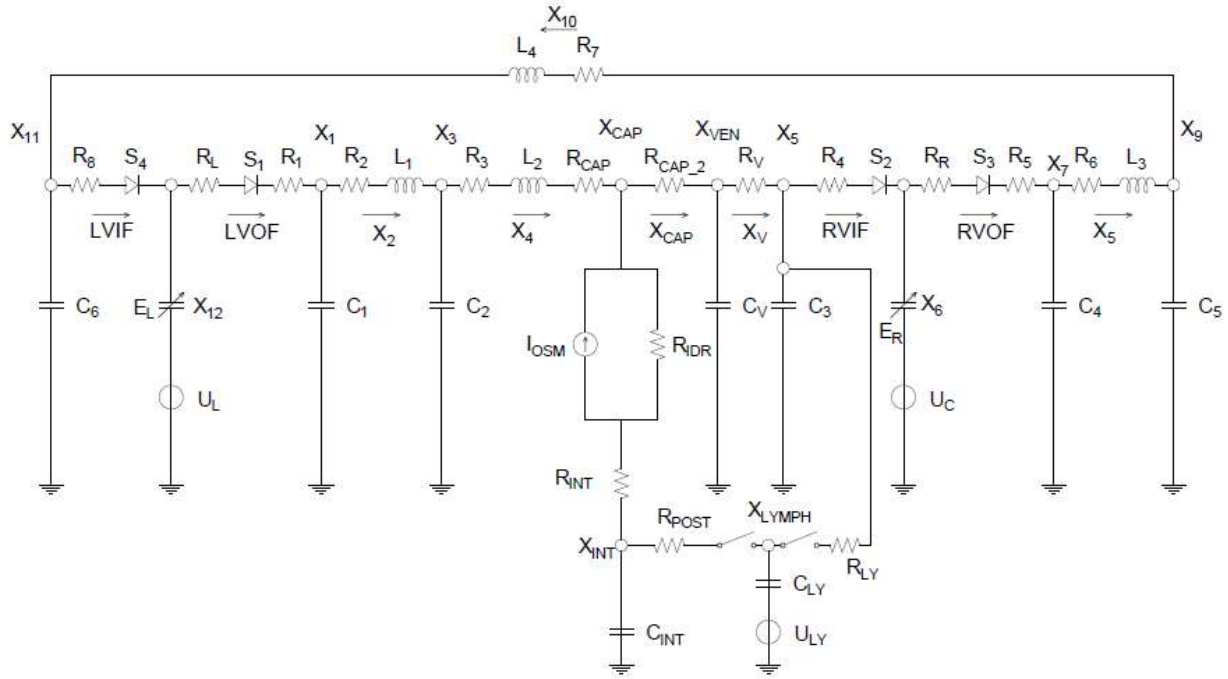

Figure 4.12: lumped parameter model of fluid balance with a passive connection between the microcirculation and the cardiovascular system

As can be seen above, we introduce two resistors, R_{INT} and R_{POST} which represent the viscous losses experienced by the fluid in the transition from the capillaries toward the interstitium. Similarly, we consider another resistor, called R_{LY}, describing the hydraulic resistance and consequent losses caused by lymph movement throughout the lymphangions' chain.
Moreover, we introduce two diodes representing the secondary valves of the lymphangions which govern allow the unidirectional movement throughout lymphatic system. The outlet one (*OUT_VALVE* in Figure

4.12) is modelled in OpenModelica with the diode presented in Chapter 3. Its behaviour is controlled by the pressure in the lymphangion compartment (X_{LYMPH}) and the veins one (X5). Specifically:

- If $X_{LYMPH} > X_5$, the diode is closed and it allows the flux from lymphatic system towards the venous side;
- If $X_{LYMPH} < X_5$, the diode is open to prevent retrograde flow;

Regarding the upstream one we consider a slightly different diode representation.
Specifically, we implement in OpenModelica the class reported in Figure 4.13.

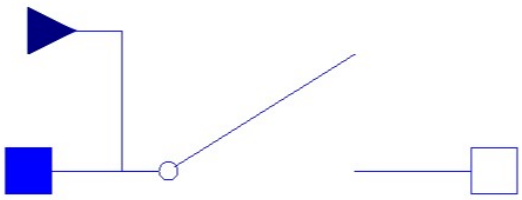

Figure 4.13: Inlet valve of the lymphangions compartment

This element behaves as follows:

- when the lymphangion is contracting, the diode is open. As a matter of fact, during the contraction pressure in the lymphangions compartment increases. Hence, we can reasonably hypothesize a unidirectional flow from the lymphangion compartment towards the venous side and the absence of flow from the interstitial space to the lymphatic system, i.e. the diode is open;
- conversely, when the lymphangion is in the relaxation phase, we expect a flux from the interstitial space toward the lymphatic system and the diode is closed.

Hence, diode's behavior depends on contractility of the lymphangion, i.e. on the ideal potential source introduced in section 4.1.3. In Open Modelica this modelling is made possible by connecting the diode's interface with the pressure source of the lymphangion.

Calibration procedure

Now, we need to pursue the calibration of both resistance and parameters characterizing the time varying-elastance. The objective is to find values of those elements resulting in a physiological range of pressure at the electric node called $X_{\_INT}$, which represents the interstitial space. As described before, we expect this pressure to be, on average, in the subatmospheric range. Meanwhile, a flux must be established from the interstitium towards lymphatic compartment.
Through this procedure we know:

- the physiological range of value of the resistance and of the ideal current source describing the filtration process (section 3.5.3);
- the parameters of the cardiovascular circuit. They have been already calibrated and we expect them not to change in a significant matter because volume involved in the microcirculation are smaller compared to the one involved in cardiovascular circulation;
- the electrical representation of the lymphangion based on the time-varying elastance.

Regarding the last item in the list, after an iterative procedure we consider the following parameter for the lymphangion

UO	2	mmHg
ED	0.0084	mmHg / cm^3
ES	0.42	mmHg / cm^3
Tc	13.26	s
a	0.08	s
b	0.045	-

Table 4.1: Parameter value of the proposed lumped parameter model of the lymphangion

This calibration leads to the time-rate of change of pressure in the lymphangion compartment reported in Figure 4.14.

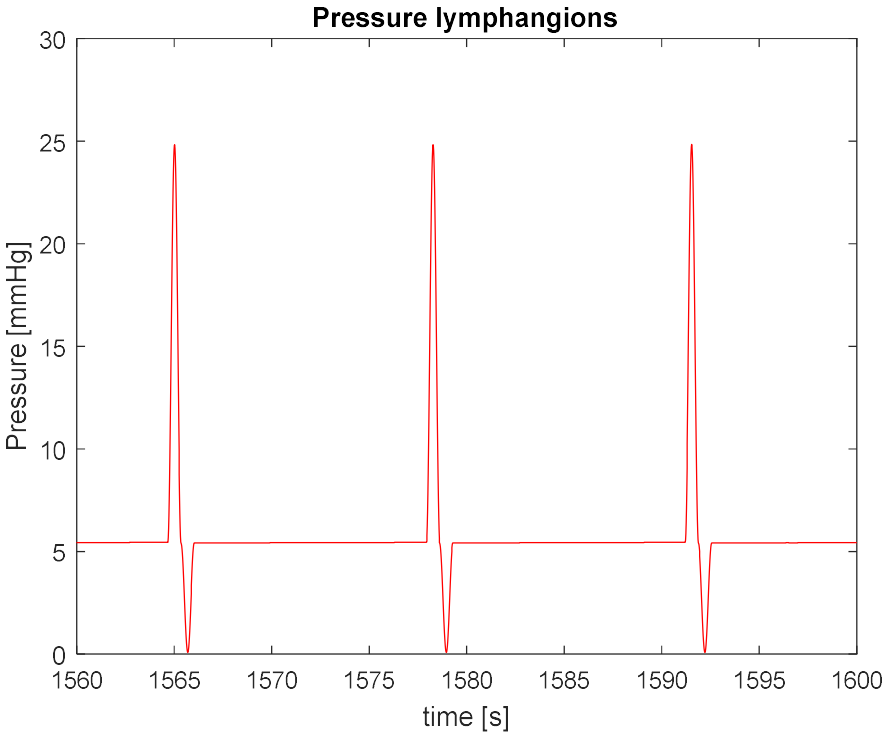

Figure 4.14: Time-rate of change of pressure in the lymphangion compartment

As it can be observed, there is a faster recovery in our curve compared to the one reported in [7]. However, we considered this approximation as acceptable because, experimental measurements in [7] has been obtained from rat, while our objective is the definition of a computational environment for humans. Thus, we aim at reproducing the waveform rather than try to find an exact match between the absolute values of the pressure reported in the literature. As a matter of fact, a similarity in the waveform means that we are correctly capturing the main features of the lymphatic physiology

The difference regarding pressure is even bigger (25 mmHg compared to 6 mmHg). However, measurements performed in Unno [5] using a non-invasive technique, showed that the pressure in the lymphangions on human volunteers was $29.3 \pm 16\ mmHg$, which is very close to the evaluation of Figure 4.14.

Given these observations, we considered the calibrated model to be capable of describing an average physiological condition in human lymphangions. At the same time, the parameters in the circulation were slightly affected by this calibration procedure and we maintained for them the same values described in Chapter 3. Regarding the filtration process, we consider the following values:

R_Idr	3.03	mmHg· s/cm^3
I_Osm	6.5	cm^3

Table 4. 2: Parameter value of the proposed lumped parameter model of the filtration process

However, in this passive configuration, we are not able to observe a subatmospheric pressure in the interstitial space. For instance, we can consider the combination of resistance parameters reported in Table 4.3.

R int	To be calibrated
R post	12.5
Rly	12.5

Table 4. 3: calibration of resistance value in the passive configuration varying R_{INT}

Maintaining fixed both R_{POST} and R_{LY}, we can study the effect of R_{INT} on the interstitial pressure as showed in Figure 4.15.

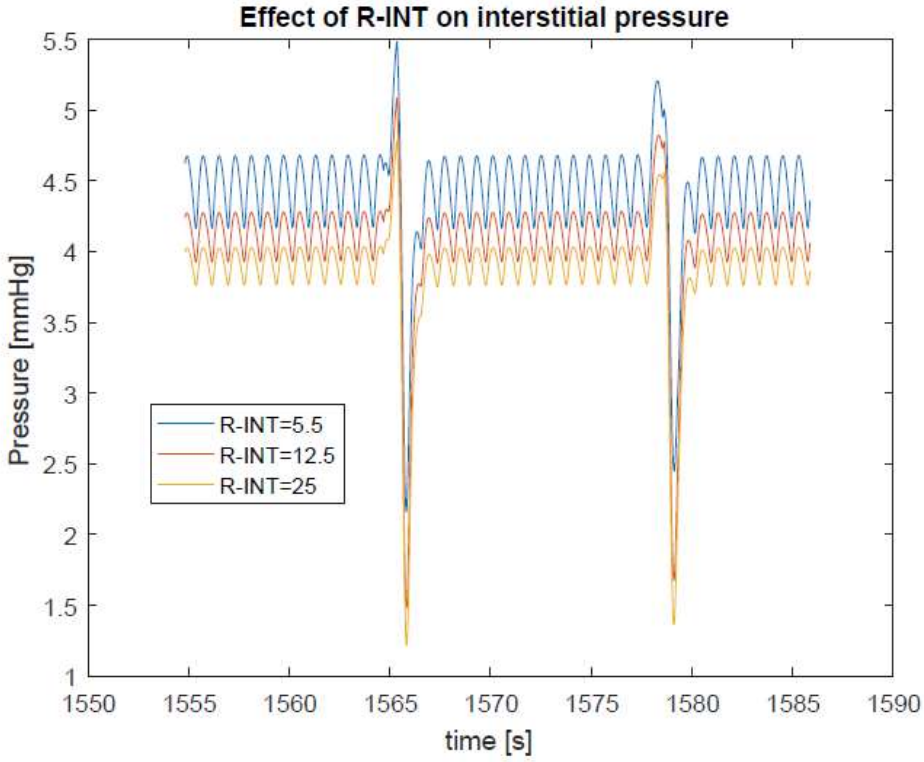

Figure 4.15: Effect of R_{INT} on the interstitial pressure

We are reporting the plot of pressure into the interstitium and, against our physiological expectation, we observe a positive value of pressure, as it can be seen in Figure 4.15. Increasing the value of the resistance, we can observe a progressive lower value of the pressure of the interstitial space but not enough to obtain a negative value as we physiologically expect. Furthermore, we can observe a reduction of the amplitude of pressure oscillation decreasing the value of the resistance.
Considering a similar analysis with the resistor called R_{POST} we can observe an analogous behaviour. Specifically, in this case the parameter values vary according to the following table:

R int	12.5
R post	To be calibrated
Rly	12.5

Table 4.4: calibration of resistance value in the passive configuration varying R_{INT}

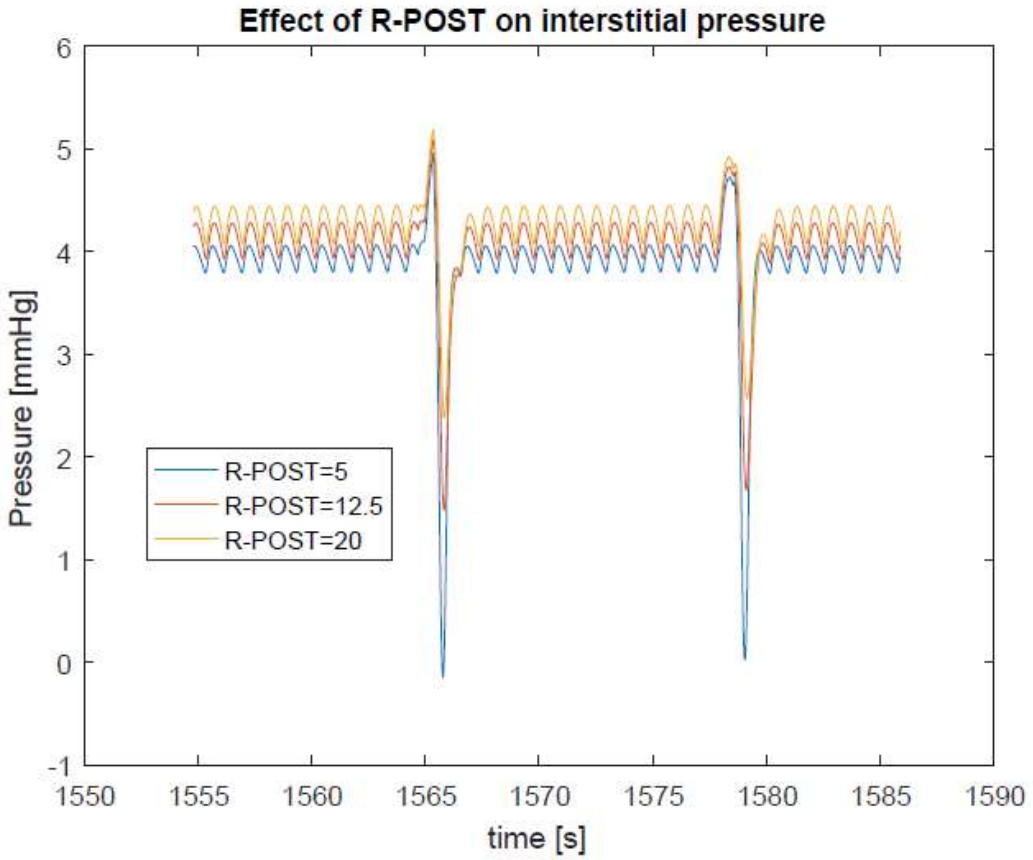

Figure 4.16:Effect of R_{POST} on the interstitial pressure

We can notice how increasing the value of the resistance we increase the pressure in the interstitium.
As a result, also in these other tested configuration we are not able to find a subatmospheric pressure.
Modifying the parameter of R_{LY}, we have an even smaller effect on interstitial pressure. Hence, we can conclude that with a combination of passive elements connecting cardiovascular and lymphatic system we are not able to describe the peculiar feature of the interstitial space, i.e. the subatmospheric pressure.
This observation naturally introduces us in the next section where a different electric configuration is proposed and numerically tested.

4.2.2 Adding a current source

Starting from the observation of the previous model, we decide to introduce a current generator source between the interstitial space and the lymphangion compartment. By doing that, the electric circuit can be represented as in Figure 4.17.

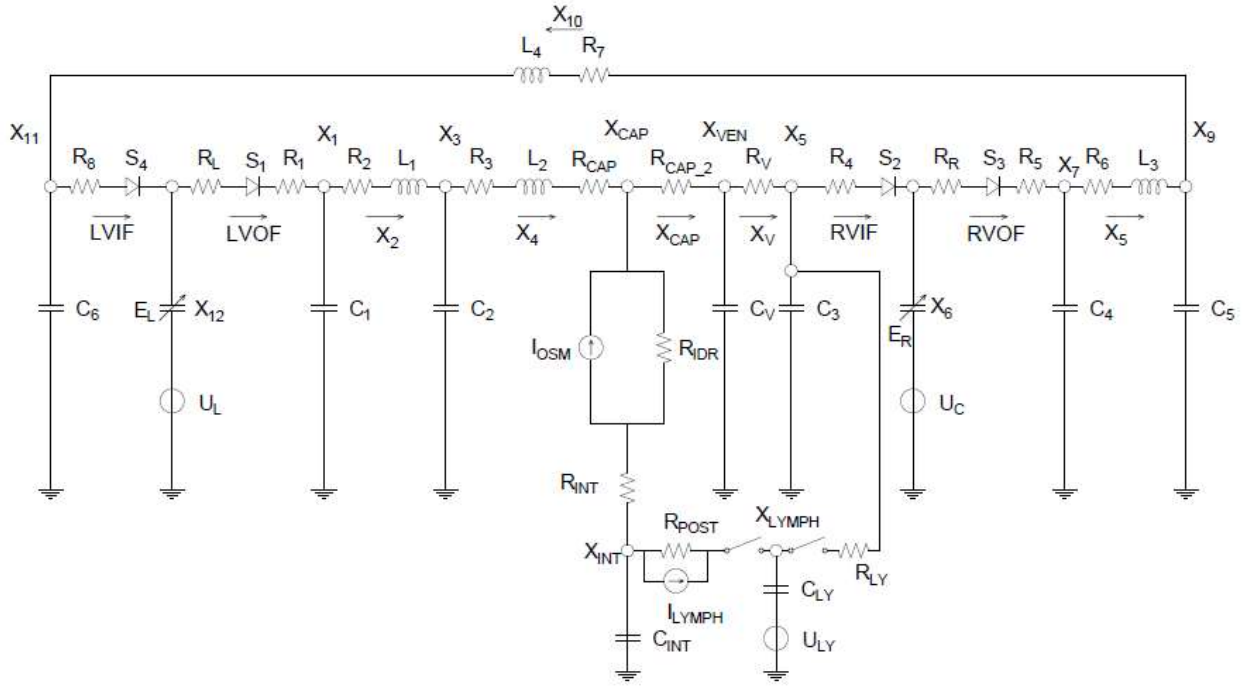

Figure 4.17: Lumped parameter model of fluid lumped balance with the addition of the current source

Also in this situation we performed a parameter calibration. After that procedure, we assign a value of 0.6 cm^3 to the current source I_{LYMPH}. Moreover, maintaining:

- The same value of the electrical elements characterizing the filtration process;
- The already described parameters for the lymphangion

and considering the following the value of the resistors reported in Table 4

R int	12.5	mmHg· s/cm^3
R post	12.5	mmHg· s/cm^3
Rly	15	mmHg· s/cm^3

Table 4. 5: Parameter value of the resistance in the model configuration with a current source

We obtain the following behaviour of pressure into the interstitial fluid:

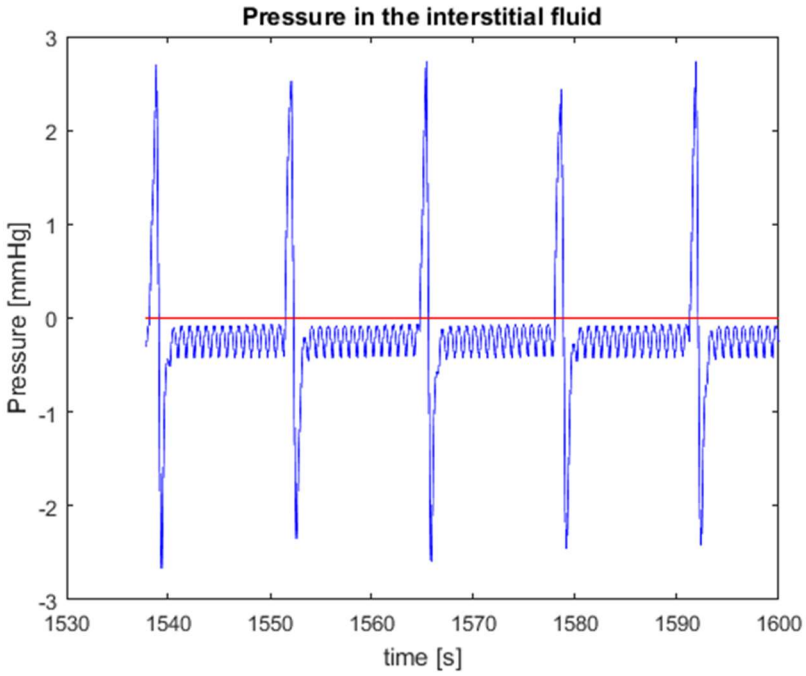

Figure 4.18: Pressure in the interstitial space after the introduction of a current source

As can be observed, introducing a current source leads to an average negative value of the pressure in the interstitium. This result agrees with the physiological expectation ad constitutes a fundamental step to build a consistent model of the human fluid balance. By a physiological point of view, the introduction of a current source is consistent because it describes the process of lymph formation. As already said, the latter term refers to the entry of fluid and protein into the initial lymphatic from the interstitial space and it is represented in Figure 4.19 as J_{lymp} .

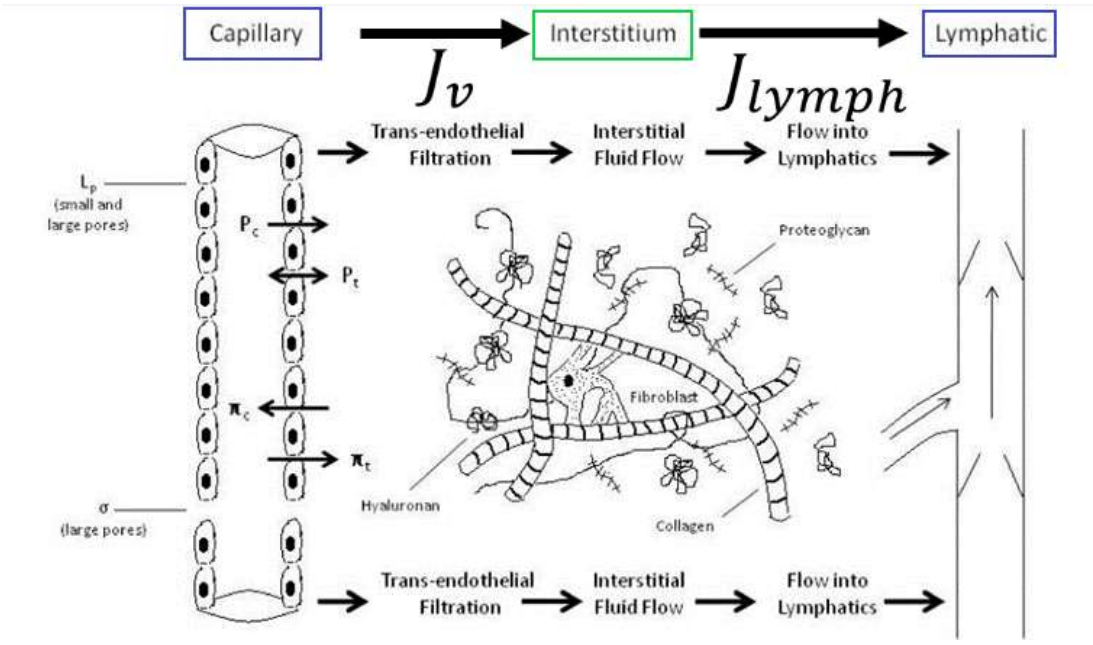

Figure 4.19: process of lymph formation

Despite its crucial importance in human homeostasis, it is not clear which is the mechanism leading to the formation of lymph flow from a subatmospheric pressure condition in the interstitium. In the literature there are three main hypotheses regarding that:

- a convective flow caused by a protein concentration gradient [10];
- a hydrostatic pressure gradient from the interstitial space even with an average subatmospheric pressure condition [41];
- Opposite to what already said, a variant of the hydrostatic pressure hypothesis posits that spontaneous contractile lymphatic lymphangions, during their relaxation phase, are able to generate a suction force drawing interstitial fluid into the initial lymphatics [10].

We can summarize these concepts by simply stating that from a hydraulic and electric points of view, we need a positive flow from the interstitial space towards the lymphatic. This flow must be guided by an adverse pressure gradient or by a gradient generated by a protein concentration. In our mathematical modelling, the current generator source mimics exactly this flow in the initial part of the lymphatic system. Additionally, the latter electric element was shown to play a crucial role in the maintenance of a negative pressure in the interstitium. Hence, the conclusion of our model is an influence of the lymphatic system in maintaining a subatmospheric pressure into the interstitium, as hypothesized by Guyton [9].
This would imply a tight functional relation between the lymphatic and the interstitium in the overall maintenance of a homeostasis condition (for instance, the pressure in the interstitial space regulates the filtration process at the capillary side).
Based on the previous conclusion, our proposed model, to the best of our knowledge, seems be a first quantitative evidence of the conjecture proposed by Guyton.

4.3 Results of the model

In this section we present the results of our proposed model of human fluid balance.

4.3.1 Results

We report below the plot of the time-rate of change of pressure in the large arteries throughout 18 subsequent cardiac cycles. Specifically, in Figure 4.19, on the x-axis we report the period of a single cardiac (0.8 seconds) while on the y-axis we report pressure behaviour in each m-th cycle, m=1 ...18.

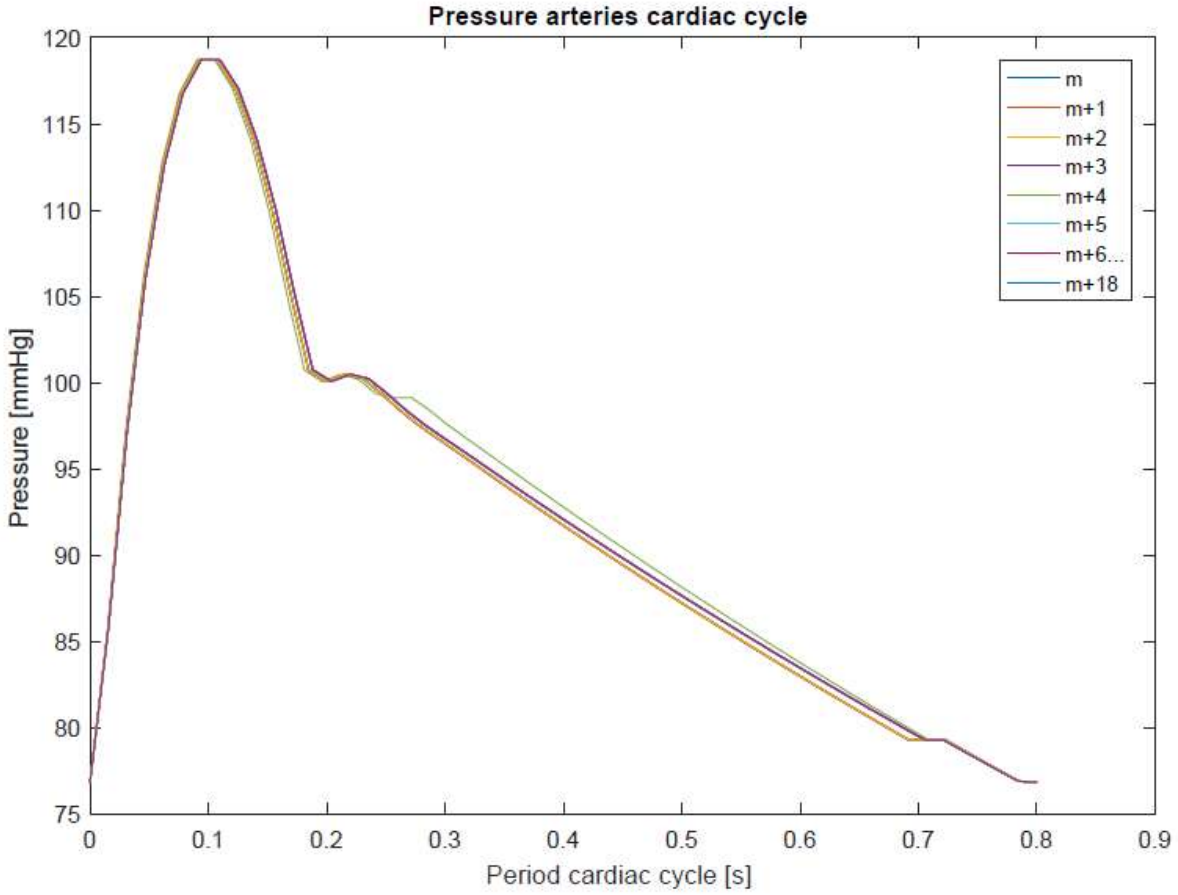

Figure 4.20: time of rate of change of pressure in the large arteries in m=1...18 subsequent cardiac cycles

Overall, this plot normalises 18 subsequent waveforms over a time frame of 14 s. Throughout this time frame, there is at least one contraction of the lymphangion whose contraction period is of 13.26s.
As we can see in the figure, we have a very small difference between the subsequent curves meaning that the lymphatic pumping has a small impact on the pressure behaviour of the large arteries.
This agrees with the physiological literature as the waveform we expect to observe is shown in Figure 4.20.

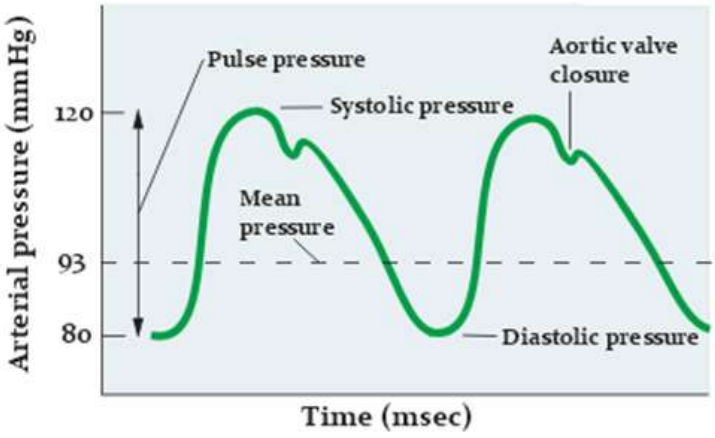

Figure 4.21: physiological expected aortic pulse pressure

The same situation can be observed in the capillaries. Considering the same time frame of 14 seconds, we subdivided that it into 18 subintervals of 0.8 second and we represent the behaviour of the pressure in Figure 4.22.

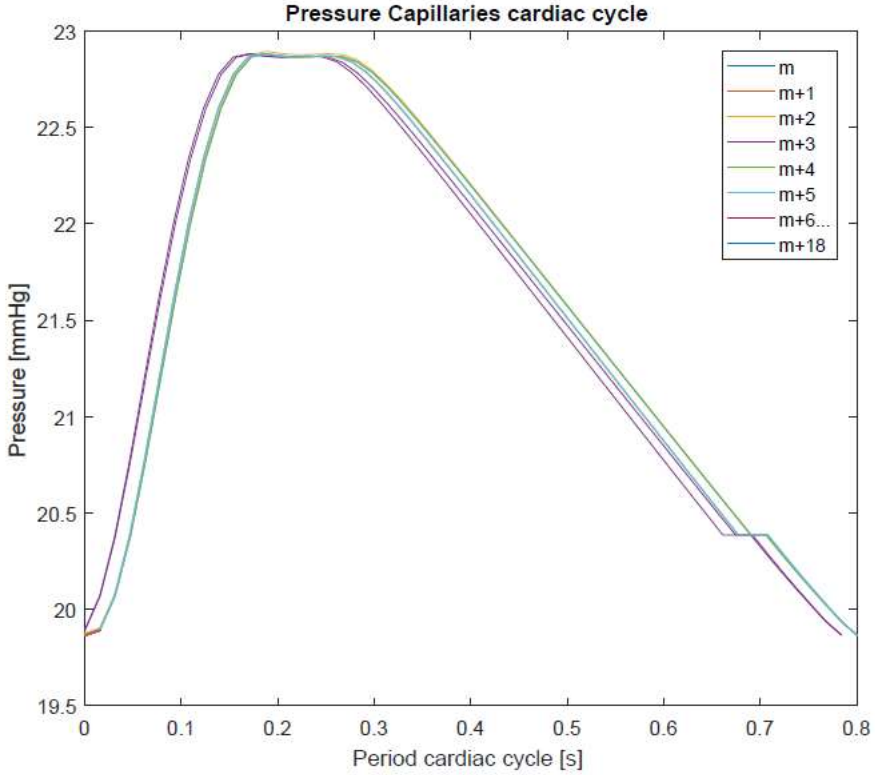

Figure 4.22: time of rate of change of pressure in the capillaries in m=1...18 subsequent cardiac cycles

The pressure waveform seems is not affected by lymphatic pumping and its pressure values are in the range of the physiological value, namely 20-30 mmHg [9][50]. In contrast, in the interstitial space we can clearly observe the influence of the contraction of the lymphatic system in time rate of change of pressure, as reported in Figure 4.23.

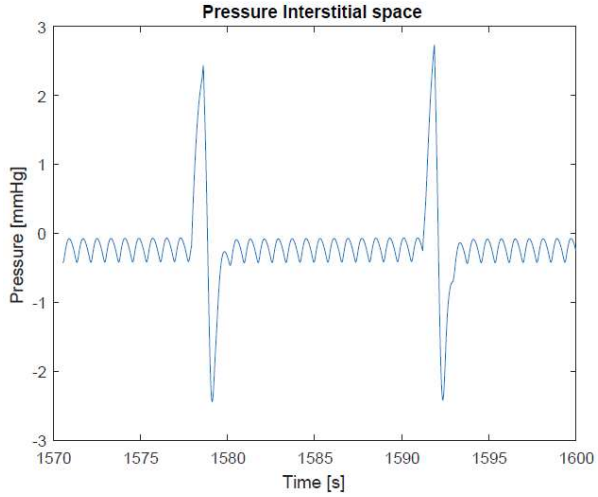

Figure 4. 23: time rate of change of pressure into the interstitium

In Figure 4.23 we can observe both the frequency of the waveform typical of the heart (so 0.8 seconds) as well as the one caused by the lymphangions (13 s). Pressure behaviour in both the compartments of the interstitial space, lymphangion and the capillary are reported and compared in Figure 4.24.

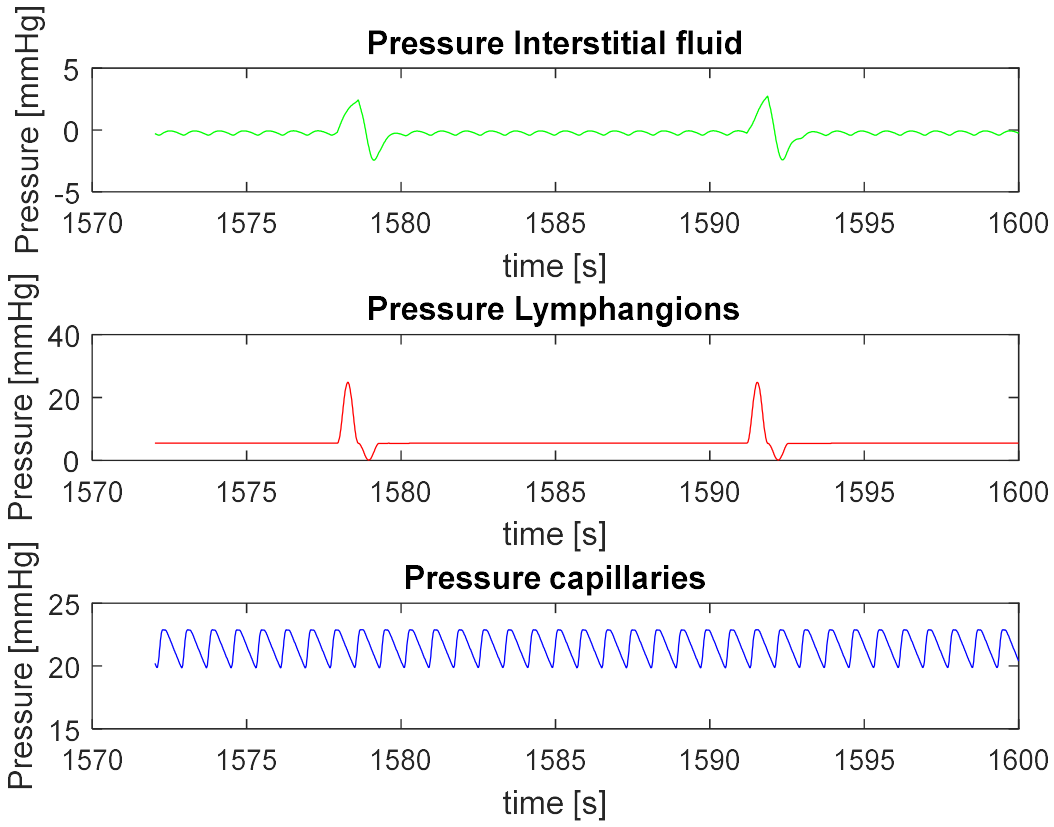

Figure 4.24: time rate of change of pressure in the interstitial space, in the lymphatic system and the capillaries

In Figure 4.24 we can observe how, during the silence period of the lymphangion, the pressure in the interstitial fluid is affected by the capillary compartment. Conversely, when the lymphangion contracts, the pressure in the interstitial space increases because the inlet valve is closed. Then, when the lymphangion ends its contraction phase, the diode closes allowing a flux which results in a reduction of the pressure in the interstitial space.

Furthermore, we can observe a hysteresis loop in the lymphangion which resembles the shape observed in the heart. In Figure 4.25 we compare both the hysteresis loop observed in the left ventricle as well as the one in the lymphangion. The shape of both agrees with physiological expectation [7],[35]. Moreover, we can notice how the heart experiences significant higher pressure and volume compared to the lymphatic system.

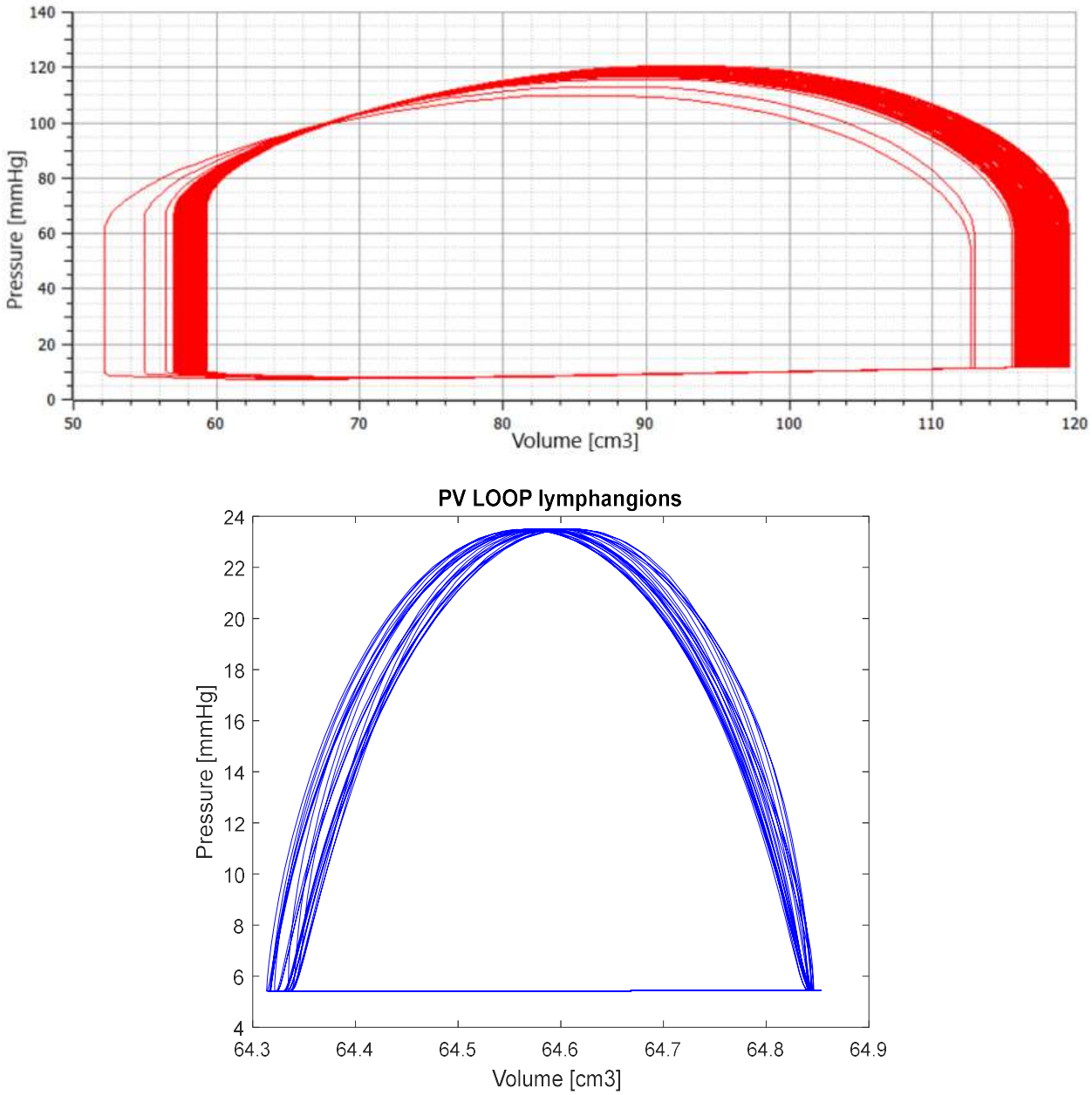

Figure 4.25: hysteresis loop in the lymphangion and in the left ventricle

Finally, we represent in Figure 4.26 the pressure in the interstitial fluid pressure and of the flow into the initial part of the lymphatic system.

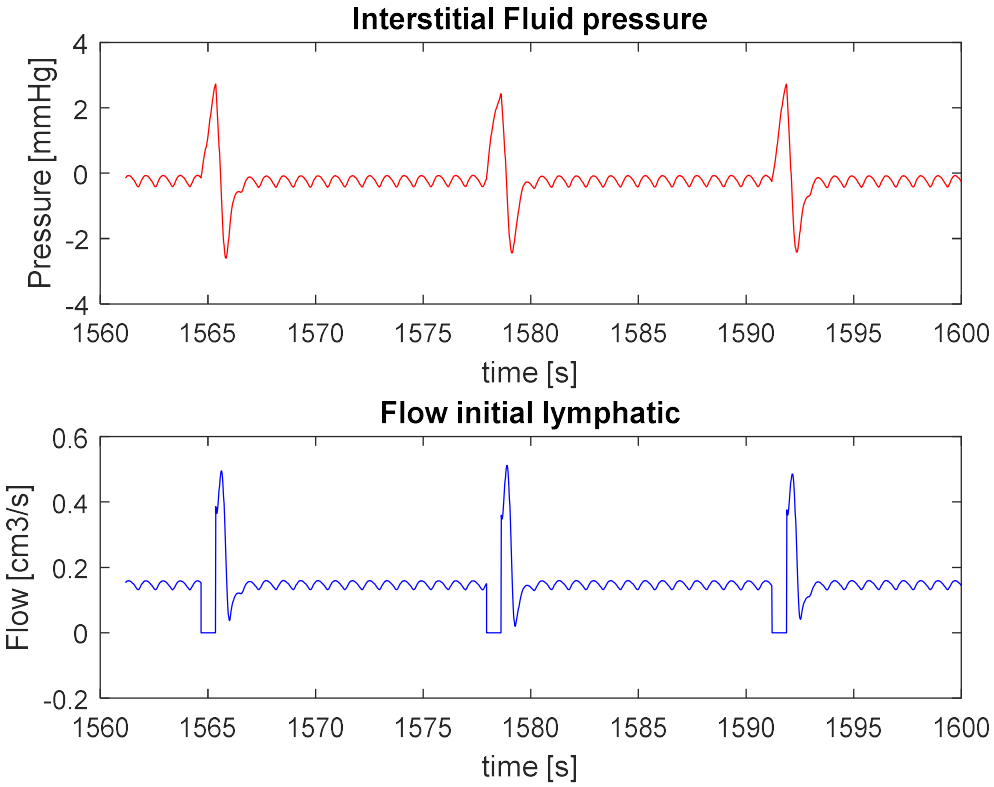

Figure 4.26: Comparison between pressure in the interstitial space and flow into the lymphatic system

As we can observe, the interstitial fluid pressure increases when the valve is closed, i.e. when the flow is equal to zero. At the end of the contraction phase, in agreement with the physiological expectation, valves open and we can observe a flow and consequentially we have a decrease of pressure.

4.3.2 Objective and next modeling directions to further develop the lumped parameter model

Starting from the conclusions of the circuit developed in section 4.3.1, we can hypothesize a coupled behaviour of the interstitial space with the lymphatic system in the overall fluid human balance. According to the results of our model, this coupling seems to influence both lymph formation as well as the maintenance of the negative pressure in the interstitium.

However, before investigating this possible coupled behaviour, we need to study more in detail the problem of lymph formation.

Although mechanisms leading to this flow are yet not established in the physiological literature, in a work recently published by Jamalian et Al. [7] the suction effect was proposed as a possible explanation.

Starting from experimental measurements on rat's mesenteric lymphangion, the authors pointed out how this mechanisms could be explained and demonstrated from the pressure "dip" in the time-rate of change of pressure reported in Figure 4.10.
More in details, they observed "…This suction opens the inlet valve and is required for filling in the presence of low upstream pressure. Positive transmural pressure is required for this suction, providing the energy required to reopen the vessel…. suction is transmitted upstream, allowing fluid to be drawn in through initial lymphatics.
From this considerations we can hypothesize the suction mechanism as the factor leading to lymph formation. However, the suction effect is a consequence of the contractility of the lymphangions. Hence, if we want to test quantitatively this hypothesis, we need initially to investigate more in detail the role of the contractile element in the latter mechanisms as summarized in Figure 4.26.

Figure 4. 27: schematic description of the suction effect

However, we decide to study this problem in a new computational environment, a CFD simulation.
As a matter of fact, our objective is now a study at a local scale of the lymphangions. Accordingly, a 3D simulations offers a more suited modelling for this target compared to a lumped approach, whose biggest strength is the systemic perspective.
Hence, in the next chapter we'll focus on the definition of the numerical set-up of a simulation of a lymphangions. We will investigate its fluid-dynamic behaviour to obtain possible insights regarding this suction effect.

CHAPTER 5
NUMERICAL 3D MODEL OF A SINGLE LYMPHANGION

The aim of this chapter is to define a 3D numerical model of a single lymphangion with ***FLOW-3D*** aiming at reproducing in-vivo measurements of lymphatic activity reported in [7]. In section 5.1 we describe the features of ***FLOW-3D***, the CFD commercial with which we simulate the problem at hand. Afterwards, in section 5.2 we illustrate the experimental work that serves as a reference and the main hypotheses of our proposed formulation. In Section 5.3 we describe the construction of the numerical model while in section 5.4 we discuss the obtained results and the improvements which can be made to optimize the simulation.

5.1 FLOW-3D

The simulation which will be described in these chapters are performed with ***FLOW-3D***, which is a commercial highly-accurate CFD software specialized in solving transient, free-surface problems.
FLOW-3D serves a broad range of applications, ranging from microfluidics, biomedical devices to water civil infrastructure.
The licence to access the content of this software has been provided by *XC-Engineering*, an engineer society of Cantù (Italy) specialized in fluid-dynamic simulation and numeric optimisation.
In this section we provide an overview of the features of the CFD software ***FLOW-3D***.

5.1.1 Structure of CFD software and features of FLOW-3D

Computational Fluid Dynamics (CFD) means computer solution of the equations governing the conservation of mass, momentum, and energy for a fluid. Those conservation equations are discretized and then solved to yield an approximate solution to the original problem.
The capability of a CFD software is the creation of a computational model which may be considered equivalent to set-up of an experiment. A general CFD software can be described according to the scheme reported in Figure 5.1.

Figure 5. 1 :Structure of a CFD software

We will discuss briefly the three parts highlighting peculiar features of ***FLOW-3D***.

Pre-processing

In the pre-processing we define properties of the fluid we want to simulate as well as the geometry of our simulation, which will constitute the computational domain of our simulation. The geometry is then discretized into a number of control volume which will define the mesh of our problem. Moreover, ***FLOW-3D*** has several physical models which are already implemented and are useful to include physical mechanism in the simulations such as viscosity, turbulence or moving object

Solver

This step involves the discretization of the system of PDE governing the problem. In ***FLOW-3D***, spatial discretization follows the finite volume approach. After this procedure, we obtain a system of algebraic equation which is solved for each cells of our numerical domain.

Post-processing

The outputs of the simulation are represented and analyzed to study time and space evolution of the relevant variable. This process can be done with ***FLOW-SIGHT***, a post-postprocessing tool combined with ***FLOW-3D.***

5.1.2 *FLOW-3D* grid and the FAVOR™ method

The mesh subdivides the physical space of the simulation into control volumes where calculations take place. The ***FLOW-3D*** approach is to use an orthogonal mesh defined in terms of either cartesian or cylindrical coordinate. The mesh is defined independently of the geometry. The primary advantage of this approach is that geometrical objects can be added, removed, or moved without affecting the mesh.
On the other hand, governing equations must be re-derived to account for both geometry and flow effects within a control volume.
This procedure is done with a method called FAVOR™ (fractional area/volume obstacle representation), which is the algorithm used in ***FLOW-3D*** to embed geometry effects in the conservation equations for each control volume. This method computes the area fractions on the cell faces along with the volume fraction

open to flow to define the location and orientation of solids in the mesh. Specifically, seven quantities are used to represent geometry in the governing equation:

- six area fractions (one for each face of the cell), which represents the ratio of the open area to the total area of the cell face;
- one volume fraction (ratio of the open volume to the total volume of a cell);

Afterwards, ***FLOW-3D*** calculates the cell face area blocked by the component and then draws a flat surface linearly across the cell from one face to another as reported in Figure 5.7.

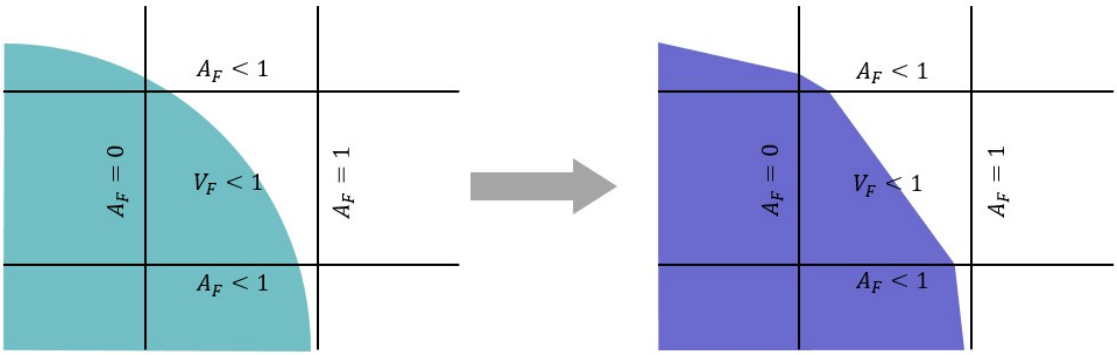

Figure 5. 2:Mesh discretization with FAVOR™

Both area and volume fractions are then included in the governing equation of the software as it will be illustrated in the next section. It is worth noting that each component must occupy at least one grid intersection point in order to generate enough fractional area data to resolve. Components that don't occupy at least one mesh intersection will be lost completely.

An additional feature of ***FLOW-3D*** is the multi-block gridding. Hence, we can have multiple mesh-block in a simulation each of them spanning a certain region of the whole flow domain. With ***FLOW-3D*** the mesh blocks can be of two types: rectangular blocks (Cartesian coordinates) or cylindrical blocks (cylindrical coordinates). The blocks of rectangular mesh can then be placed side by side or inserted one inside the other (going to refine the regions where it is useful to do it).

5.1.3 Governing equation in FLOW-3D

Mass balance

The more general form of the mass balance equation is given by:

$$\frac{\partial \rho(\underline{x},t)}{\partial t} + \nabla \cdot (\rho\,(\underline{x},t) \cdot \underline{v}(\underline{x},t)) + \nabla \cdot (\underline{\gamma}(\underline{x},t)) + \ \beta = 0 \qquad \text{Eq(5.1)}$$

where

- the vector valued γ represents a flux through the boundary;

- β represents the net production rate (according to the sign of β, the last term in the right hand side will act as a source or as a sink)

In FLOW-3D the mass-source term of fluid β is considered, and the more general form of the continuity equation based on FAVOR™ method is

$$\frac{\partial}{\partial t}(\rho V_f) + \nabla \cdot (\rho \underline{v} A) = S_m \qquad \text{Eq(5.2)}$$

where S_m is a physical mass source term, V_f and A are volume and area fractions.
V_f and A are constant if we have stationary obstacle problems while they vary with time in presence of moving objects problems (it will be further explained in section 5.2.1 when the GMO physics will be introduced).If we rewrite Eq(5.3) component-wise, we get

$$\frac{\partial}{\partial t}(\rho V_f) + \frac{\partial(\rho\, uA_x)}{\partial x} + \frac{\partial(\rho\, vA_y)}{\partial y} + \frac{\partial(\rho\, wA_z)}{\partial z} = Sm \qquad \text{Eq(5.3)}$$

This is how the governing equation is implemented in a cartesian coordinate system.
Since we will consider cylindrical geometry, we need to introduce additional term representing the change of coordinates. The more general equation reads as

$$\frac{\partial}{\partial t}(\rho V_f) + \frac{\partial(\rho\, uA_x)}{\partial x} + R\frac{\partial(\rho\, vA_y)}{\partial y} + \frac{\partial(\rho\, wA_z)}{\partial z} + \xi\frac{\rho\, uA_x}{x} = RSOR \qquad \text{Eq(5.4)}$$

The coefficient R and ξ depends on the choice of coordinate system in the following way. If we use a cartesian mesh R = 1 and $\xi = 0$. When cylindrical coordinates are used, R = $\frac{r_m}{r}$ and $\xi = 1$.
Moreover, the y derivatives must be converted to azimuthal derivatives,

$$\frac{\partial}{\partial y} \rightarrow \frac{1}{r}\frac{\partial}{\partial \theta} \qquad \text{Eq(5.5)}$$

This transformation is accomplished by using the equivalent form

$$\frac{1}{r}\frac{\partial}{\partial \theta} = \frac{r_m}{r}\frac{\partial}{\partial x} \qquad \text{Eq(5.6)}$$

Where r_m is a fixed reference radius.

Momentum balance

For a Eulerian reference system, the conservation of momentum reads as

$$\rho \frac{\partial \underline{v}}{\partial t} + \rho \underline{v} \cdot \nabla \underline{v} + \underline{v}\left(\beta - \nabla \cdot \underline{\gamma}\right) = \nabla \cdot \underline{\underline{\boldsymbol{T}}} + b_i \qquad \text{Eq(5.7)}$$

If we assume a Newtonian fluid, an incompressible fluid and β, γ, $\underline{b}$ equal to zero, we get

$$\begin{cases} \rho \frac{\partial u}{\partial t} + \rho\left(u\frac{\partial u}{\partial x} + v\frac{\partial u}{\partial y} + w\frac{\partial u}{\partial z}\right) = -\frac{\partial p}{\partial x} + \mu\left(\frac{\partial^2 u}{\partial x^2} + \frac{\partial^2 u}{\partial y^2} + \frac{\partial^2 u}{\partial z^2}\right) \\ \rho \frac{\partial v}{\partial t} + \rho\left(u\frac{\partial v}{\partial x} + v\frac{\partial v}{\partial y} + w\frac{\partial v}{\partial z}\right) = -\frac{\partial p}{\partial y} + \mu\left(\frac{\partial^2 u}{\partial x^2} + \frac{\partial^2 u}{\partial y^2} + \frac{\partial^2 u}{\partial z^2}\right) \\ \rho \frac{\partial w}{\partial t} + \rho\left(u\frac{\partial w}{\partial x} + v\frac{\partial w}{\partial y} + w\frac{\partial w}{\partial z}\right) = -\frac{\partial p}{\partial z} + \mu\left(\frac{\partial^2 u}{\partial x^2} + \frac{\partial^2 u}{\partial y^2} + \frac{\partial^2 u}{\partial z^2}\right) \end{cases} \qquad \text{Eq(5.8)}$$

Considering the presence of mass sources and geometries that obstruct the flow, and dividing everything by density, Eq(5.9) is described in ***FLOW-3D*** as follows

$$\begin{cases} \frac{\partial u}{\partial t} + \frac{1}{V_f}\left(uA_x\frac{\partial u}{\partial x} + vA_yR\frac{\partial u}{\partial y} + wA_z\frac{\partial u}{\partial z}\right) - \xi\frac{A_x v^2}{xV_f} = -\frac{1}{\rho}\frac{\partial p}{\partial x} + G_x + f_x - b_x - \frac{R_{SOR}}{\rho V_f}(u - u_w - \delta u_s) \\ \frac{\partial v}{\partial t} + \frac{1}{V_f}\left(uA_x\frac{\partial v}{\partial x} + vA_yR\frac{\partial v}{\partial y} + wA_z\frac{\partial v}{\partial z}\right) - \xi\frac{A_y uv}{xV_f} = -\frac{1}{\rho}\left(R\frac{\partial p}{\partial y}\right) + G_y + f_y - b_y - \frac{R_{SOR}}{\rho V_f}(v - v_w - \delta v_s) \\ \frac{\partial w}{\partial t} + \frac{1}{V_f}\left(uA_x\frac{\partial w}{\partial x} + vA_yR\frac{\partial w}{\partial y} + wA_z\frac{\partial w}{\partial z}\right) = -\frac{1}{\rho}\frac{\partial p}{\partial z} + G_y + f_z - b_z - \frac{R_{SOR}}{\rho V_f}(w - w_w - \delta w_s)) \end{cases}$$

Eq(5.9)

where it can be observed that:

- in the right-hand part of the equation we have the more-general term considering the cylindrical framework (R and ξ);
- (G_x, G_y, G_y) are body acceleration while the term *f* describes the viscous term;
- (u_w, v_w, w_w) are the component of the velocity of the mass source while $(\delta u_s, \delta v_s, \delta w_s)$ are the fluid velocity stemming from the mass-source movement.

5.2 Mathematical modeling of a lymphangion

In this section we define the numerical model of the contractile element of the lymphatic system, called lymphangion. The proposed model is inspired by the work of Jamalian and Davis [7], which will be

presented in Section 5.1.1. In Section 5.1.2 we define the target of our investigation. Finally, in Section 5.1.3, we discuss the main hypotheses on which the model is based.

5.2.1 Description of reference article

In the work of Jamalian and Davis [7] in-vivo measurements of lymphatic activity have been performed. Specifically, they isolated a lymphatic vessel from rat mesentery containing six valves as depicted in Figure 5.1.

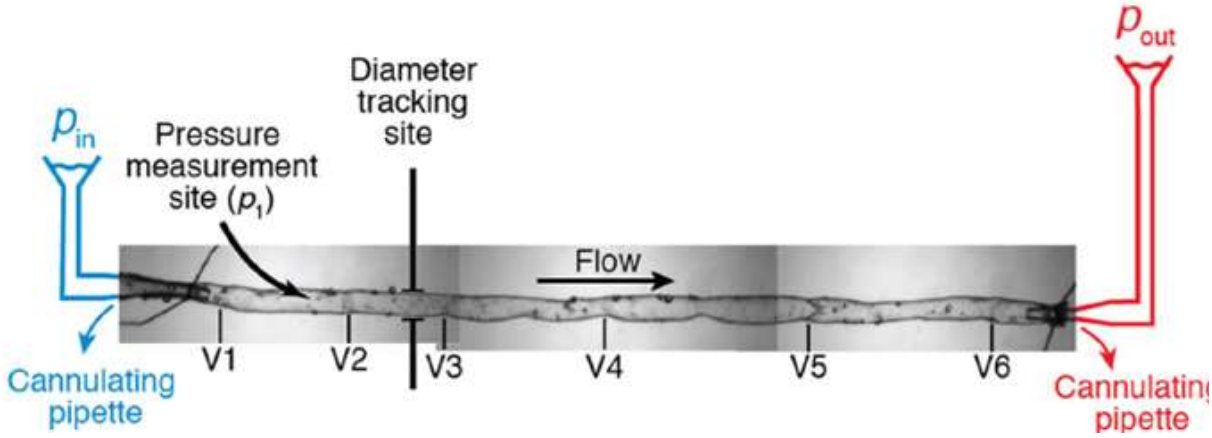

Figure 5.3: Experimental set-up of the lymphangion chain described in [7]

They cannulated this vessel to be able to impose a pressure boundary condition at the inlet and outlet with two reservoirs. With this set-up, they were able to observe a dynamic contractile function without the application of any external stimulus. Then, they recorded both pressure and diameters in the tracking site reported in Figure 5.1. Time rate of change of those experimental quantities is reported in Figure 5.2.

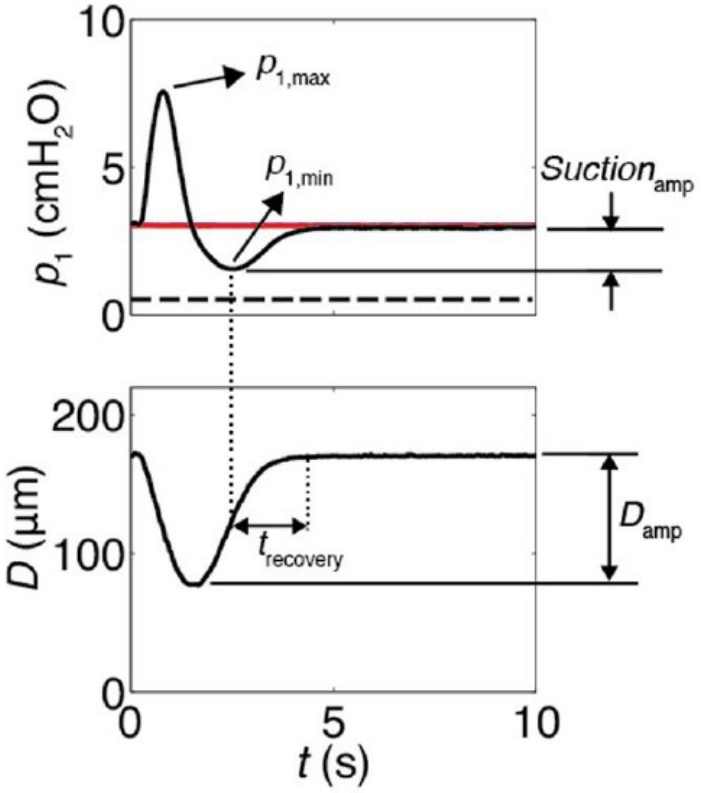

Figure 5.4: *pressure and diameter experimentally measured from [7]*

5.2.2 Definition of the model

Our goal is to develop a mathematical model capturing the main physiological characteristics of a lymphangion, which can serve as the framework to investigate the fluid dynamic behaviour of this element. To this purpose, we build a three-dimensional model of an *equivalent lymphangions* with ***FLOW-3D*** based on the experimental measurements provided in the work of Jamalian and Davis [7]. The concept of equivalent lymphangion is introduced to mathematically summarize the fluid-dynamic behaviour of the five vessels in a single element.

This element is characterized by same boundary conditions and geometrical features reported in [7]. Using the introduced equivalent lymphangion we calibrate the numerical model on the reproduction of the time rate of change of pressure reported in Figure 5.2.

5.2.3 Challenges and assumptions of the numerical model of a

lymphangion

The first step to study the fluid-dynamic behaviour of a lymphangion with a CFD approach is the definition of the simulation domain. Regarding the problem at hand, the computational domain must vary its shape to reproduce the cardiac-like contraction of this vessel.

To describe this peculiar feature, we introduce a first modeling hypothesis. Specifically, the displacement of the lymphangions wall is constrained to reproduce the time-diameter relationship observed by [7]. This hypothesis stems both from the target of our model and the uncertainty in the physiological literature regarding the mechanism triggering this contraction [4][11]. However, the characterization of the time rate of change of diameter is not enough to define a 3D domain because the geometry of a lymphangion cannot be considered cylindrical throughout all the contraction [8]. Hence, we will combine measurements reported in [7] and the available information in the literature to define a geometry representative of an average lymphangion.

If we analyse the lymphangion's shape at the end of the contraction, we can assume a cylindrical geometry. It will be characterized by the smallest diameter reported in [7] and a length of 1 mm [7] and it is depicted in Figure 5.3.

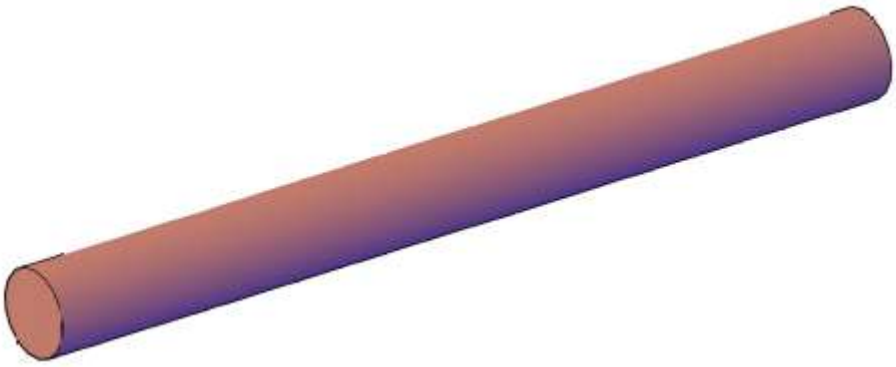

Figure 5. 5: geometry of the lymphangion at the end of contraction phase

From this condition, there is an enlargement of the vessel, called diastole. At the end of this phase, the lymphangion experiences the maximum diameter and the hypothesized geometry is reported in Figure 5.4.

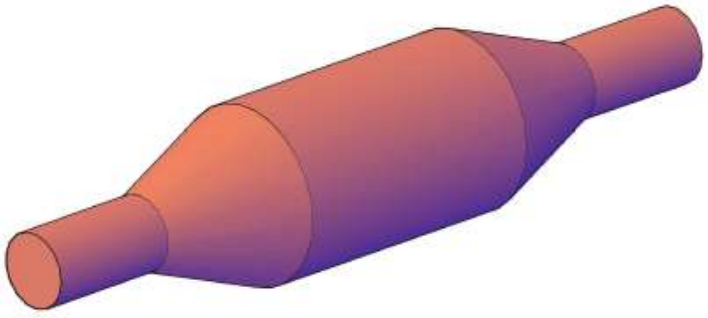

Figure 5. 6: *geometry of the lymphangion at the end of diastole phase*

The assumed volume is characterized by a central part whose diameter has been evaluated as the maximum observed in [7]. The two cones connect the cylinder defining the continuous wall of the lymphangion. Having considered the images reported in the literature [8], [11], [43], the geometry reported in Figure 5.4 is a reasonable approximation and it will constitute the domain within which the fluid will move.
To properly reproduce the physiology of the lymphangion, we must consider valves. These elements move according to pressure dynamics inside the chambers and prevent retrograde flow. In the reference article [7], there is no quantitative information regarding both dynamics of their movement and shape. Hence, we have performed a survey of existing available reference to define a consistent modeling of this element.
From confocal images reported in Figure 5.5, we can observe the thin shape of those elements.

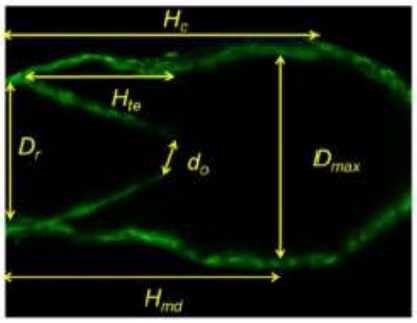

Figure 5.7: Confocal images of a lymphangion valve

Moreover, we can introduce a parameter which will play a crucial role in the valve modelling. Using the same terminology as in Figure 5.5, we can define the opening angle as

$$Opening\ angle = \frac{d_0}{D_r} \qquad \text{Eq (5.10)}$$

This quantity defines the space within which fluid will move when valves are open.
Considering Figure 5.6 (from [8]), we can further notice how the valves movement ranges from a completely closed state to an open situation where an almost horizontal configuration is reached (in the plane orthogonal to movements).

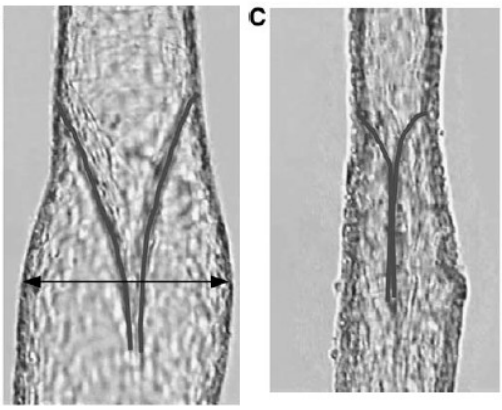

Figure 5. 8: valves at the end of systole and in a closed state

Hence, we will assume valve movement to be characterized by two configurations. Initially, the valve is closed and $d_0 = 0$. When movement of this object is triggered by forces exerted by the fluid, the valve will move from a closed state to a final configuration, where $\frac{d_0}{D_r} = max$.

The maximum opening angle of valves will be a parameter calibration of this simulation and it will be analysed in section 5.3. Regarding the valve shape, we introduce parallelepipedal objects. Rigorously, its shape should be characterized as a leaflet. However, given their thin dimension we considered this assumption reasonable.

5.3 Definition of the numerical modelling with FLOW-3D

In this section we will describe the construction of the numerical model in ***FLOW-3D*** according to the assumptions listed and motivated in section 5.1. In Section 5.3.1 we describe the model called general moving objects (GMO), which allows objects move in the simulation. Then we present the geometrical set-up of the model. In section 5.3.3 we will determine both the maximum opening angle of the valve and the mesh configuration which will determine the final configuration of our model of the lymphangion.

5.3.1 GMO model

General moving object (GMO) is the model with which objects can move in ***FLOW-3D***. The motion of these object can be entirely prescribed or coupled. A coupled scheme of GMO means that ***FLOW-3D*** solves the equations stemming from the fluid-structure interaction to compute forces which make the object move. In contrast, when we consider a prescribed method, objects move according to an imposed movement and they are not affected by fluid motion. ***FLOW-3D*** uses FAVOR™ algorithms to account for the presence of moving objects and its effect on fluid flow. Specifically, the peculiarity of FAVOR™ is that the mesh is maintained fixed and objects will occupy a different part of the computational domain according to their movement. As a result, we will observe a change in the area and volume fraction of cells which will affect the flow regime in the area surrounding moving objects. To describe the change of the area and volume fraction of a cell, sources and sink terms are introduced in both mass and momentum balance. For instance, the general form of mass-balance equation reads as

$$\frac{\partial}{\partial t}(\rho \cdot \underline{V_f}) + \nabla \cdot (\rho \underline{u} A) = S_m \qquad \text{Eq (5.11)}$$

If a moving object is present, Vf and A vary with time and, Eq (5.1) becomes

$$\frac{\underline{V_f}}{\rho}\frac{\partial \rho}{\partial t} + \frac{1}{\rho}\nabla \cdot (\rho \underline{u} A) = \frac{S_m}{\rho} - \frac{\partial \underline{V_f}}{\partial t} \qquad \text{Eq (5.12)}$$

Comparing it with the continuity equation for stationary obstacle problems Eq(5.3), it can be seen that $\frac{\partial V_f}{\partial t}$ is equivalent to an additional volume source term. When using the control volume method, this source term exists only in mesh cell around the moving object boundary and the source term is computed as

$$\frac{\partial V_f}{\partial t} = \frac{S_{obj}}{V_{cell}} V_{obj} \cdot \underline{n} \qquad \text{Eq (5.13)}$$

where:

- Vcell is volume of a mesh cell;
- Sobj, n and Vobj are surface area, unit normal vector and velocity of the moving object in the mesh cell respectively.

Let us consider the momentum balance equation

$$\begin{cases} \frac{\partial u}{\partial t} + \frac{1}{V_f}\left(uA_x\frac{\partial u}{\partial x} + vA_yR\frac{\partial u}{\partial y} + wA_z\frac{\partial u}{\partial z}\right) - \xi\frac{A_x v^2}{xV_f} = -\frac{1}{\rho}\frac{\partial p}{\partial x} + G_x + f_x - b_x - \frac{R_{SOR}}{\rho V_f}(u - u_w - \delta u_s) \\ \frac{\partial v}{\partial t} + \frac{1}{V_f}\left(uA_x\frac{\partial v}{\partial x} + vA_yR\frac{\partial v}{\partial y} + wA_z\frac{\partial v}{\partial z}\right) - \xi\frac{A_y uv}{xV_f} = -\frac{1}{\rho}\left(R\frac{\partial p}{\partial y}\right) + G_y + f_y - b_y - \frac{R_{SOR}}{\rho V_f}(v - v_w - \delta v_s) \\ \frac{\partial w}{\partial t} + \frac{1}{V_f}\left(uA_x\frac{\partial w}{\partial x} + vA_yR\frac{\partial w}{\partial y} + wA_z\frac{\partial w}{\partial z}\right) = -\frac{1}{\rho}\frac{\partial p}{\partial z} + G_y + f_z - b_z - \frac{R_{SOR}}{\rho V_f}(w - w_w - \delta w_s)) \end{cases}$$

Eq(5.14)

In those equations, the term Uw = (u_w, v_w, w_w) is the velocity of the source component, which will generally be non-zero for a mass source in the GMO while $(\delta u_s, \delta v_s, \delta w_s)$ the velocity of fluid respect to the mass source

5.3.2 Numerical model of the lumped lymphangion with FLOW-3D

Geometrical features of physical objects are defined in ***FLOW-3D*** through components and subcomponents. Specifically, components represent physical objects and are the portion of a given body that will share common properties and the initial condition. Subcomponents represent the geometrical shape of solid objects or holes within a given component. By a computational standpoint, components may be further subdivided into non-moving and moving objects. The former represents the fixed boundary of the domain whereas the latter moves according to the force the fluid exerts on them or through movement prescribed by the user.

To characterize the assumed geometry of the lymphangion with ***FLOW-3D***, we introduced a cylindrical component and three moving objects. These components define the continuous boundary of the lymphangions. The computational domain in the initial condition(t=0) is depicted in Figure 5.9.

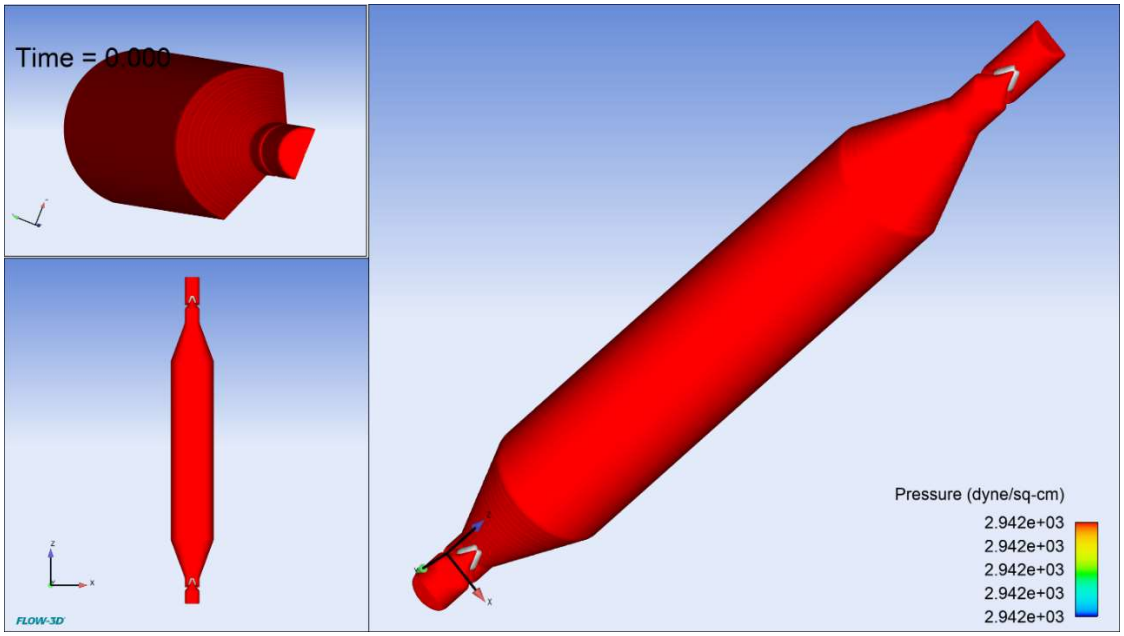

Figure 5.9: Rendering in FLOW-3D of the lymphangion geometry in the initial condition

Then, we must describe the movement of these objects in the contraction and relaxation phase. In agreement with the hypotheses described in section 5.2.3, their motion will be imposed a priori to reproduce the time rate of change of diameter reported in [7]. Thus, we will use the prescribed scheme of GMO model of ***FLOW-3D***. By doing that, we must specify the angular velocity of the moving objects. Specifically, the cylinder will move along the x- axis (the reference system is reported below in Figure 5.10) with a translational velocity defined by time diameter behaviour measured in [7]. The cones will rotate along the y-axis following the movement of the cylinder.

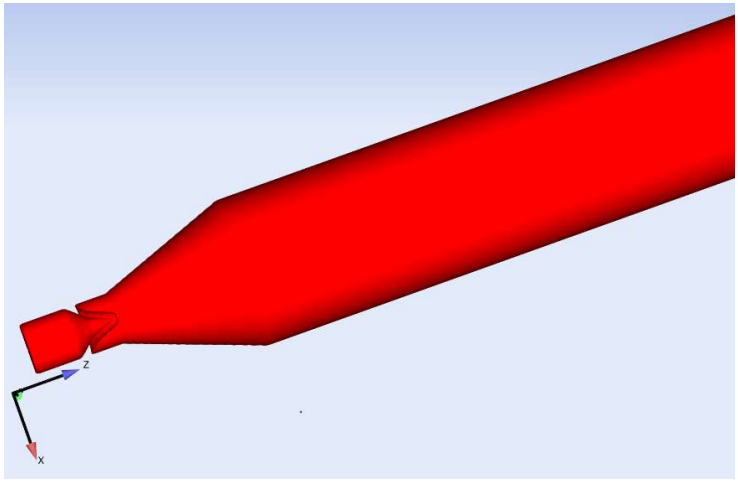

Figure 5.10:Reference System

Before computing these quantities, we want to verify if we can optimize the simulation. Specifically, in agreement with physiological literature [11], [23] we can expect a laminar flow in the lymphangions. If this condition is verified, we can introduce the assumption of axial-symmetry with a significant reduction of the computational effort. To verify this hypothesis in our model, we evaluate the flow regime.

Having imposed the geometry and movement of lymphangions, we know the volume displaced in the contraction phase. Hence, we can compute the expected discharge according to mass conservation.
Thus, we can evaluate the Reynolds number. This dimensionless number describes characteristics of flow regime and, if lower than a threshold value, can be considered representative of a laminar condition.
To compute discharge, a Matlab code is implemented. Initially, time-diameter curve from [7] is digitalized. The length of the lymphangion (1 mm from [7]) is discretized into n_L element as well as the observation time of a single contraction cycle, 10 seconds, subdivided into N temporal instants. Owing to contraction, at each time step volume contributions depend on the radius α of the lymphangion, defined as

$$\alpha = arctan\left(\frac{radius(i)}{(L - L\_centro/2)}\right) \qquad \text{Eq (5.15)}$$

Where L_centro is depicted in Figure 5.10 and it is assumed equal to 0.7 mm

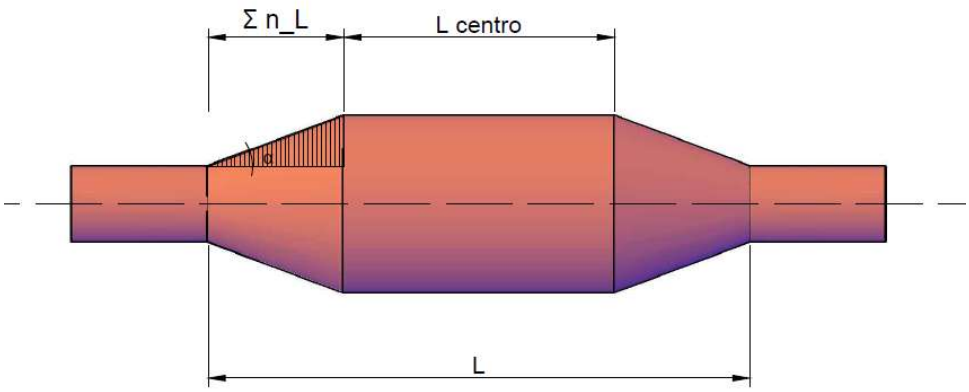

Figure 5.11:Discretization of the numerical domain to compute discharge

The volume inside the lymphangion is determined by two contributions:

- volume given by the two lateral cones;
- contribution given by the central cylinder

At each time step, we can compute the contribution of each n_L infinitesimal volume and then add the values along longitudinal direction to obtain the volume. We can repeat this procedure throughout the duration of the contractile cycle (10 s) determining the time behaviour of the discharge.
More precisely, the implemented algorithm is reported in Table 5.1.

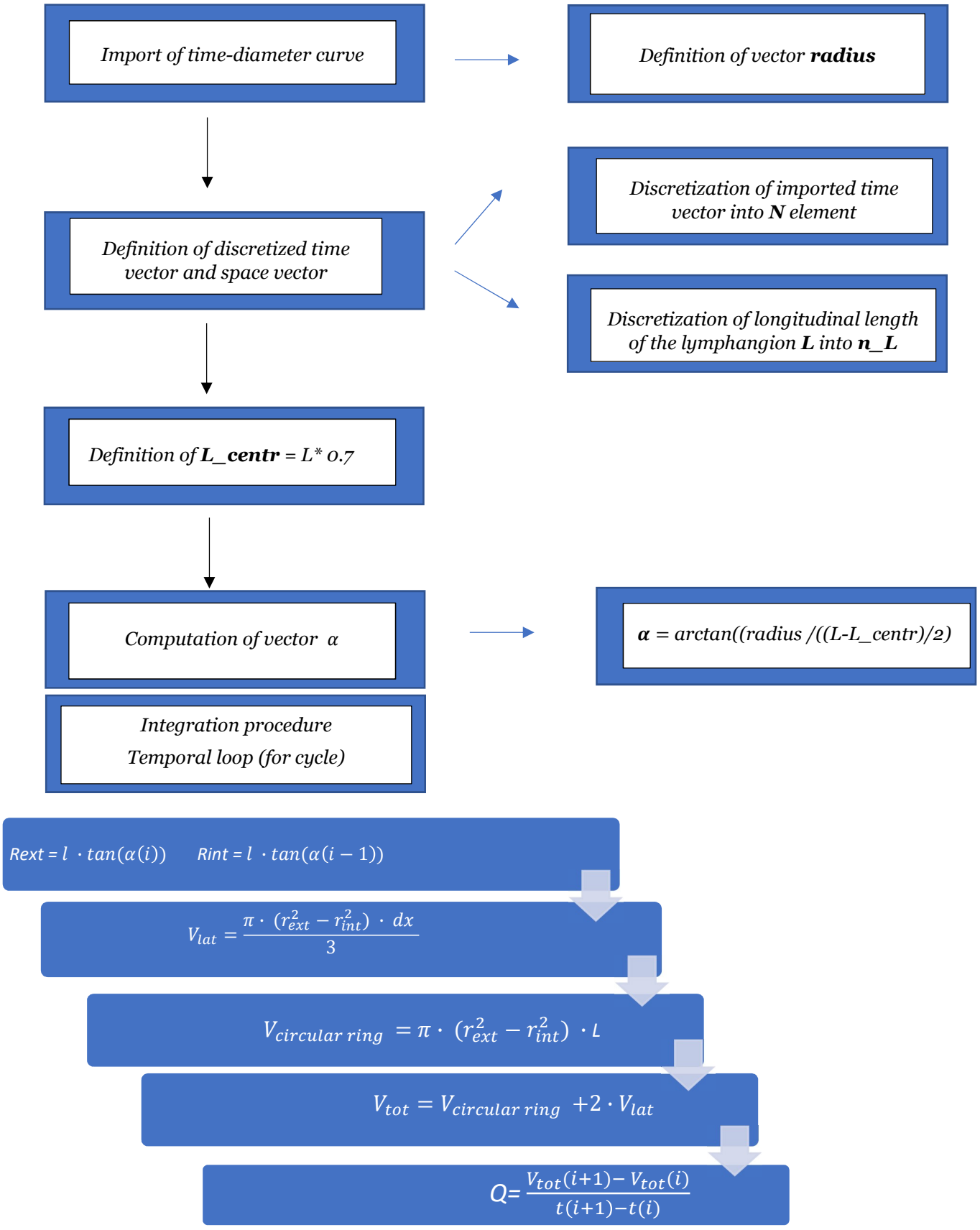

Table 5.1: Matlab code to compute discharge

The resulting time-discharge plot is reported below

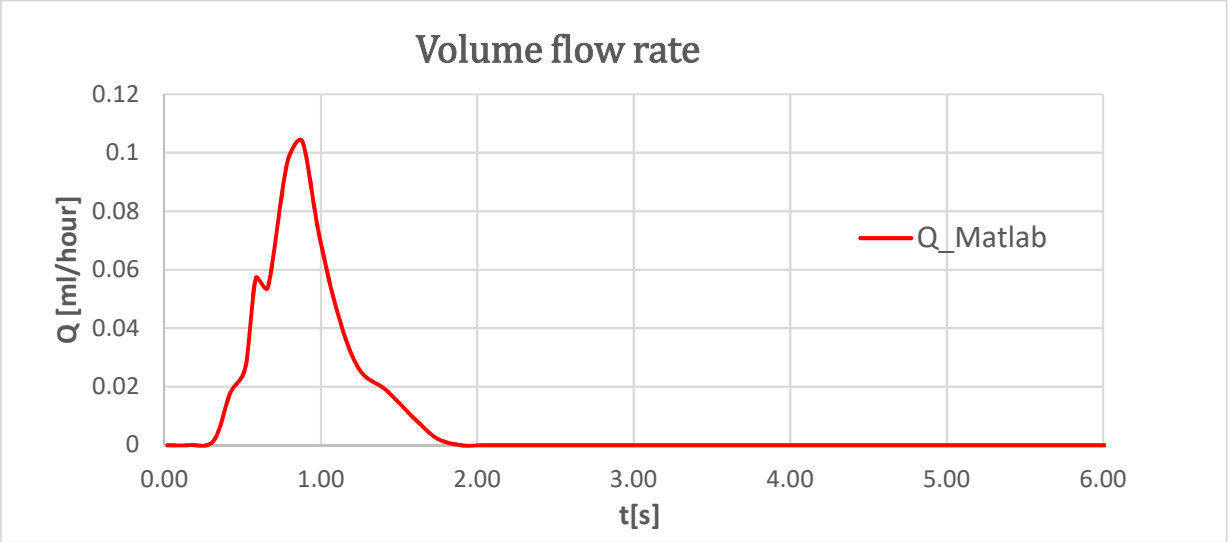

Figure 5.12:Time rate of change of discharge computed with Matlab

To compute the Reynolds number, we need velocity, a characteristic length and property of the fluid. Even if in the reality lymph is a mixture of lipid, protein and water, it can be considered (as already done in [44]) as a single phase-flow characterized by the same hydraulic properties as water.
Average velocity is computed starting from discharge reported in Figure 5.12 dividing by the cross-sectional area. Specifically, we pursue the preliminary evaluation of the Reynolds number in valve cross section where we expect the fluid to accelerate. Here, we assess the radius as one third of the diameter of the cylinder because its exact value depends in the opening angle which will be calibrated in section 5.3.5.
Considering as a characteristic length the diameter of the lymphangion, the quantities involved in the computation are reported in Table 3.2

ρ	1000	kg/m3
μ	0.01	kg/m/s
D	0.1	cm
V	0.7	cm/s

Table 5.2: evaluation of Reynolds number

leading to a value of Reynolds number equal to:

$$Re = \frac{\rho \cdot V \cdot D}{\mu} = 1.96 \qquad \text{Eq(5.16)}$$

The obtained value of Reynolds is representative of a laminar condition. Consequently, we introduce the assumption of axial-symmetry to study our 3D problem into a 2D domain. Hence, from now on, we will refer to the 2D section reported in Figure 5.13 for the calculation.

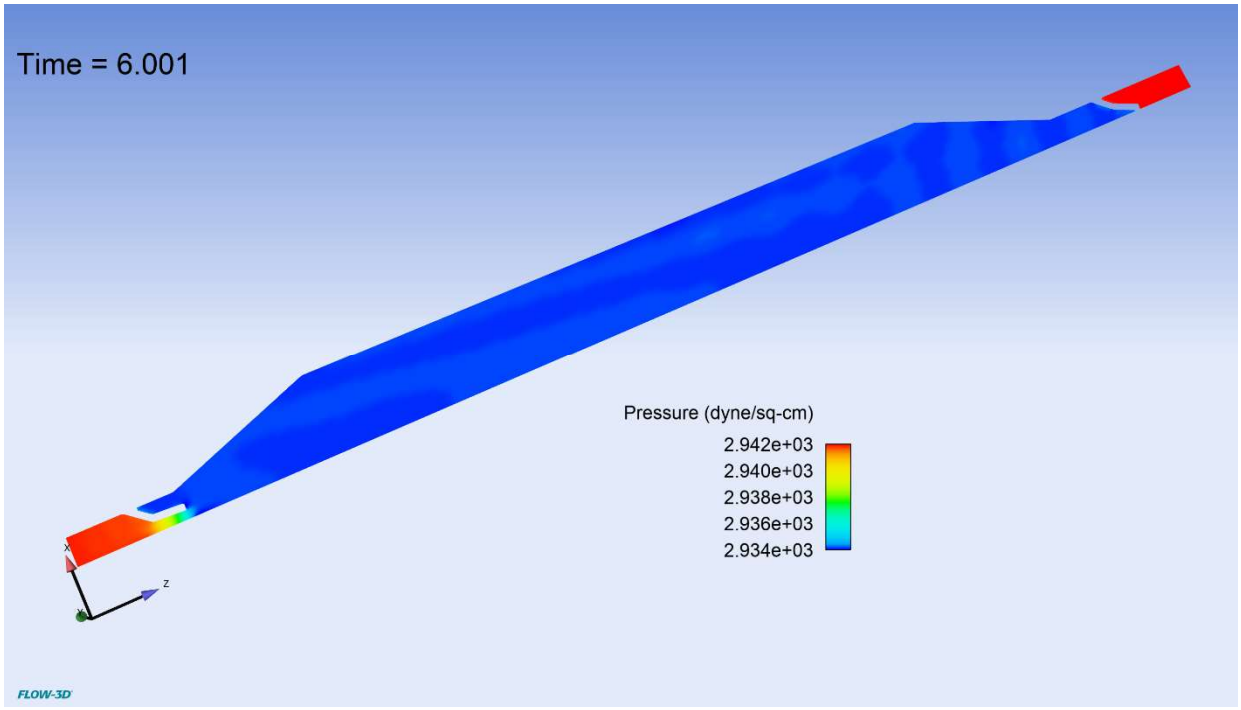

Figure 5.13:Rendering of a lymphangion exploiting the assumption of axial-symmetry

The same Matlab code is used to obtain the angular velocity of the cones, which represents the input needed in ***FLOW-3D*** to make these objects move, namely

$$\boldsymbol{vel\_angular} = \frac{\alpha(i+1) - \alpha(i)}{t(i+1) - t(i)} \qquad \text{Eq(5.17)}$$

It is worth noting that the two cones will move with an equal but opposite angular velocity.
The central cylinder will be characterized by the following translational velocity

$$\boldsymbol{vel\_translational} = \frac{radius(i+1) - radius(i)}{t(i+1) - t(i)} \qquad \text{Eq(5.18)}$$

Knowing these velocity, we can prescribe the motion of the moving objects constituting the lymphangions wall in ***FLOW-3D***. In Figure 5.13, we compare the time rate of change of diameter observed experimentally in [] with the one obtained in our simulation with the previous reasoning.

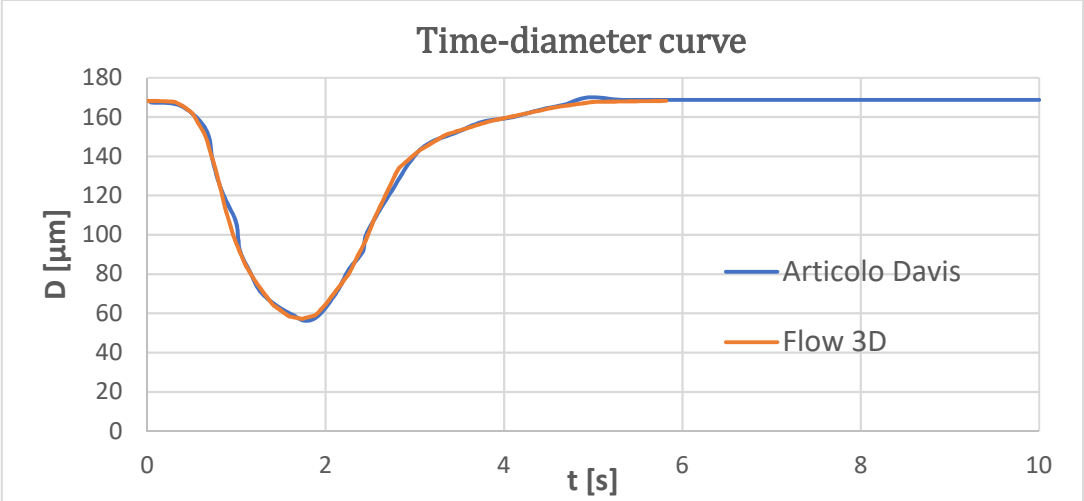

Figure 5.14: comparison between experimental and numerical time-diameter curve

As one can see, there is a consistent agreement between the movement we impose and the one recorded experimentally.

5.3.3 Valve modeling

Valve geometry is inspired by Figure 5.7. Specifically, we consider two rectangular components to create their numerical counterpart with ***FLOW-3D***.
Exploiting axial-symmetry, we introduce a rectangular non-moving object, representing a part of valves which is hypothesized not be influenced by the motion of fluid. Then, we consider a second rectangular moving object represented by the black component in Figure 5.15.

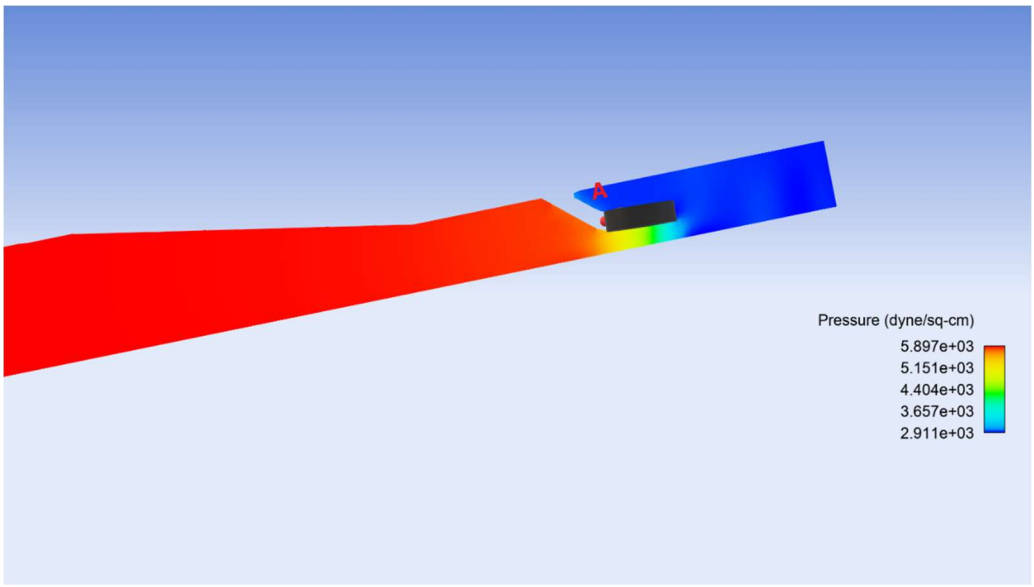

Figure 5. 15: Moving flange of valve

This object will rotate along the y-axis (the reference system is the one reported in Figure 5.10) to determine the opening angle of valve (Eq 5.11). Specifically, we adopt a coupled scheme of the GMO model of ***FLOW-3D*** for this component. Hence, from the initial configuration it will rotate according to the forces exerted on them by the fluid.
In agreement with Section 5.1.3, we assume that valves have a maximum rotation angle corresponding to a condition where valves are almost horizontal. The latter assumption represents the constraint that a valve cannot rotate by an infinite angle. It is worth noting that the continuity of the 2 components describing valve geometry is obtained interpenetrating them. By doing that, we are not introducing errors in the simulation because ***FLOW-3D*** will simply sum up area and volume fraction. Both inlet and outlet valve will be characterized with this geometry.

5.3.4 Numerical parameters of the simulation

The fluid considered in the simulation is water and its characteristics are defined in Table 5.2.
To run the simulation, we activate the model of GMO, where a coupled scheme is used for the valves and a prescribed one for the moving walls of the lymphangion, and the mode of the viscosity. We define the boundary condition as in [7], so an equal pressure of 294.2 Pa at both the inlet and at the outlet. On the remaining boundary a symmetry condition is introduced. In terms of numerical algorithm, in this simulation we considered a GMRES pressure solver and an implicit solver for the viscous stress.

5.3.5 Mesh assessment

The computational mesh discretizes the physical space of the simulation. Since physical variables vary continuously in space, a mesh with a fine spacing between nodes provides a better representation of the reality than a coarser one. However, reducing grid spacing leads to an increase of the size of the model. Hence, reaching a compromise between computational time and an accurate solution is one of the objectives of a numerical simulation.
Regarding our problem, mesh design is particularly important close to valves, where we have the reduction of the cross section. In this area, we need enough cells between valve and the symmetry plane to describe properly fluid dynamic behaviour. However, the magnitude of this cross-section reduction will depend on the maximum opening angle (Eq 5.1), which is a calibration parameter.
Hence, we have to analyse the effect of both maximum opening angle and mesh design on the simulation's results. Specifically, we must calibrate the parameter of the opening angle of valves which provides a similar behavior of pressure compared to the one observed experimentally. Meanwhile, we must define a mesh configuration characterized by a compromise between computational time and accuracy of the solution.
Initially we run the simulation with single mesh block to avoid the presence of inter-block boundary condition. Specifically, a uniform grid characterized by a quadratic cell of 2.5 e-4 is considered and is reported in Figure 5.16.

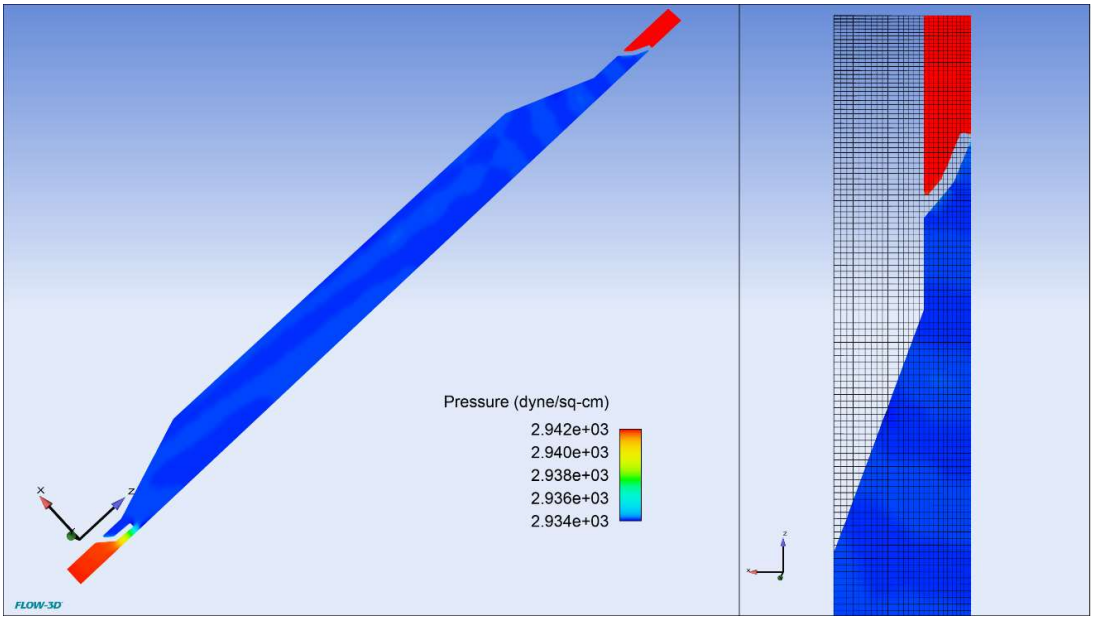

Figure 5.16: Uniform mesh with cell dimension 2.5 e-4

With this mesh, after several attempts, a maximum opening angle of 18.5 degrees is chosen. This angle provides a pressure gradient inside the lymphangion resembling the one observed experimentally in [7], as reported in Figure 5.17.

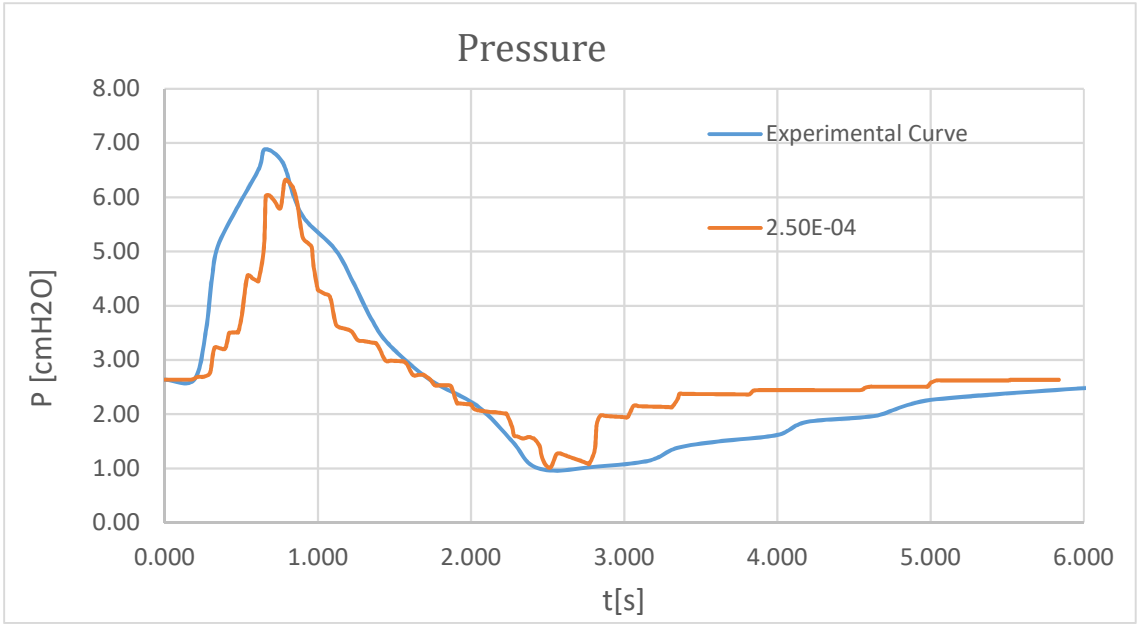

Figure 5.17: Time rate of change of pressure with an opening angle of 18.5°

The volume flow rate superimposes the one computed with Matlab (based on mass conservation) as can be seen in Figure 5.18.

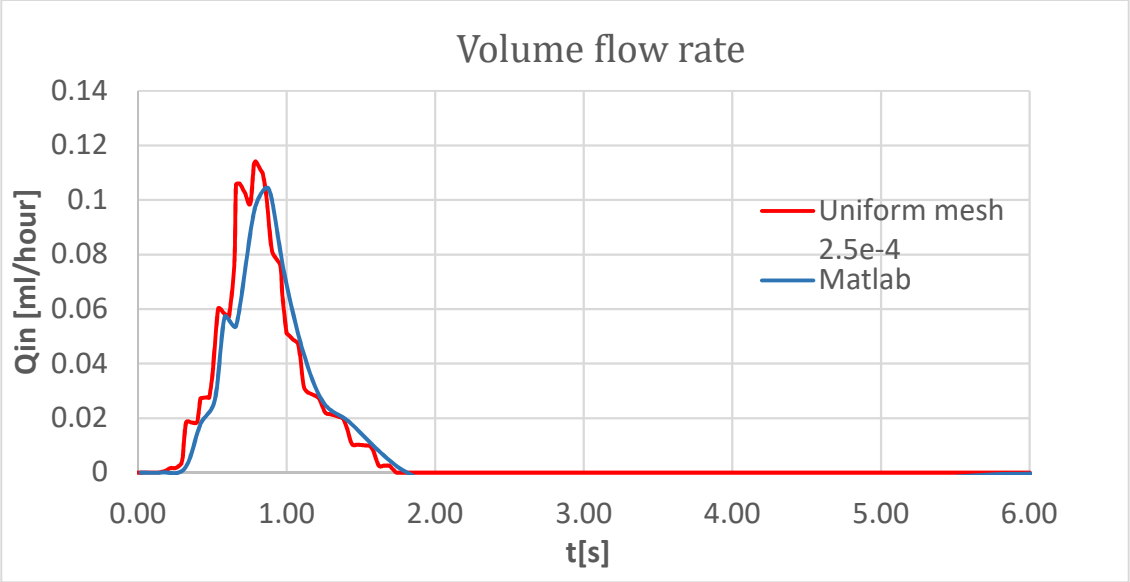

Figure 5.18: Outlet volume flow rate

Regarding pressure, the average gradient experienced by the lymphangion during contraction and relaxation is similar, even if there are some differences regarding the shape of the pressure curve. This difference in the pressure curve is reasonable since we are describing an equivalent model of the experimental set-up described by Davis. Hence, we consider it as a preliminary acceptable solution.
We also address the issue of the dependence of the solution on the mesh. Depending on the number of cells into valve cross-section reduction, we expect to describe more precisely the pressure dynamic.
We report below only three cases, where we reduced the cell size from 2.5 e-4 to 1e-4.

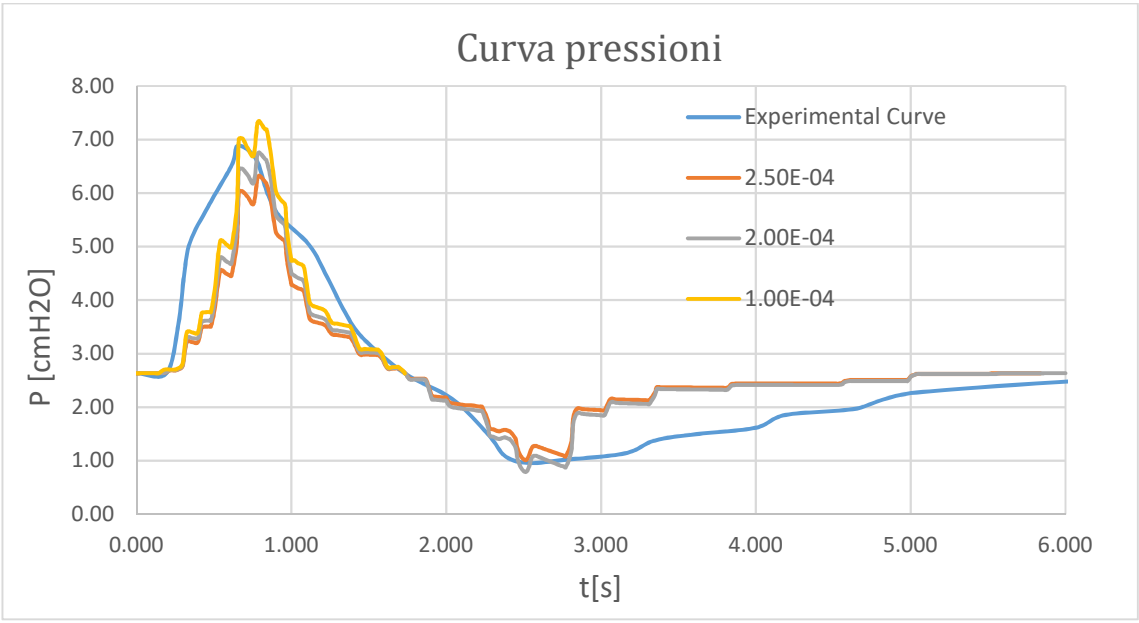

Figure 5.19: Time-rate of change of pressure with different mesh configuration

We decide to consider a uniform mesh with a cell dimension of 2e-4. This solution allows us to refine the mesh maintaining an affordable computational effort.We show below a magnification of the area of the valve both in the initial configuration in Figure 5.16 and when the outflow valve is completely open, depicted in Figure 5.17.

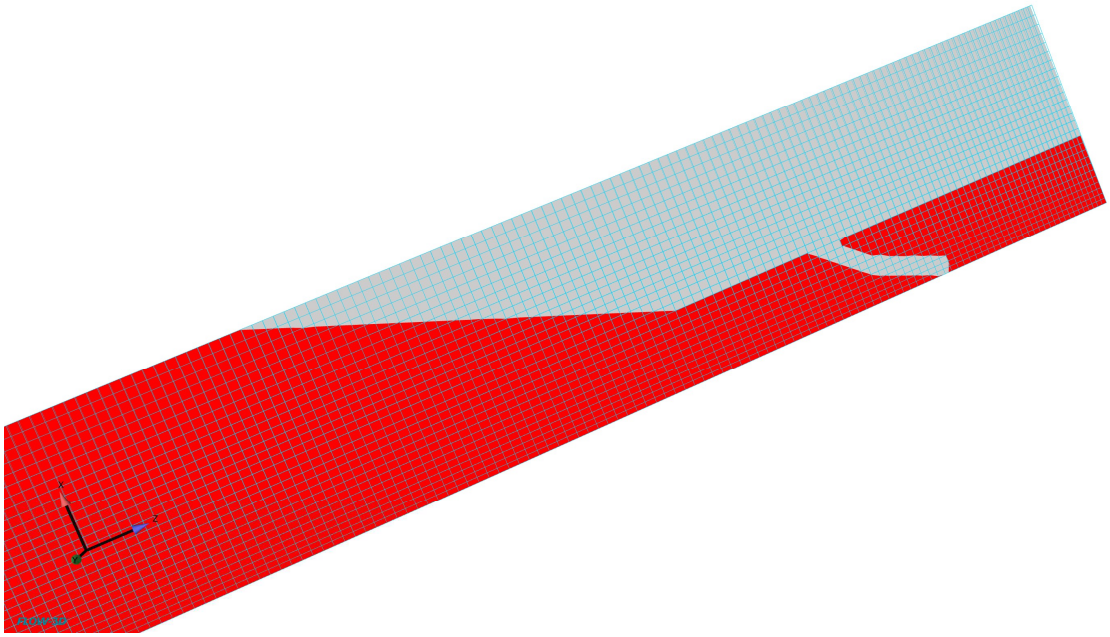

Figure 5.20: Outlet valve in the closed configuration

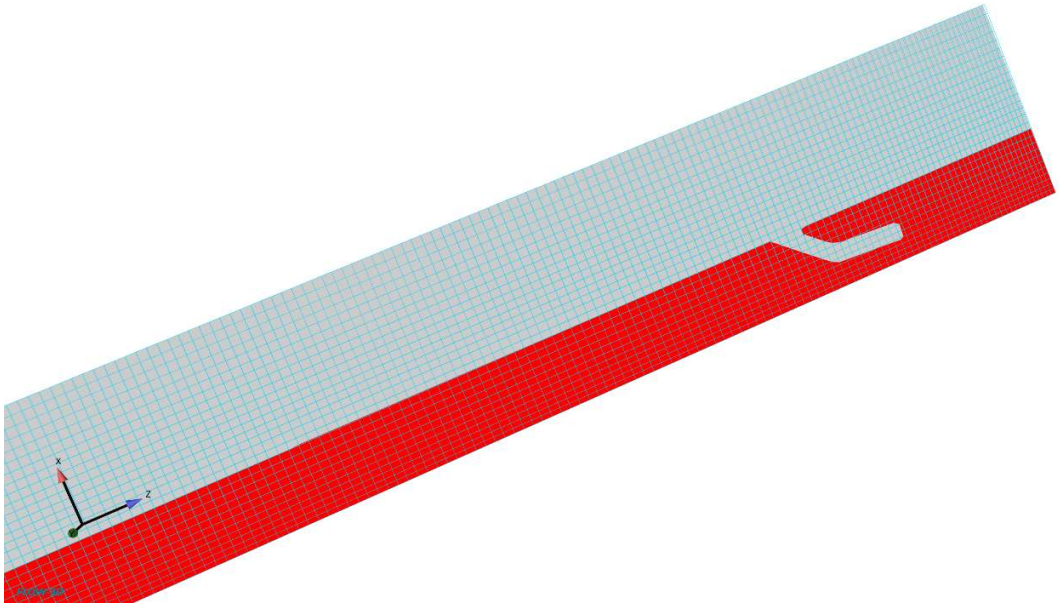

Figure 5.21:Outlet valve in the open configuration

5.4 Simulation results from the 3D modelling of an equivalent lymphangion

In this section we present the results of the single equivalent lymphangion model. In section 5.4.1 we interpret pressure behaviour based on fluid dynamic theory while in section 5.4.2 we analyse valve movement. Then, based on these observations, we will modify the simulation set-up to reduce the computational time.

5.4.1 Description of pressure behavior

Pressure behaviour is influenced by the movement of the lymphangion wall, the presence of valves and the boundary conditions. These three elements lead to the time-rate of change observed in Figure 5.18. We can analyse pressure behaviour subdividing simulation time (6s) in different time frames (called stages).

Stage 1, initial condition: fluid is initialized at the pressure of the boundary and valves are closed.

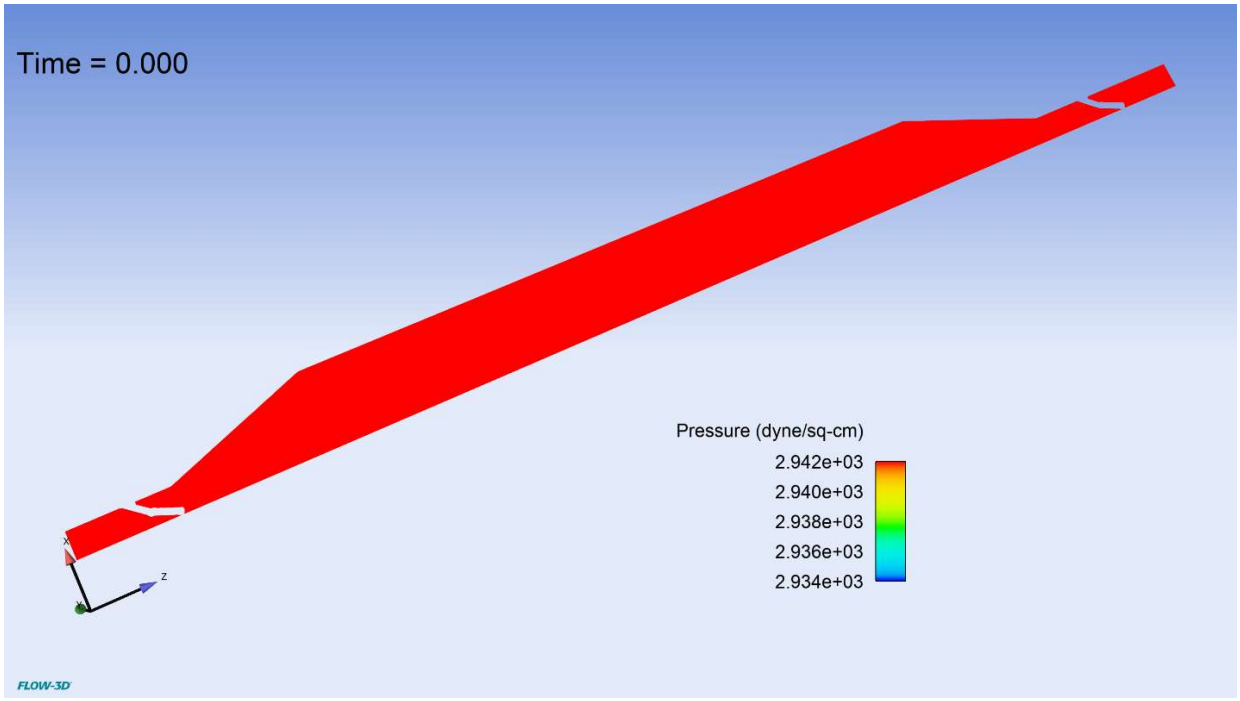

Figure 5.22: pressure inside the lymphangion in the initial condition (t=0)

Stage 2, contraction.

When the lymphangion starts moving, walls exert a pressure and displace a certain volume of fluid.

This movement leads to an increase of pressure inside the lymphangion and cause the outlet valve to open. Once this valve has opened, the movement of the wall provides the driving force to move fluid towards the outlet section. In the region of valves, the fluid accelerates locally due to cross-section reduction. In

agreement with mass conservation, this local increase of velocity requires an increase of pressure inside the lymphangion exactly equal to the pressure drop caused by the valve, which can be expressed as

$$\Delta P = \alpha Q^2 \qquad \text{Eq(5.19)}$$

The coefficient α depends on shape and dimension of the cross-section reduction and it demonstrates a-posteriori the influence of the opening-angle on fluid dynamic behaviour inside the lymphangion.
We report below a snapshot of a temporal instant of this contraction phase

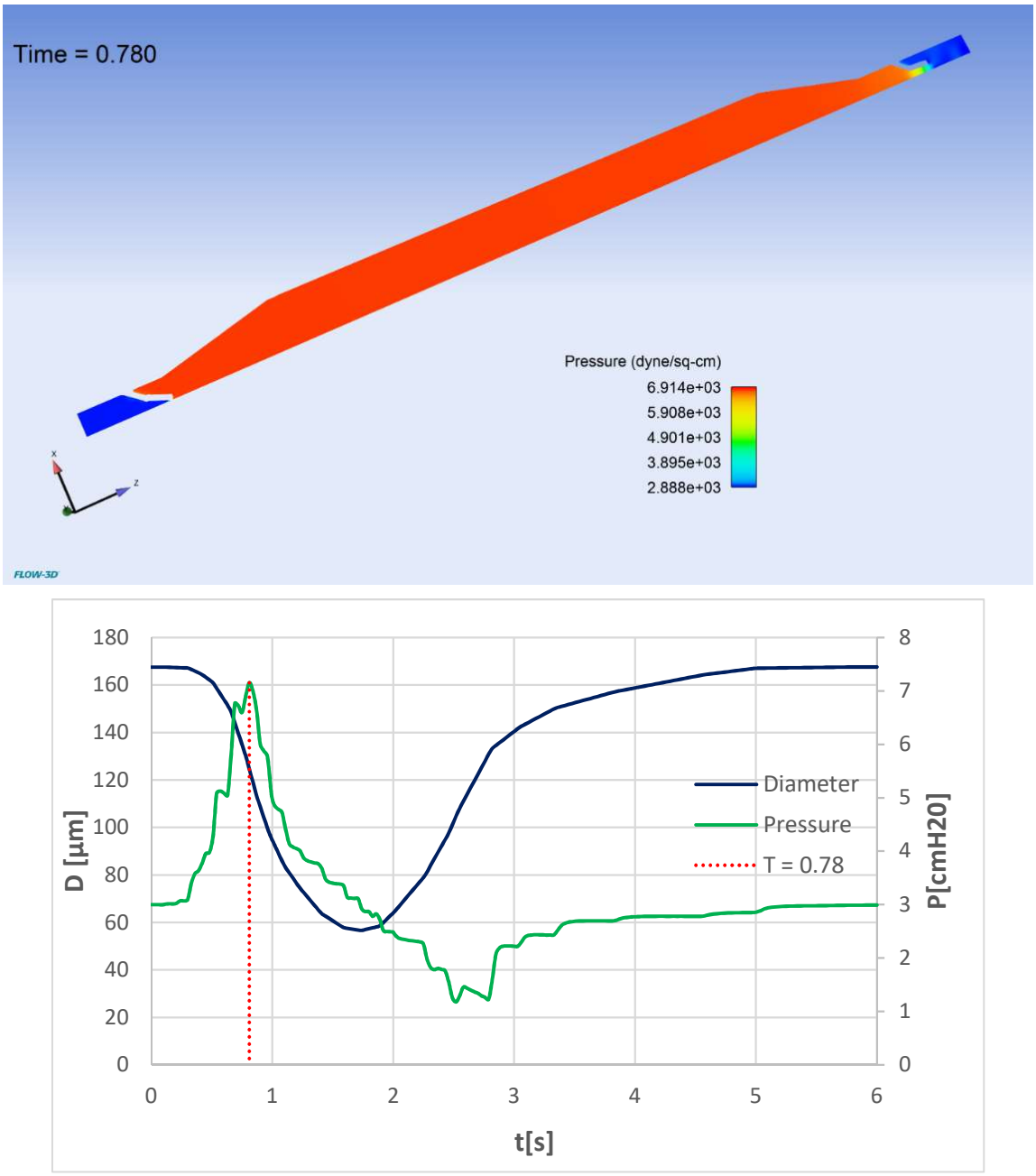

Figure 5.23: contraction phase

The graph above represents the time rate of change of pressure inside the lymphangion. Specifically, the red line illustrates the instant corresponding to the maximum pressure. This moment corresponds to the maximum velocity of the lymphangion, which can be detected by an inflection in the time-diameter curve.
We can make another interesting remark regarding the pressure dynamic. In Figure 5.23 we plot the time-rate of change of pressure inside a lymphangion in three different locations of the chambers (at the inlet, center and outlet section of the lymphangion). We can evaluate this quantity in ***FLOW-3D*** with probes, which are measurement points introduced a priori in the simulation to control the fluid-dynamic behaviour.

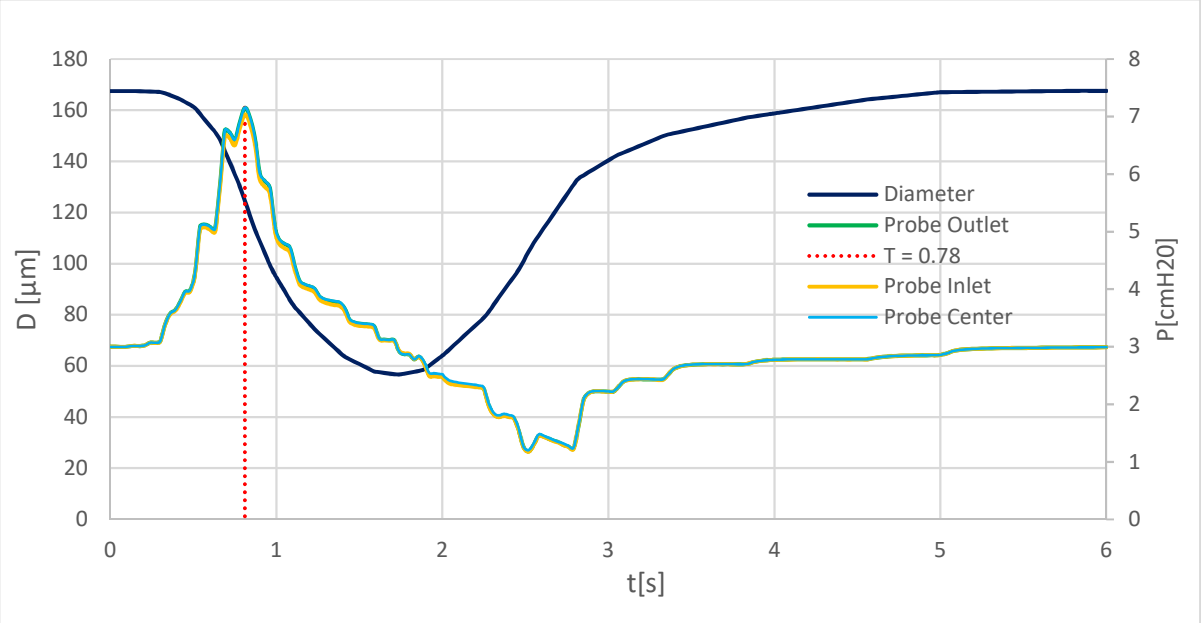

Figure 5.24:Pressure comparison in different location inside the lymphangion

As can be noticed, we have small differences of pressure along the longitudinal direction. This observation shows how the interior of the lymphangion has an almost uniform pressure distribution in space.
Hence, we can conclude that the observed time-rate of change of pressure stems almost entirely from the pressure drop caused by the valves. Rigorously, small pressure gradients are always present, but they are negligible compared to valve contribution. The only moment when these two terms are comparable is at the end of the contraction, corresponding to the minimum diameter. However, in all the other instants of the simulation the pressure drop caused by valves play the major role and determine the observed time rate of change of pressure.

Stage 3, minimum diameter
In this moment, walls of the lymphangion are no longer able to compress the fluid. They do not create the driving force for movement and we do not observe an outflow. Consequently, the pressure drop caused by valves tends to zero and a pressure equal to the initial condition is re-established inside the lymphangion, as showed in Figure 5.24. This remark agrees with the previous observation that time-rate of change of pressure stems almost entirely from the valves. Corresponding to the minimum diameter, we can observe a small spatial pressure gradient inside our domain, as reported in the snapshot in Figure 5.24.

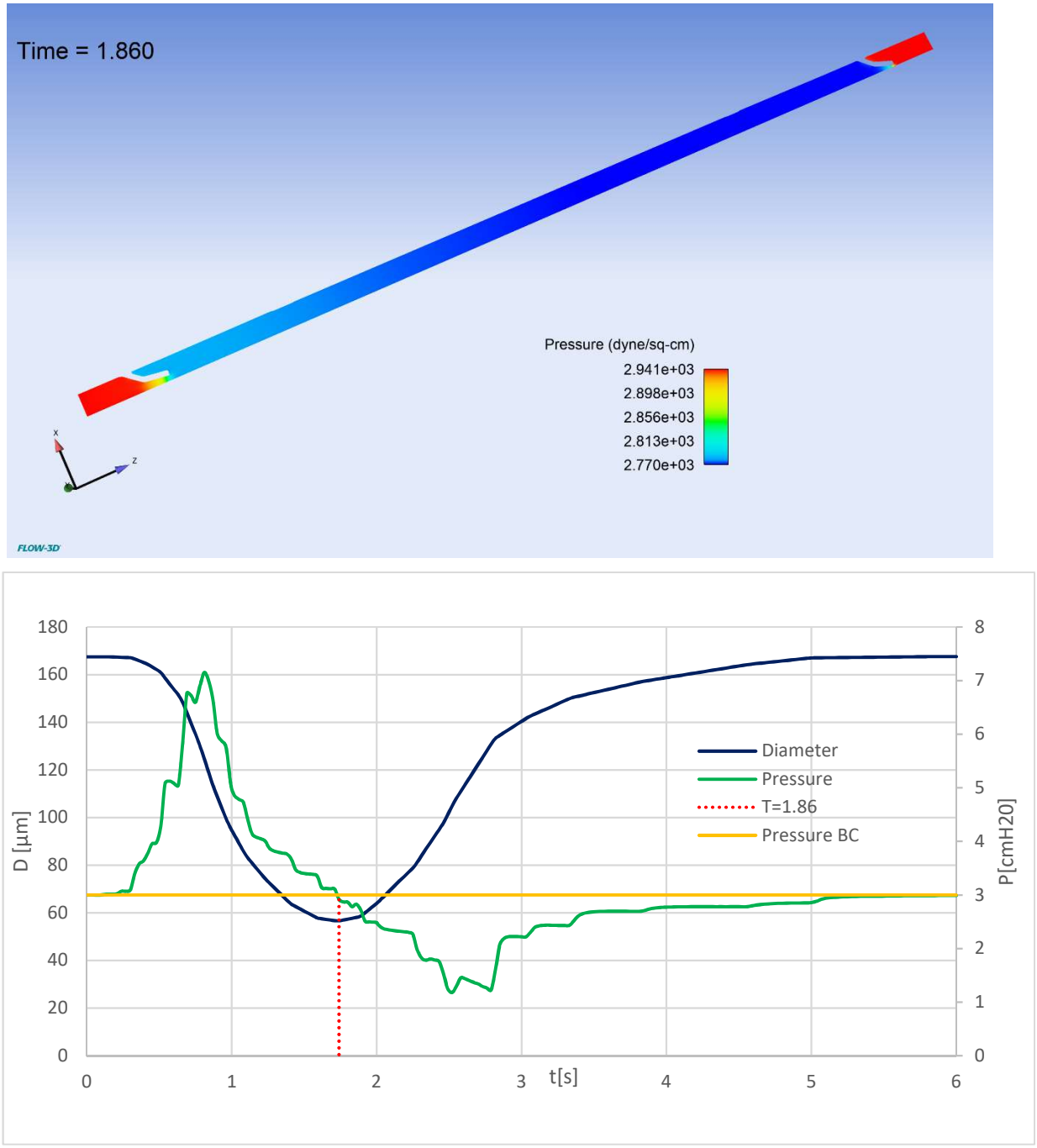

Figure 5.25: End-systolic phase

After this moment we have the next diastolic relaxation which will lead to a new time-rate of change of pressure inside the lymphangion.

Stage 4, Diastolic relaxation

When the expansion of the lymphangion takes place, pressure inside the lymphangion decreases.

The lymphangion adapts to this new condition triggering valves movements. The outflow valve closes preventing suction from the downstream boundary where a higher pressure is imposed, whereas the inlet valve opens. Since we have an inflow, we will have a new pressure drop caused by the inlet valve.
This will lead to a negative time-rate of change of pressure inside the chamber compared to the inlet boundary condition.
This is significant, because it demonstrates the capability of the developed numerical model to reproduce the pressure dip measured experimentally in [Davis], which is the evidence demonstration of the suction effect on the lymph formation.

5.4.2 Valve's movements

Another observation can be made related to valves dynamics. Having considered the GMO coupled physics, valves movement depends exclusively on pressure dynamic and forces exerted by the fluid. Consequentially, during the simulation they move according to the condition:

- If $Pup > Pdown$, valves are open;
- If $Pup < Pdown$, valves are closed;

where Pup is the pressure upstream of the valve (for instance in the inlet valve it is the inlet pressure boundary condition) while $Pdown$ is the one downstream of the valve (for the inlet valve the pressure inside the chambers).
Moreover, due to pressure dynamic previously described, we can conclude that the valves movement will happen exactly in the moment corresponding to end of systole independently of the pressure value at the boundary and the opening angle of the valve. In this moment, as previously explained, the lymphangion is not able to compress the fluid and the pressure boundary condition is re-established inside the lymphangions. Then, the subsequent diastole leads lead to a new pressure variation and triggers the synchronous movement of the valves. Specifically, the inflow valve opens while the outflow valve closes.
This observation emphasizes how the valve's dynamic is passive and completely depends on pressure behaviour and, in turn, on the diameter movement.
Moreover, in Figure 5.25, we can observe that the valve movement is fast and happens in a time interval which can be considered a small fraction of the perturbation which causes this movement (the variation of the diameter).

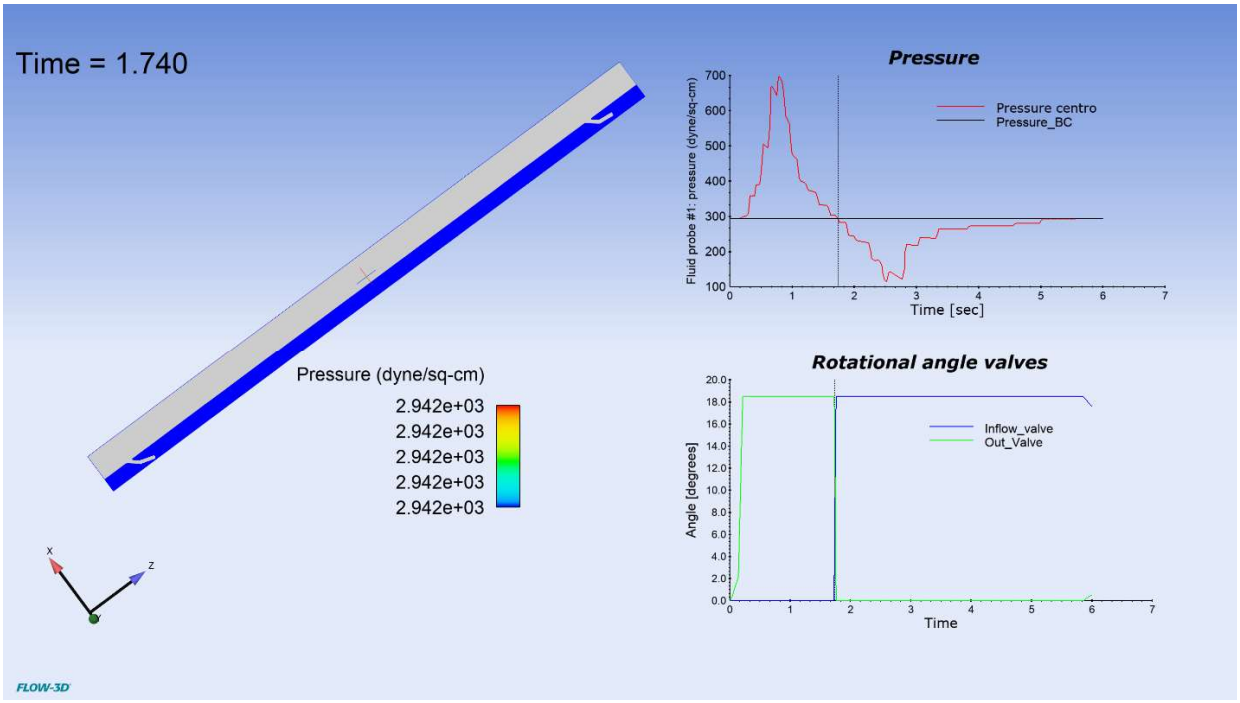

Figure 5. 26: Valve dynamic

This fast dynamic of valves is consistent with the physiological and biological modeling literature, where valves are described through an electric equivalence with a diode and the opening is considered instantaneous [45][18]. Moreover, it can be noted that valves switch from a closed state to a complete open one with a continuous movement without stopping in any intermediate position. This further remark emphasises how this movement is impulsive, and it will be useful in the next subchapter.

5.4.3 Improvements of the simulation

The simulation presented previously is characterized by a simulation time of 14 hours.

We can hypothesize that this high timing stems from valve's movement. As a matter of fact, in the previous simulation we used the GMO-coupled scheme of ***FLOW-3D*** for valves. Hence, the movement of these objects was computed at each time step starting from pressure and shear force exerted on them by the fluid. When valves open, the rapid dynamic and the pressure gradient involved requires several pressure iteration to converge. At each iteration the software must compute forces exerted by fluid on valves leading to an increase of the simulation time.

However, after having observed valve dynamics, a modelling hypothesis may be introduced to fasten simulations. In ***FLOW-3D*** it is possible to introduce the "Event" model, which enables triggering an event such as movement of a moving object conditionals to another occurrence.

Accordingly, if we introduce a probe close to valves, we can control the movements of these objects by imposing the respect of the previous observed pressure dynamic, namely

- If $Pprobes > Pout$, valves are closed;

- If $Pout > Pprobes$, valves are open;

where $Pout$ is the pressure boundary condition (the pressure of the inlet for the upstream valve and the outlet for the downstream one) while $Pprobes$ is the pressure measured in the probe.

In Figure 5.27 probes are characterized by green colour.

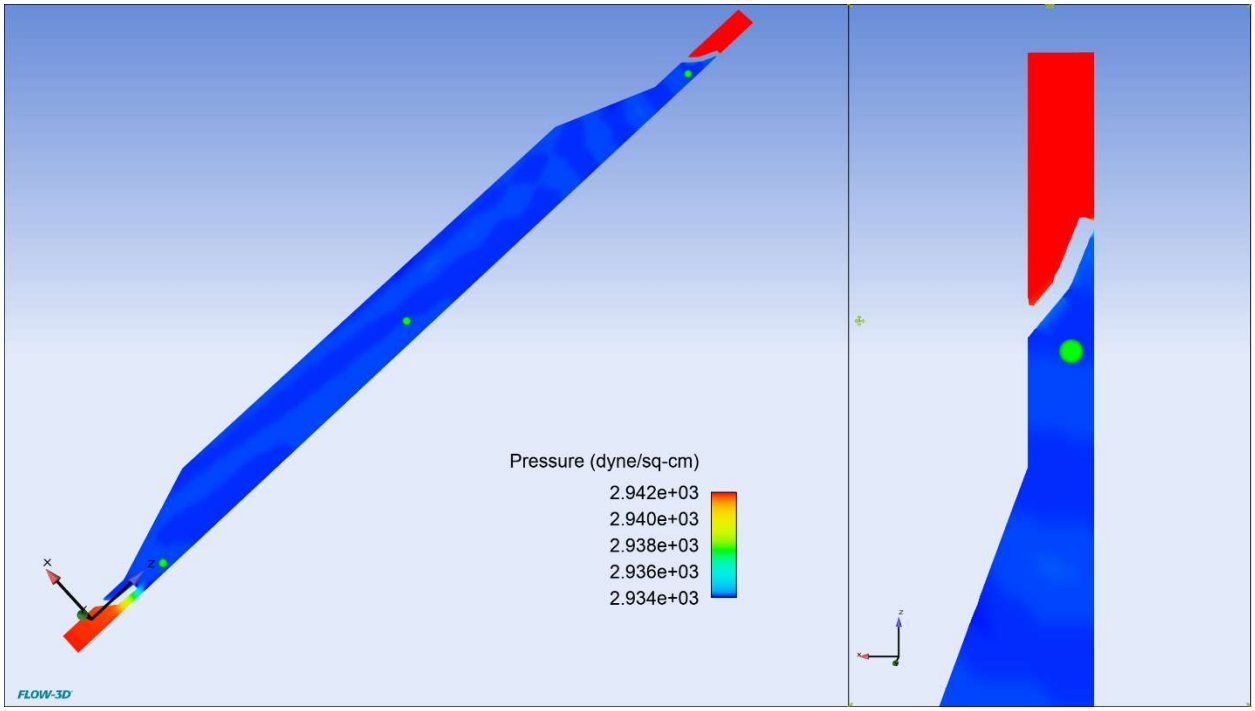

Figure 5.27: introduction of probes in the simulation

By doing that, we are reproducing the physics of the problem. In fact, with the "Event" model valves movement will be triggered in agreement with pressure dynamic inside the lymphangion. However, we can also use the prescribed model of *GMO* for valves with which the movement of valves is not computed starting from the fluid-interaction problem but is imposed a priori. Hence, we expect a significant reduction of the simulation time. To prescribe valve movement, we must compute the angular velocity of these objects. To this purpose, we analyze the outlet valve movement reported in in Figure 5.28 which stem from the simulation shown previously.

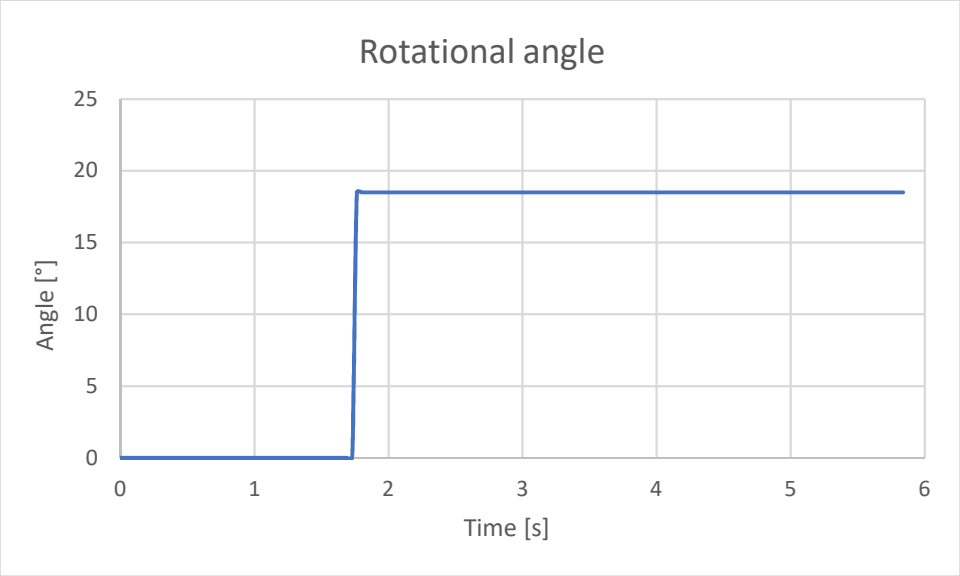

Figure 5.28: movement of valve

Valve is initially closed, i.e. rotational angle = 0°. The rotation starts at 1.76 s and it is completed in 0.1 seconds. Since the movement is fast and continuous, initially we approximate this movement with a linear relationship. Hence, will rotate with a constant angular velocity of 1.85 °/s.
Running the simulations with the prescribed scheme, the results do not change, as showed in Figure 5.29.

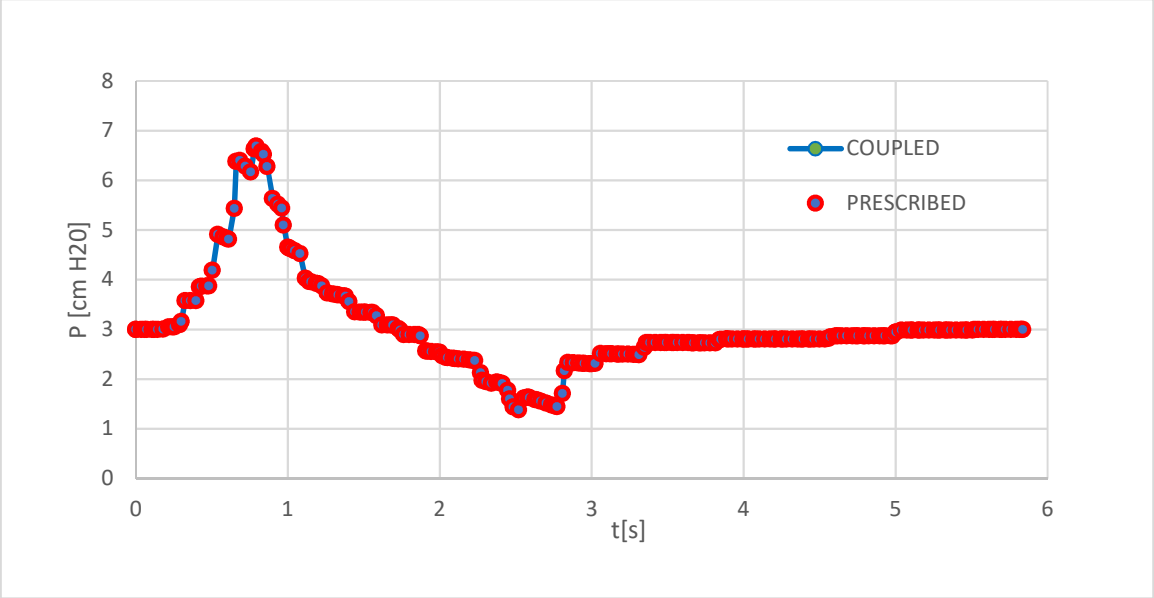

Figure 5.28: comparison of time-rate of change of pressure with the coupled and prescribed GMO model for the movement of valves

Figure 5.28 confirms that with our assumption we are able to reproduce the physics of the problem. Moreover, with this strategy we dramatically reduce simulation time (from 13 to 1 hours).

Having obtained a faster simulation, the aim of the next chapter is to develop the model considering a chain of lymphangions not only to be able to define a numerical set-up closer to the one contained in [7], but also to observe the dynamic with a chain of lymphangions.

CHAPTER 6
SIMULATION OF A CHAIN OF LYMPHANGIONS

In this chapter we will develop a numerical simulation accounting for 5 lymphangions.
After describing the numerical set-up in section 6.1, we will introduce a modeling hypothesis regarding the movement of valves based upon observations made in chapter 5.5. Then, in section 6.2 we will perform a parameters' calibration to reproduce the experimental curve reported in [7].
Finally, we will compare the numerical results with the experimental one recorded by Davis [7] and we will also make additional observations regarding fluid-dynamic behaviour.

6.1 Features of a simulation of a chain of a lymphangions in FLOW-3D

Our goal is to develop a numerical model comprising of five lymphangions. This geometric representation allows us to define a numerical set-up similar to the experiments of [7] which is reported in Figure 6.1.
After having shown the set-up of the simulation, in Section 6.1.2 we will describe the hypothesis on valve's behaviour stemming from the results of Chapter 5.

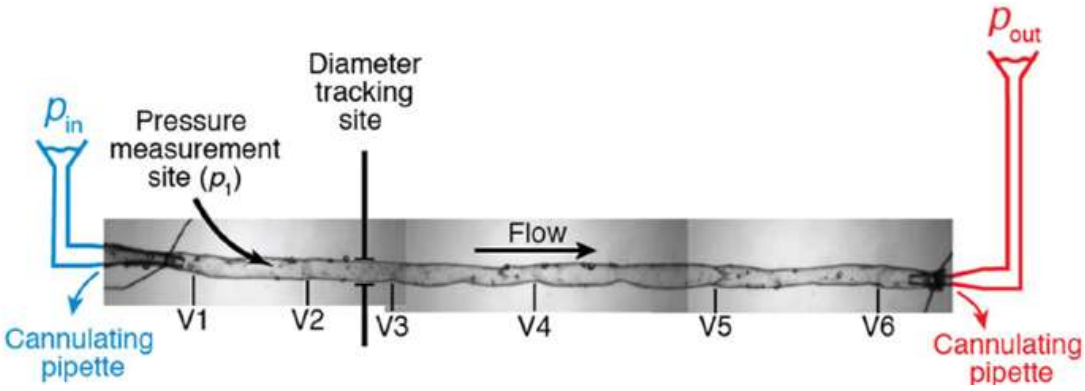

Figure 6. 1:experimental set-up of the lymphangion chain described in [7]

6.1.1 Set-up of the simulation

We hypothesize the 5 lymphangions to be equivalent geometrically and characterized by the same time-diameter relationship. Hence, we maintain the same description of the lymphangion already shown in Chapter 5. Specifically, we replicate each component and subcomponents constituting the vessel. Then, we translate them of the desired quantity to obtain a geometry composed of five lymphangions. The computational domain in ***FLOW-3D*** is represented in Figure 6.2.

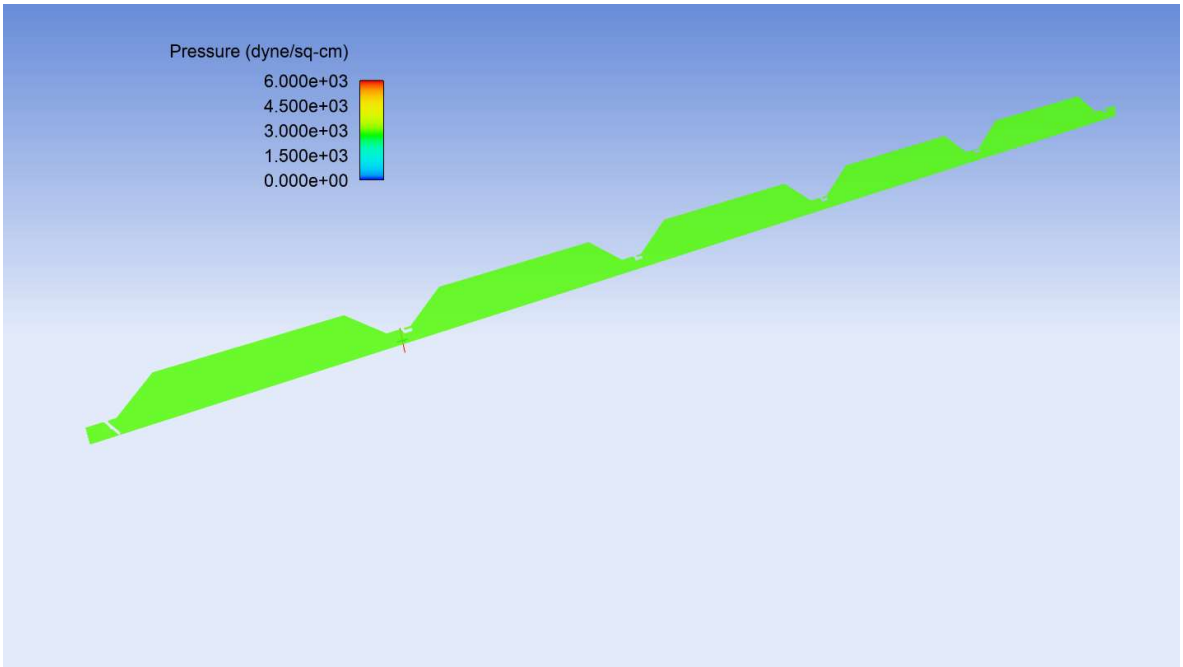

*Figure 6.2:Simulation of a chain of lymphangion in **FLOW-3D***

As in Chapter 5, a calibration parameter of the simulation is the maximum opening angle of valves. Moreover, the subsequent lymphangions do not contract simultaneously but they are characterized by a delay [11]. Since there is not an absolute reference in the physiological literature and in the work of [7]

regarding this quantity, we will consider it a second calibration parameter of the simulation. We can now describe the proposed hypothesis regarding valve movement.

6.1.2 Valve movement hypothesis

The new numerical set-up may lead to a dramatic increase in the computational time. However, based on the fluid dynamic behaviour observed previously, we can optimize the simulation.
We indeed observed in section 5.4 how using a coupled scheme of GMO for valves movement increased the simulation time. However, we demonstrated that valve dynamics is passive and depends on the pressure developed inside the chamber. Furthermore, we showed how the time-rate of change of pressure and diameter were strictly interconnected. Starting from these results, we propose a valve movement scheme based on time rate of change of diameter. This hypothesis does not affect model capability to reproduce physiological features of the lymphangion. Meanwhile, it enables us to run the simulation using a prescribed model of the GMO for the valve and fasten the simulation.
Only for the purpose of illustrating the formulation of our hypothesis, we consider a time delay equal to 0.5 seconds. Consequently, time-diameter behaviour of the five lymphangions is the one reported in Figure 6.3.

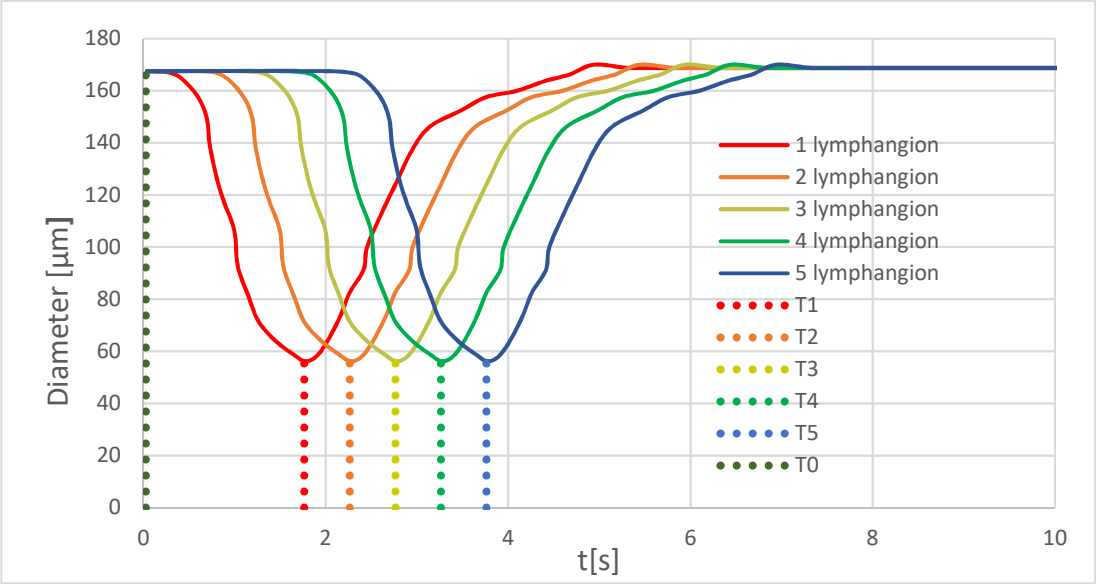

Figure 6.3: Time-diameter curve of five lymphangions with Td = 0.5 s

Specifically, time t_i represent end-systolic instants for each lymphangions (moments corresponding to the minimum diameter) and they are separated by a time-delay of 0.5 seconds.
We focus on the behaviour of the first and the second lymphangions before generalizing to the entire chain. We report the time-rate of change of diameter of these 2 lymphangions in Figure 6.4.

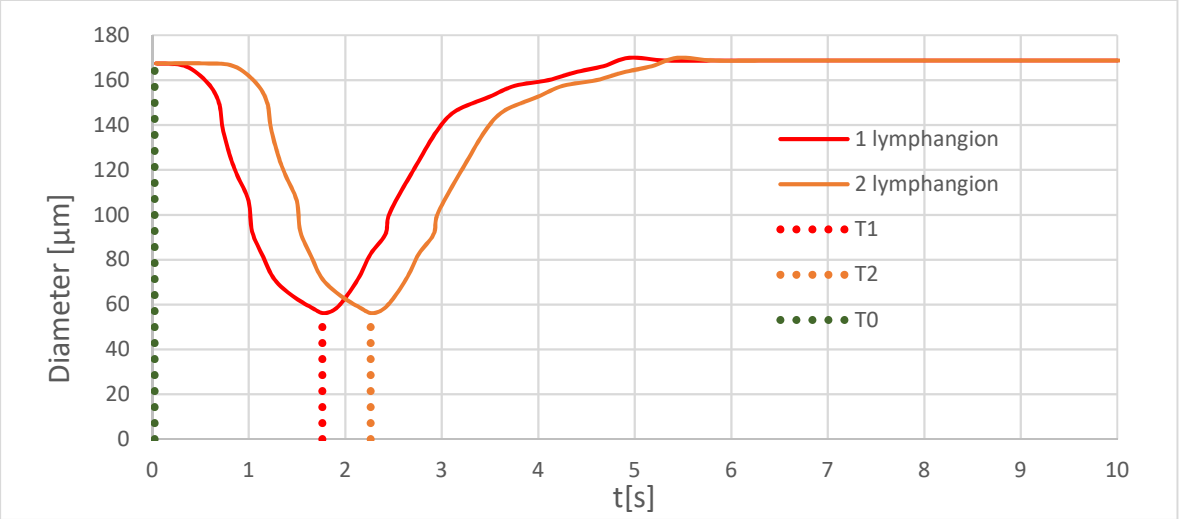

Figure 6.4: Time-diameter curve of 1st and 2nd lymphangions with Td = 0.5 s

At t_0, all valves are open except the first one which is closed and the fluid region is initialized everywhere equal to the boundary condition value (294.2 Pa). The first lymphangion starts contracting at t_0 while the second will move at 0.5 *s* because of the imposed time delay. In each instant between t_0 and t_1, the pressure in the first vessel is higher compared to the second one (as will be demonstrated in section 6.2.1). Hence, the outlet valve of the first lymphangion will remain open.

At t_1 the first lymphangion ends the systole phase, and it experiences the minimum diameter. Hence, a pressure equal to the initial condition is re-established inside the chamber and the inlet valve will open. Meanwhile, the second lymphangion is still compressing the fluid. Consequently, the outlet valve of the first lymphangion closes to prevent retrograde flow from chamber 1 to 2, as depicted in Figure 6.5.

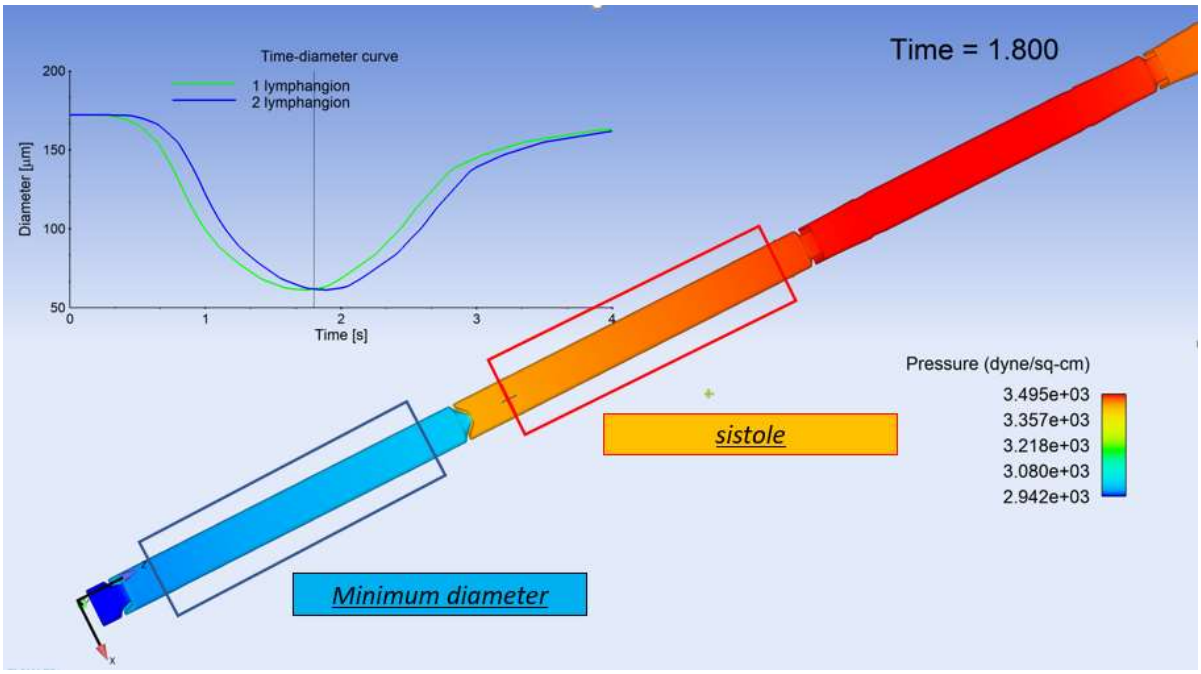

Figure 6.5: time rate of change of diameter at the end-diastolic instant of the first lymphangion

The other lymphangions are not yet moving and so, we can reasonably assume their valve to be in the same initial configuration. we can summarize valve behaviour at time *to and t1* in Table 6.1 where C means close and O open.

	valve_in	valve_1	valve_2	valve_3	valve_4	valve_out
to	**C**	O	O	O	O	O
t1	O	**C**	O	O	O	O

Table 6.1: Valves' movement scheme between to and t1

Where *valve_in* represents the inlet valve of the first lymphangion while *valve_i* the outlet valve of ith-vessel.
At t2 the second lymphangion will experience the minimum diameter. In the third lymphangion we have a higher pressure because this vessel is still compressing the fluid due to the time-delay. Hence the outlet valve, called valve_2 in Table 6.2, closes. Meanwhile the inlet one, called valve_1, opens. This procedure may be extended to all the other lymphangions. Consequently, defining *ti* as the time corresponding to the minimum diameter of the i-lymphangions, the scheme reported in Table 6.2 is proposed for valve movement

	valve_in	valve_1	valve_2	valve_3	valve_4	valve_out
to	**C**	O	O	O	O	O
t1	O	**C**	O	O	O	O
t2	O	O	**C**	O	O	O
t3	O	O	O	**C**	O	O
t4	O	O	O	O	**C**	O
t5	O	O	O	O	O	**C**

Table 6.2: General valves' movement scheme

As can be observed, valves change their state when each lymphangions experiences the minimum diameter and it leads to the diagonal matrix reported in Table 2. The proposed scheme stems from the pressure dynamic developed inside subsequent lymphangions and it agrees with the results shown in Chapter 5.
Moreover, once the time delay parameter is calibrated, we will know the value of time *ti* and, in turn, the timing characterizing the activation and closure of valves. Hence, we can use the prescribed scheme to describe their motion and we expect to significantly reduce the simulation time.

6.2 Calibration of the parameters of valve opening and time delay

In this section we will calibrate the two parameters of the simulation, maximum opening angle and time delay. In Section 6.2.1 and 6.2.2 we will analyse them separately to study their respective impact on the simulation. Based on these observations, we will define their value in the final set-up of the simulation in section 6.2.3.

6.2.1 Opening angle in the new simulation

In this section we study the fluid dynamic behaviour in the lymphangion chain without considering the dependence on the time delay *Td*. Hence, we hypothesize the five lymphangions to contract simultaneously (*Td*=0*)*. By doing that, we can study the impact of maximum opening angle of valves in this simulation.

We assume the five lymphangion to be characterized by the same maximum opening angle. However, this quantity will differ from the calibrated value for the model of the equivalent lymphangion. Specifically, we expect it to be bigger. To explain this concept, we consider pressure dynamic.

We are describing a vessel composed by five lymphangions and we expect each valve to determine a pressure drop. If we consider the ideal case in which each valve is subject to the same flow rate Q, we expect the pressure behaviour reported in Figure 6.6.

Figure 6.6:Ideal pressure drop in a lymphangion chain

Since Td =0, the five lymphangions simultaneously start compressing the fluid and putting it into motion and each valve determines a pressure drop ΔP.

Hence, in the last lymphangion a pressure given by P +2 ΔP is established. The fourth experience a pressure of P +2 ΔP, which stems from the pressure drop of two valves. This procedure can be extended to the entire chain. Consequently, the first lymphangion is affected by all the previous valves and its chamber experiences an increase of pressure equal to P +5ΔP. Hence, in this ideal case, the maximum opening angle of valves would stem from

$$P_{BC} + 5\alpha \cdot Q(t) = (P + 5\Delta P)_{experimental} \qquad \text{Eq(6.1)}$$

Conversely, in the simulation of the equivalent lymphangion, only one valve determined the pressure drop experienced by the lymphangion, namely

$$P_{BC} + \Delta P'_{equivalent} = (P + 5\Delta P)_{experimental} \quad \text{Eq(6.2)}$$

where:

$$\Delta P' = \alpha_{equivalent} \cdot Q(t) \quad \text{Eq(6.3)}$$

Comparing Eq (6.1) with Eq(6.2), we expect a smaller value of α when dealing with five lymphangions compared to the simulation described in Chapter 5.

Having made this premise, we can analyse the time-rate of change of pressure in the first lymphangion with different values of the opening angle. We limit the analysis to the contraction phase (1.76 second). For our purposes, this time window is enough, because we can observe the pressure behaviour generated by the synchronous contraction of the lymphangions in the different cases.

Regarding valves components, we maintain the same geometrical description of Chapter 5. We will only vary the maximum opening angle of the mobile flange in the different configuration.

Concerning the mesh, we maintain the same structure used in the model of the equivalent lymphangion. Hence, we define a uniform mesh with a cell dimension of 2e-4. Since we expect a smaller cross-section reduction, we will have a bigger number of cells into the valve cross section compared to the previous simulation. Hence, we consider the latter mesh capable of capturing fluid-dynamic behaviour in this configuration. Having defined this strategy, we considered three different configurations characterized by an opening angle equal to 27°, 32° and 37°, respectively. In Figure 6.13, we report the mesh configuration in two of the cases (27° and 37°).

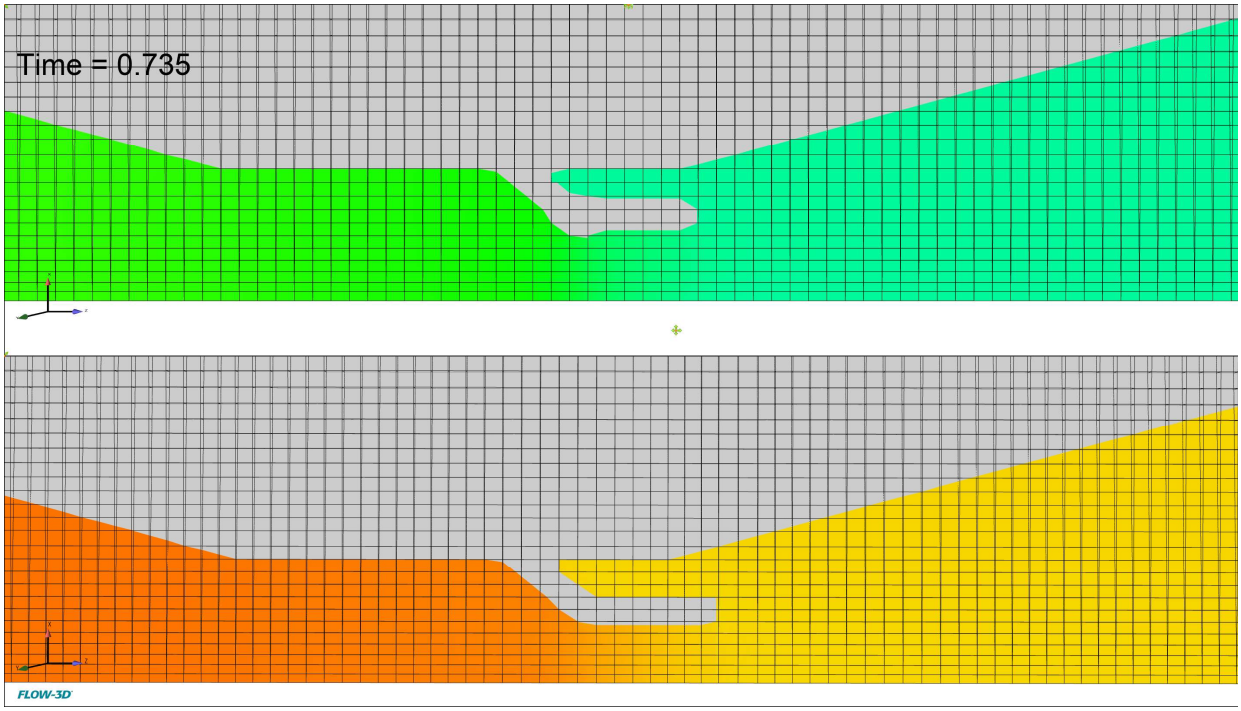

Figure 6.7: Mesh configuration in valve cross section an opening angle of 27° and 37°

In figure 6.14 we compare the volume flow rate crossing the outlet section of the first lymphangion in two configuration (27° and 37°) with the one computed in Chapter 5.

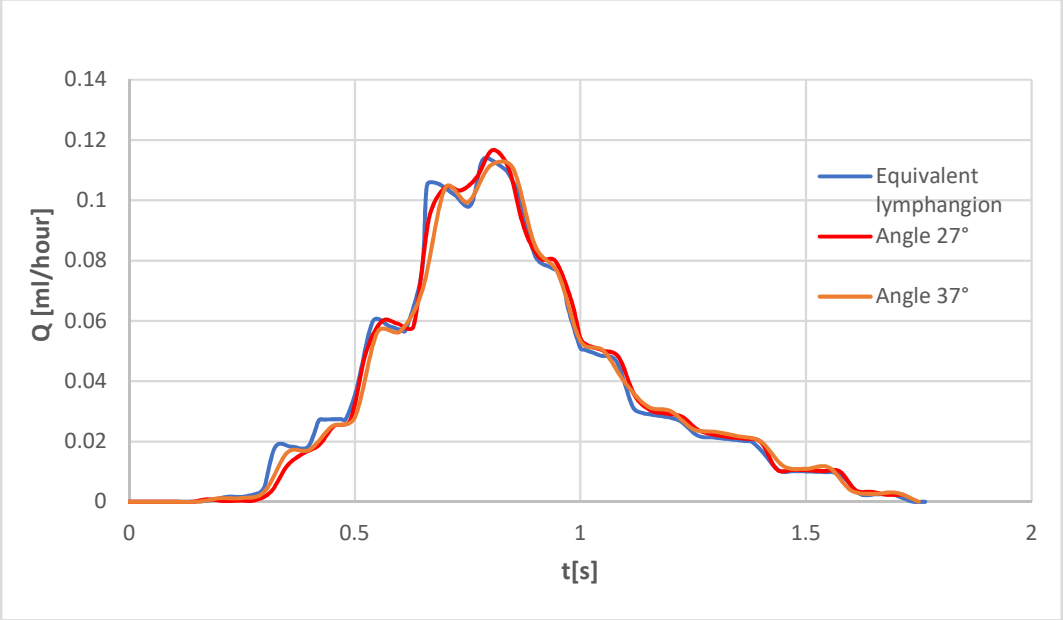

Figure 6.8: Outlet volume flow rate of the first lymphangion with 2 different maximum opening angle of valves (27° and 37°)

In agreement with mass conservation, the behaviour of discharge in the two different cases overlap the one observed in the simulation of the equivalent lymphangion. As a matter of fact, all the lymphangions of the chain are characterized by the same geometry of the equivalent configuration. Moreover, we are analyzing the first lymphangion, whose contraction starts at t=0 as for the vessel of the equivalent modeling. Hence, it is reasonable that the time rate of change of discharge does not change.
In Figure 6.9, we report the time rate of change of pressure in the first lymphangion with three different opening angles of valves compared to the simulation of the equivalent lymphangion.

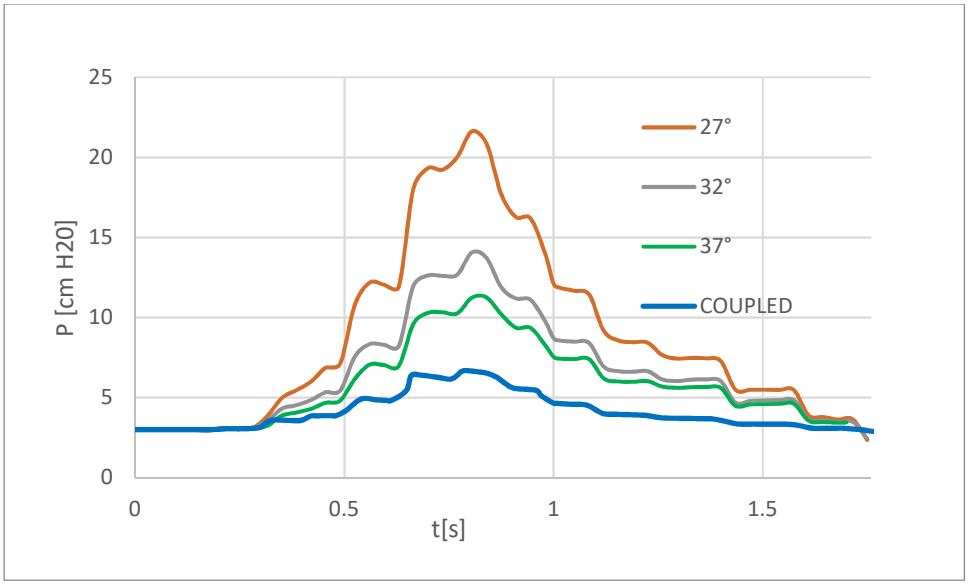

Figure 6.9: comparison of time rate of change of pressure varying the opening angle of valves

We can observe how the simulation of the equivalent lymphangion (called coupled) is characterized by a smaller time rate of change of pressure compared to all the tested configuration of the new simulation. This observation agrees with the theoretical framework previously described. We can further notice how increasing maximum opening angle, the pressure decreases maintaining the same shape.
Although we double the maximum opening angle (from 18.5° to 37°), pressure behaviour in the contraction phase is still quite different. We can now analyze by the parameter of the time-delay because, as already said, lymphangions do not contract simultaneously but they are characterized by a small delay.

6.2.2 Calibration of time delay parameter

In this section we maintain a fixed opening angle of valves (37°) to show the impact of the time delay. We will assume a positive time delay, meaning that the contraction of the second lymphangions starts later compared to the previous one, as done in [46].
The range within which we vary this parameter is between 0 and 0.5 s [11]. Also in this case, we limit the analysis to the contraction phase. In Figure 6.10 we compare the pressure behaviour of the model of the equivalent lymphangion with two cases characterized by a Td=0.05 and a Td=0.00 respectively.

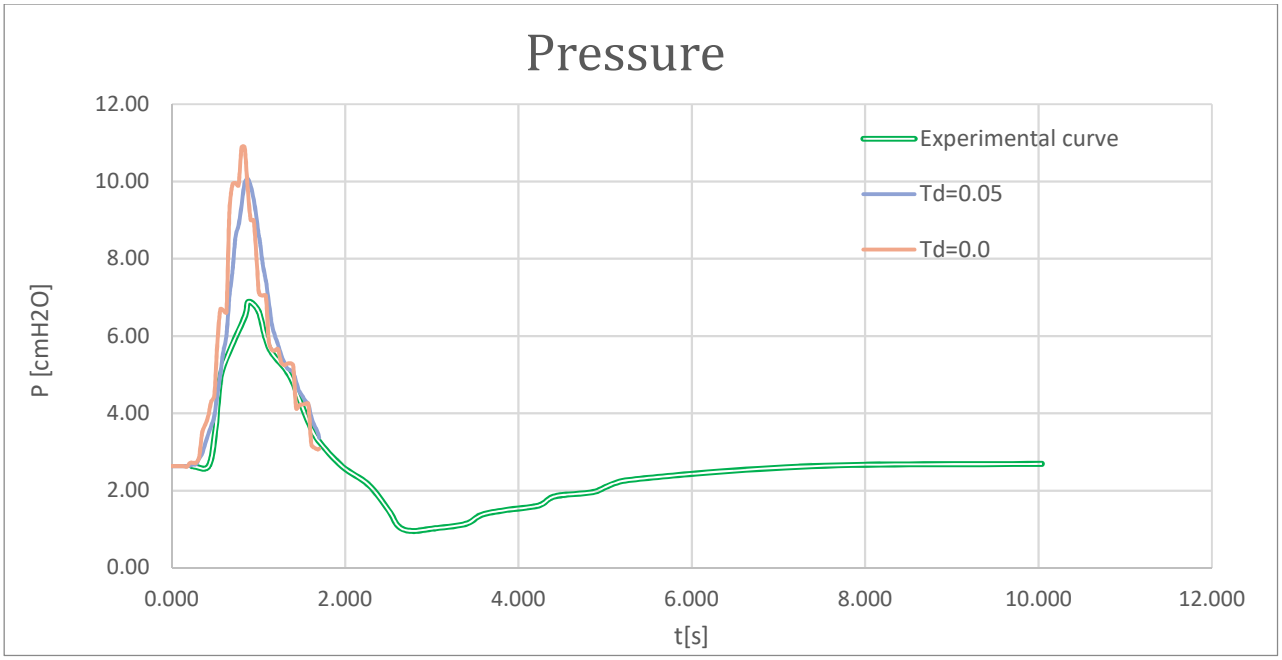

Figure 6.10:Comparison of time rate of change of pressure with different time delay

We can notice how the simultaneous contraction of five lymphangions results in the bigger increase of pressure inside the first vessel. This result may be explained using the previous theoretical analysis of pressure drop behaviour in the lymphangions chain.

Starting from the ideal situation described in Figure 6.6, we can specify the pressure experienced by the first lymphangion as

$$P_1(t) = P_{BC} + \Delta P'(t) + \Delta P''(t) \ldots + \Delta P^V(t) = P_{BC} + \alpha \sum_{i=1}^{5} (Q_i(t))^2 \qquad \text{Eq(6.4)}$$

Note that α is brought outside of the summation sign because we hypothesize valve's geometry and maximum opening angle to be the same throughout the entire chain.

If we introduce a time delay, we expect a different volume displaced in the unit time, which will be mirrored in the behaviour of pressure. Specifically, if at a certain time t less volume flows through a certain valve's cross-section, we expect a smaller pressure increase inside lymphangion chambers, in agreement with Eq (6.4).

We can verify the correctness of this theoretical argument in two different simulations, one characterized by Td=0.5 s and one by a Td=0 s. We report in Figure 6.17 the flow rate crossing the first lymphangion in both cases.

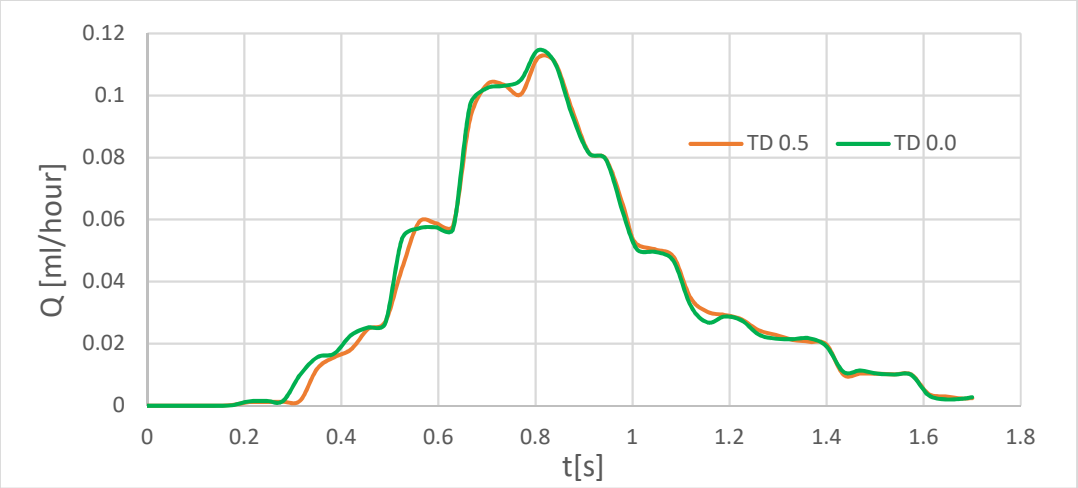

Figure 6.11: flow rate crossing the first lymphangion with Td=0.5 and Td=0

As expected, the two curves are overlapping. As a matter of fact, in both simulation the first lymphangion starts its contraction at t=t0. Given that we do not modify the geometry, discharge crossing the outlet valve of the first lymphangion is not going to change. Conversely, in Figure 6.18 we reported the flow rate crossing the valve of the fifth lymphangion.

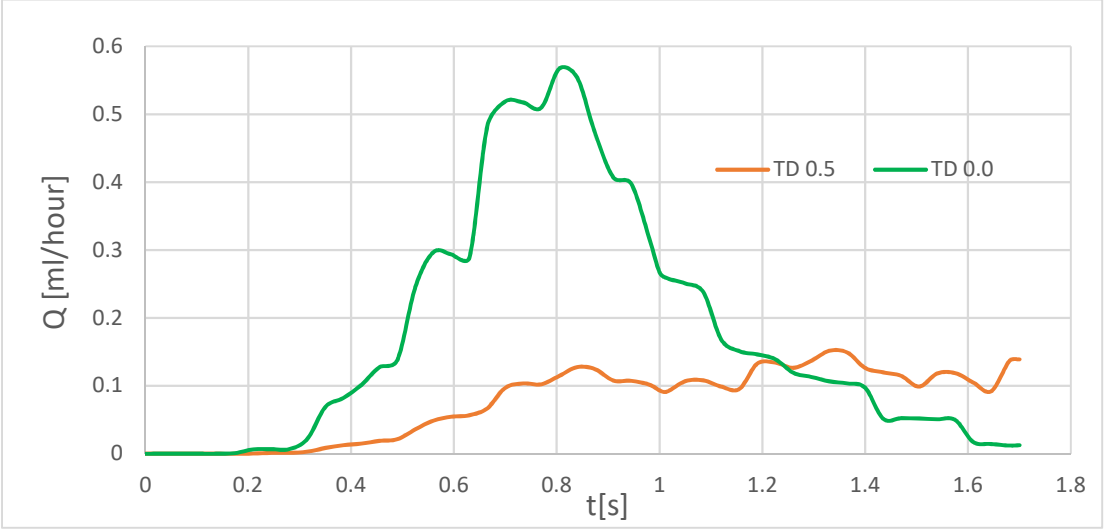

Figure 6.12: flow rate crossing the fifth lymphangion with Td=0.5 and Td=0

We can observe how the simulation characterized by a synchronous contraction experiences a peak at 0.8 seconds. This is given by the displacement of the whole fluid volume inside the lymphangion chain. Consistently, it happens in the moment corresponding to the maximum diameter velocity (see Figure 5.23). On the other hand, the simulation with $Td = 0.5\ s$ exhibit a different shape, because the volume is progressively displaced when each subsequent lymphangion starts its contraction phase.

In fact, in this interval of 1.76 s, in the simulation characterized by Td=0 s all the lymphangions have completed their contraction phase. Conversely, if we have a Td=0,5 only the first lymphangion has ended its contraction phase. As a result, the different behavior of Q caused by the time delay is reflected in pressure

behavior throughout the entire lymphangion chain. For instance, in figure 6.13 we report time rate of change of pressure in the first lymphangion with *Td*=0 s and *Td*=0,5 .

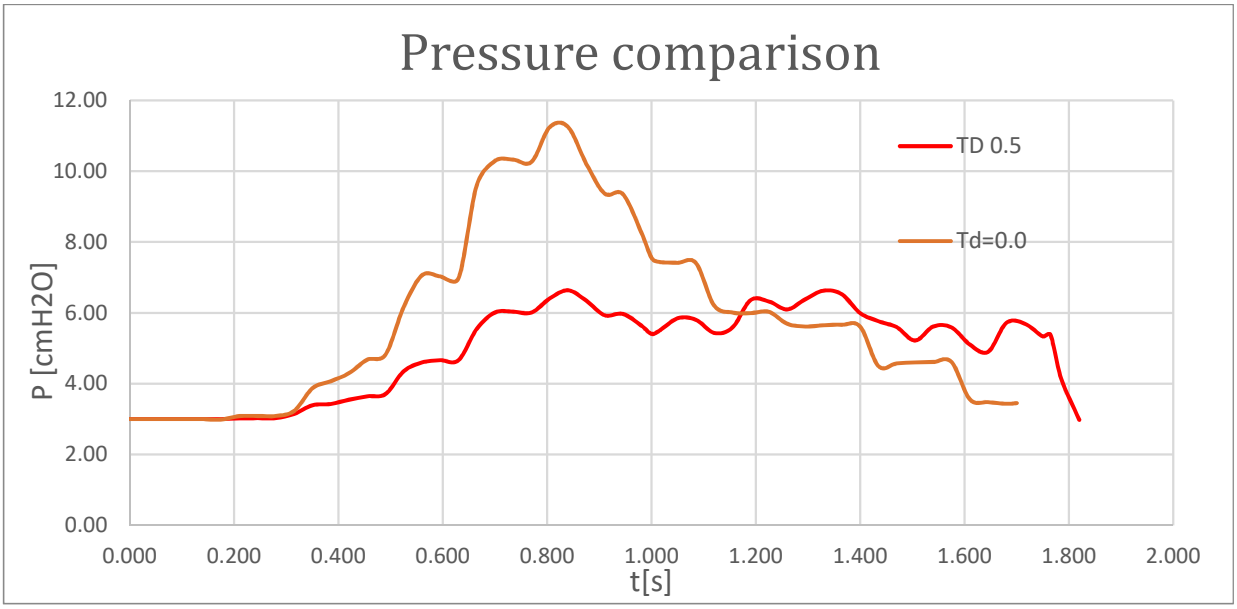

Figure 6.13:time rate of change of pressure with Td=0, Td=0.05

In the simulation characterized by *Td*=0 the lymphangions experience higher pressure and we can observe a peak at T=0.8 seconds. Conversely, we can observe a flatter curve if we consider a TD=0.5 s and it is more difficult to identify a peak.

We can consider another tested configuration (run for a bigger time-frame), characterized by a TD=0.15 s and represented in Figure 6.14.

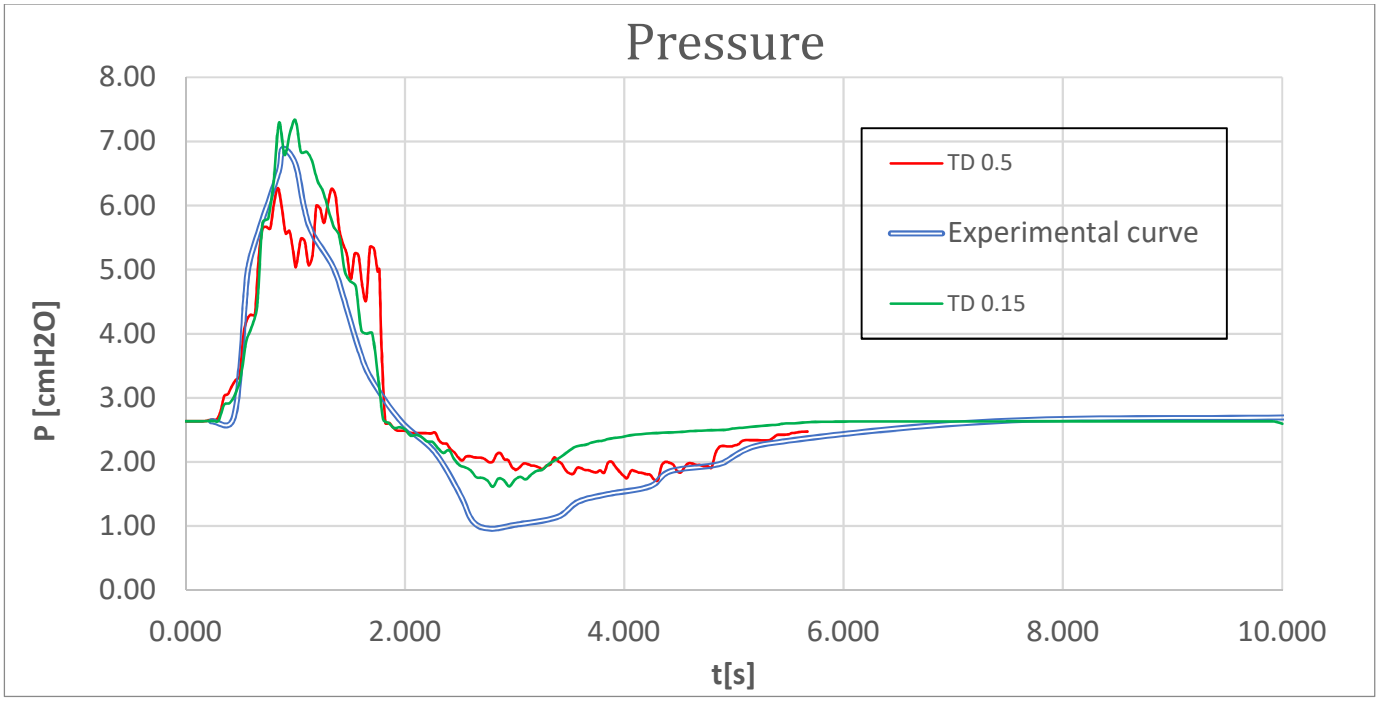

Figure 6.14: Comparison of time rate of change of pressure recorded experimentally with the simulated one with Td=0.15 and Td=0.05

We can observe how the time-delay affects both systole and diastole phase and as time delay increases we observe a smaller pressure inside the lymphangion compared to the case of a synchronous simulation in both the two phases.
The curve with a bigger time-delay seems to be wider and characterized by two lower peak if compared to the experimental or the one with a TD=0.15, where it is clear the peak happening at 0.8 seconds.
This is interestingly because fluid-pumping is one of the most important tasks of the lymphangions. Our plot clearly shows how if the delay between subsequent contraction increases, we have a reduction of the effectiveness of fluid pumping.

6.2.3 Parameters of the simulation

Starting from the observations of the previous section, we can calibrate the values of the parameters of the simulation. In the final set-up we consider:

- A maximum opening angle of 37,5°;
- A time delay between each lymphangion of 0.15 s;

Moreover, knowing the time-delay parameter, we know the instant where valves will move and we can use the prescribed GMO model of ***FLOW-3D***. To this purpose, we yet need to define angular velocity of valves.

To define the latter quantity, we start again from the results of the model of the equivalent lymphangion described in Chapter 5. In that simulation it took 0.1 s to complete opening or closure movement (so to describe an angle of 18.5°). Moreover, we observed how this time was negligible compared to the perturbation causing the valve to move. Hence, we can reasonably assume timing to be equal to 0.1 s also in this situation. The angular velocity of valves is defined as:

$$\boldsymbol{vel\_angular} = \frac{\alpha(i+1) - \alpha(i)}{t(i+1) - t(i)} \qquad \text{Eq(6.5)}$$

and it leads to an angular velocity of 3,75 °/s.

6.3 Results

In this section we illustrate the results of the model.

6.3.1 Comparison between experimental and numerical curve

In Figure 6.15 we compare the experimental curve recorded in [7] with the one obtained numerically after calibration of parameters.

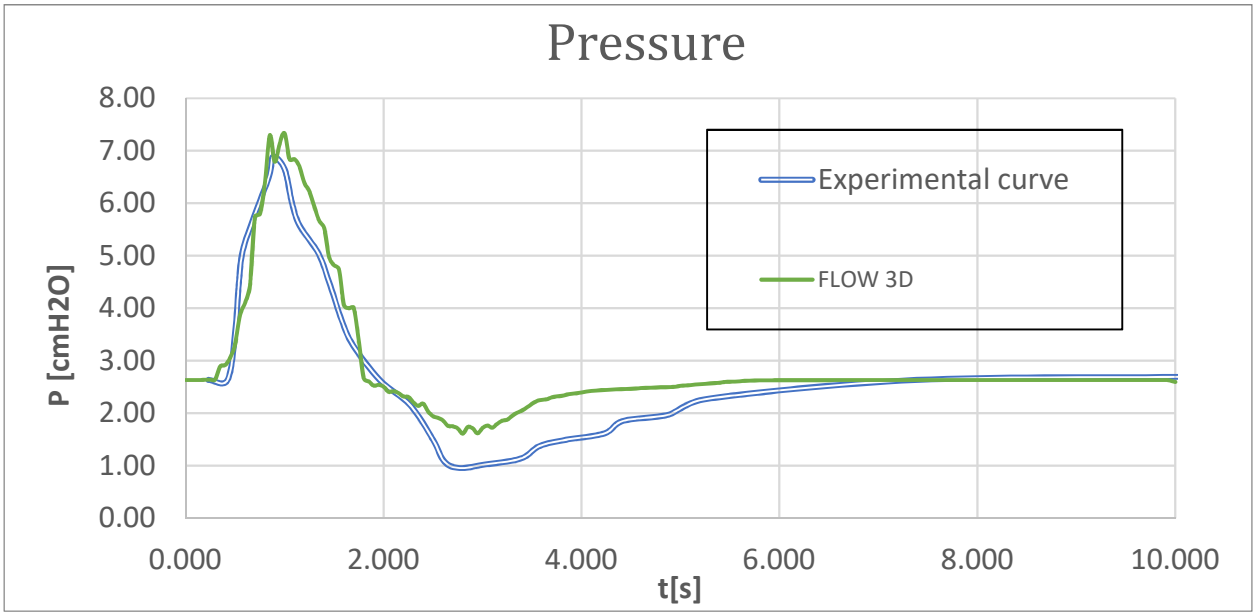

Figure 6.15: comparison between the time rate of change of pressure recorded experimentally and the numerical results

During the contraction phase the two curves are similar and almost superimposed. The numerical one is characterized by a slightly enlarged shape, but this may be a consequence of time delay assessment, in agreement with the observations of section 6.2.2.

In diastole, our model reproduces the shape of the pressure dip observed in the work of Jamalian and Davis [7]. However, the experimental curve reaches a lower value of pressure. A possible explanation for this discrepancy is that valves open and close of a different quantity, while in the simulation we assumed them to exhibit the same angle during both movements. Specifically, if the maximum opening angle is smaller in the recovery, a bigger pressure dip is going to be observed. This hypothesis seems to be consistent also because of the smoother shape of the curve in the relaxation phase which lead to smaller forces on the valves.

Finally, in Figure 6.16 we compare the curve obtained with the two modelling hypotheses showed in Chapter 5 (equivalent lymphangion) and in the current one (chain of a lymphangion).

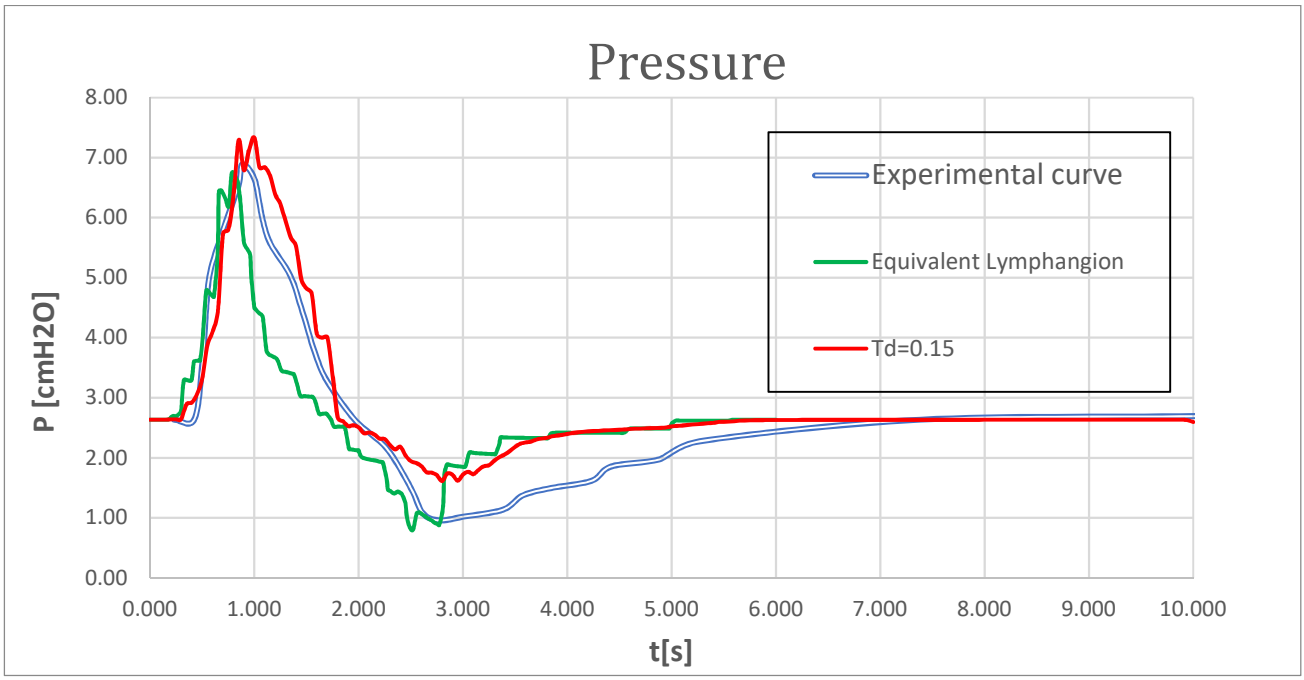

Figure 6.16:comparison between the time rate of change of pressure of the model of the equivalent lymphangion and the one of a lymphangion chain

We can observe how pressure gradient stemming from the model of the equivalent lymphangion is closer to the one measured experimentally. Conversely, the model comprising of five vessels reproduces better the shape of pressure both in the contraction and in the recovery phase and this is a consequence of the flow rate behaviour which will be described in the next section.

6.3.2 Pressure and volume flow rate behaviour in the lymphangion chain

Having showed the capability of our model to represent the experimental measurements reported in [7], we can now further investigate fluid dynamic behaviour throughout the entire chain. This is a crucial advantage of the computational model developed in ***FLOW-3D*** compared to the experimental set-up. In fact, in [7] pressure and diameter were recorded only in one location.

Conversely, in our model we can observe the interaction between the different lymphangions and their fluid-dynamic behaviour in each point throughout the computational domain. This is one of the potentiality of a numerical model compared to experimental set-up, where considering several measurement points may be expensive and it may also affect the experiment. We report pressure inside the lymphangion chain within the contractile cycle (10 s) in Figure 6.17.

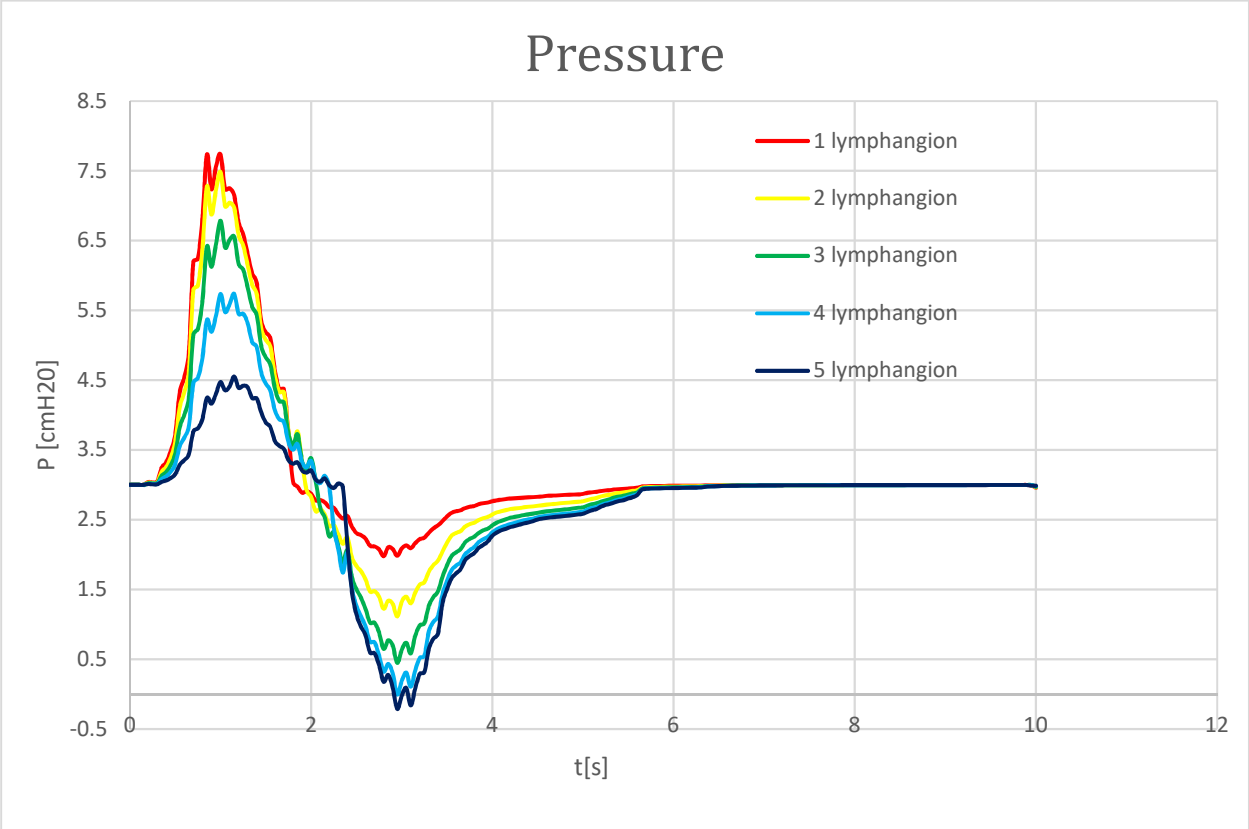

Figure 6.17:time rate of change of pressure inside the lymphangion chain

During contraction, the biggest pressure is established in the first lymphangion while in the subsequent element there is a progressive reduction of pressure until the last one, where the smallest pressure is developed. This result agrees with the hydraulic behavior of pressure drop reported in Figure 6.6.
Rigorously, pressure behavior in this configuration can be further specified as reported in Figure 6.18.

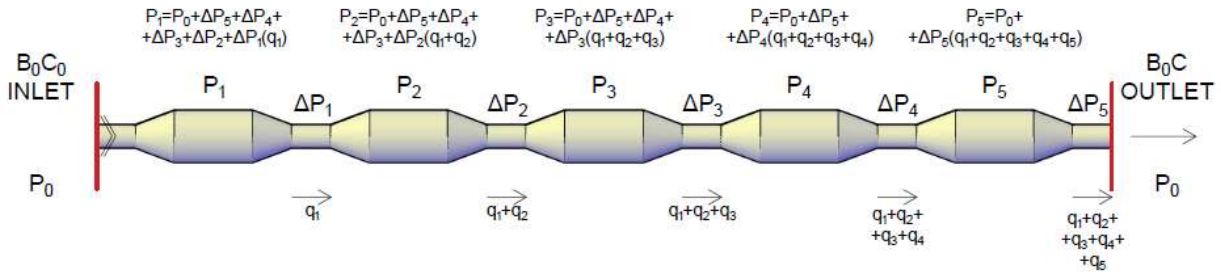

Figure 6.18:theoretical description of pressure drop behavior throughout the lymphangion chain in systole

Each pressure drop is indeed proportional to the discharge flowing through valve cross-section. These contributions determine the pressure established in each chambers compared to the pressure boundary condition P_o.

It is worth noting that the time rate of change of pressure of the first and second lymphangion differs of a small quantity, which is given by the pressure drop caused by the first valve, called ΔP_1.The latter pressure drop is the smallest one because it is proportional only to q5, which is the discharge determined by the volume inside the first lymphangion. Conversely, the biggest pressure drop in modulus in this phase is the one of the 5th lymphangion, ΔP_5 , which is proportional to the sum of the discharges flowing throughout the lymphangion chain.

Overall, these contributions determine a negative pressure gradient throughout lymphangion's chain. This spatial gradient is crucial because it allows the fluid to be displaced toward the outlet section and it constitutes the driving force for movement in the contraction phase.

During the subsequent relaxation phase a negative pressure gradient is established throughout the chain again because of the pressure drop dynamic. At time t5, the last lymphangion experiences the minimum diameter. In agreement with Table 6.2, in this moment all valves are open except the inlet one which is closed. As a result, the boundary condition perceived by the lymphangions chain is the one at the inlet. Consequently, the pressure drop scheme is the one reported in Figure 6.19

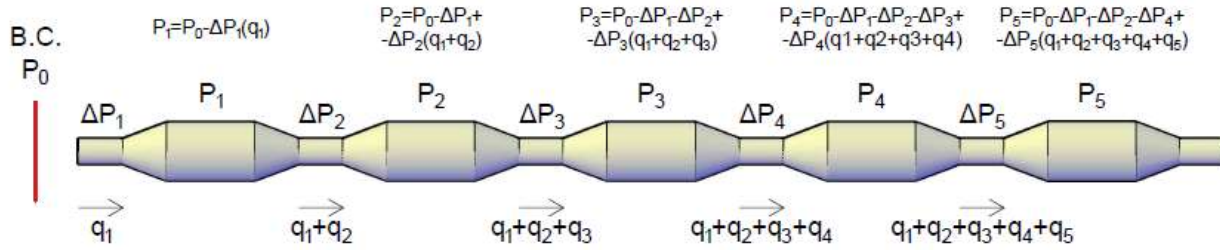

Figure 6.19: theoretical description of pressure drop behavior throughout the lymphangion chain in diastole

During relaxation phase, we have an increase of the diameter leading to a negative pressure drop in each chamber compared to the inlet boundary condition. The fifth lymphangion experiences the biggest pressure

drop as opposed to the contraction phase. As a result, a negative pressure gradient is established throughout the chain. It is worth noting that this remark is a quantitative evidence of the suction effect throughout the lymphangion chain and provide a mean to understand the presence of a flow in the lymphatic system from a subatmospheric pressure condition. As a matter of fact, based on the fluid-dynamic theory, we can conclude that the presence of a favourable gradient during diastole stems from the pressure and valves dynamic explained in Figure 6.19 and 6.20. The flux in the lymphangion chain is reported in Figure 6.20.

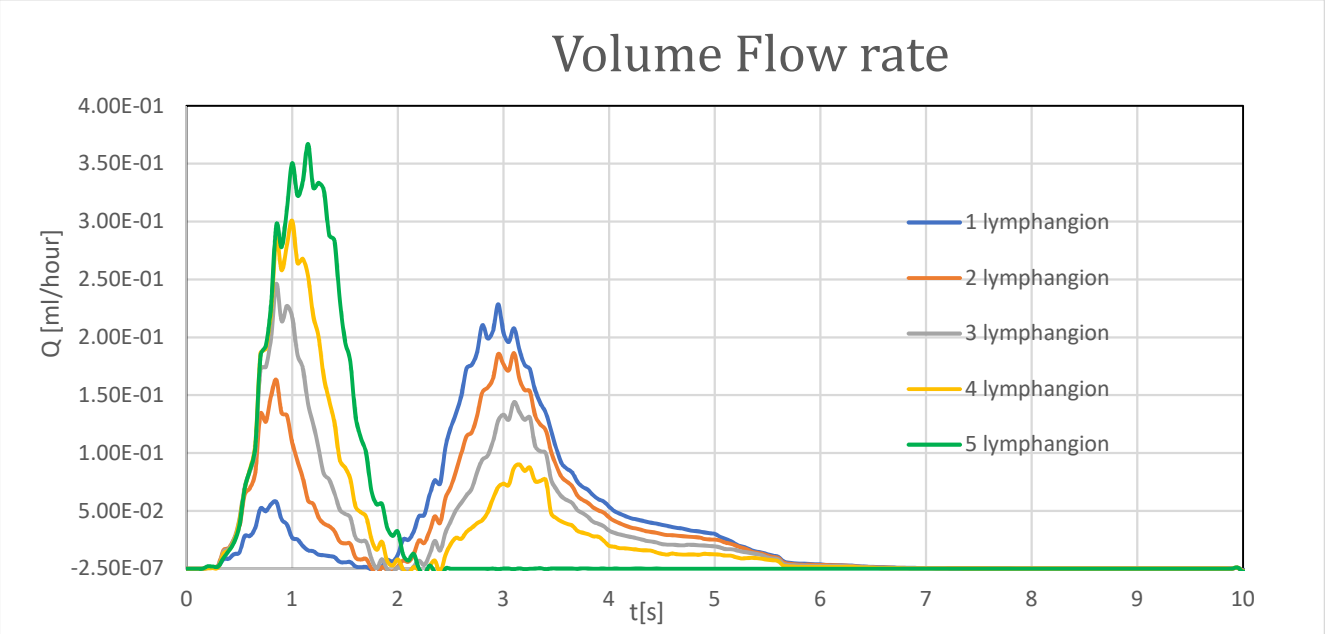

Figure 6.20: volume flow rate throughout the lymphangion chain

We can observe how during systole the fifth lymphangion experiences the biggest flow rate. This behaviour stems from the subsequent contraction of the lymphangions chain which determine a progressively greater volume to be displaced along the chain. During diastole we have the opposite situation, the largest discharge is witnessed by the first lymphangion because the inlet valve remains open throughout all the relaxation phase.

It is worth noting that, in agreement with what was observed by Bertram in [45], during valve's movement we have a small (and negligible considering order of magnitude) retrograde flow. This happens because valves dynamic is fast but not immediate. Hence, we have an infinitesimal time frame where a negligible amount of back-flow (with an order of magnitude of 1e-7) is observed.

Another possibility offered by ***FLOW-3D*** is to plot the flow-streamlines. Let us consider their behaviour immediately before and after the valves closes. In Figure 6.21 we represent both the velocity field as well as the streamlines in one single lymphangion of the chain before the closure of the outlet valve.

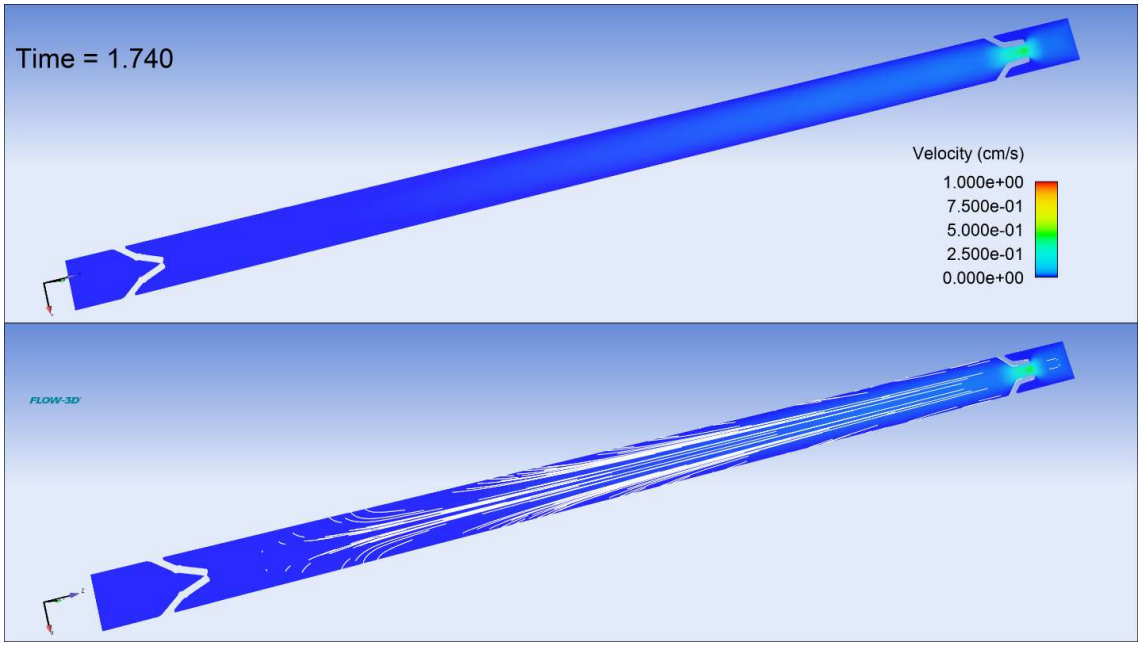

Figure 6.21: velocity field and streamlined at t=1.740 s

We can observe how the streamlines converge toward the outlet where we have the highest velocity. Conversely, in Figure 6.22 it is plotted the moment corresponding to the opening of valves.

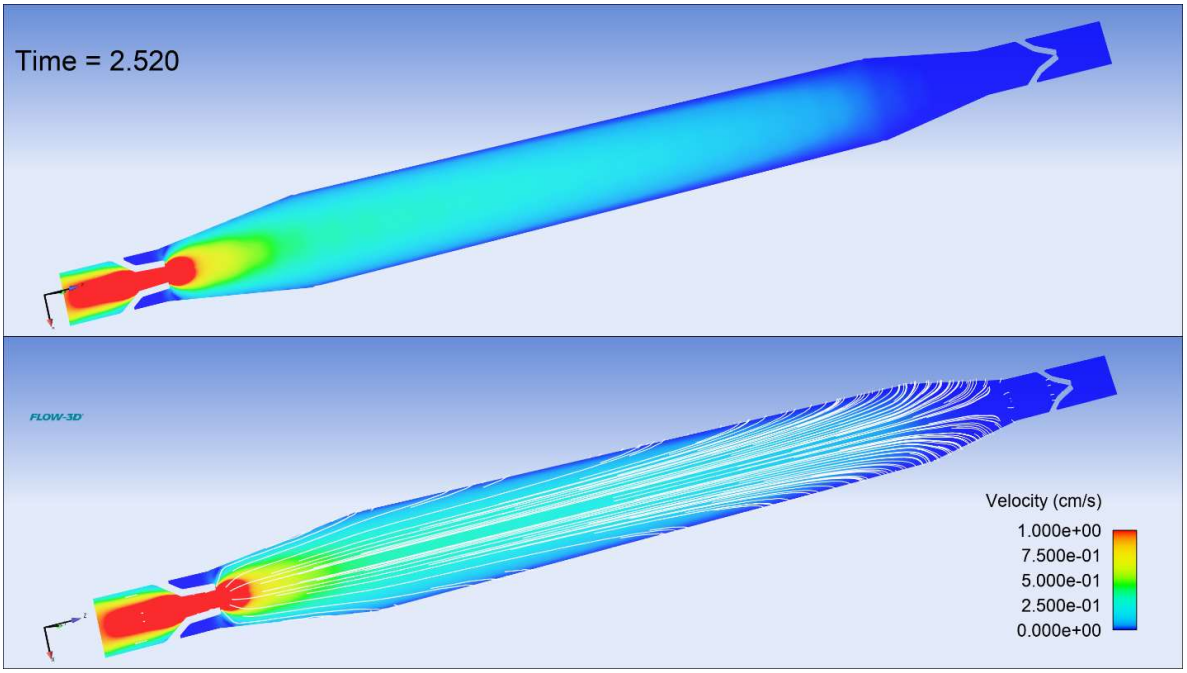

Figure 6.22: velocity field and streamlined at t=2.520 s

In this case, the streamlines tend to divert inside the lymphangion following the expansion of the diameter.

6.3.3 Boundary condition dependency

We can make an additional remark related to boundary condition dynamics. Let us subdivide the contraction cycle in three different time intervals

- To – t1
- T1- t5
- T5-10 s

To – t1

The first subinterval defines the time between initial condition and the end of the contraction of the first lymphangion. This time window is characterized by the initial valve configuration (all valves open except the last one which is closed). Throughout this time frame, the whole lymphangion chain experience the outlet boundary condition, which defines the time rate of change of pressure inside subsequent lymphangions.

When the contraction of the first lymphangion ends, so at time t=T1, we have the coupled behaviour of valves of this vessel. Hence, the inlet valve opens while the outlet valve closes.

It is worth noting how this valve's dynamic has the consequence that each lymphangion chamber perceives one boundary condition separately per time. In other words, valves' movement define the single boundary condition which each lymphangion is exposed to.

In fact, at T1, the first lymphangion stops depending on the outlet boundary condition and experience the inlet one. On the other hand, the other lymphangions still perceive the outlet boundary condition because they are yet contracting (due to time delay). Hence, we have an isolation of the volume of the first lymphangion from the others given by the outflow closed valve. This situation can be clearly in Figure 6.23.

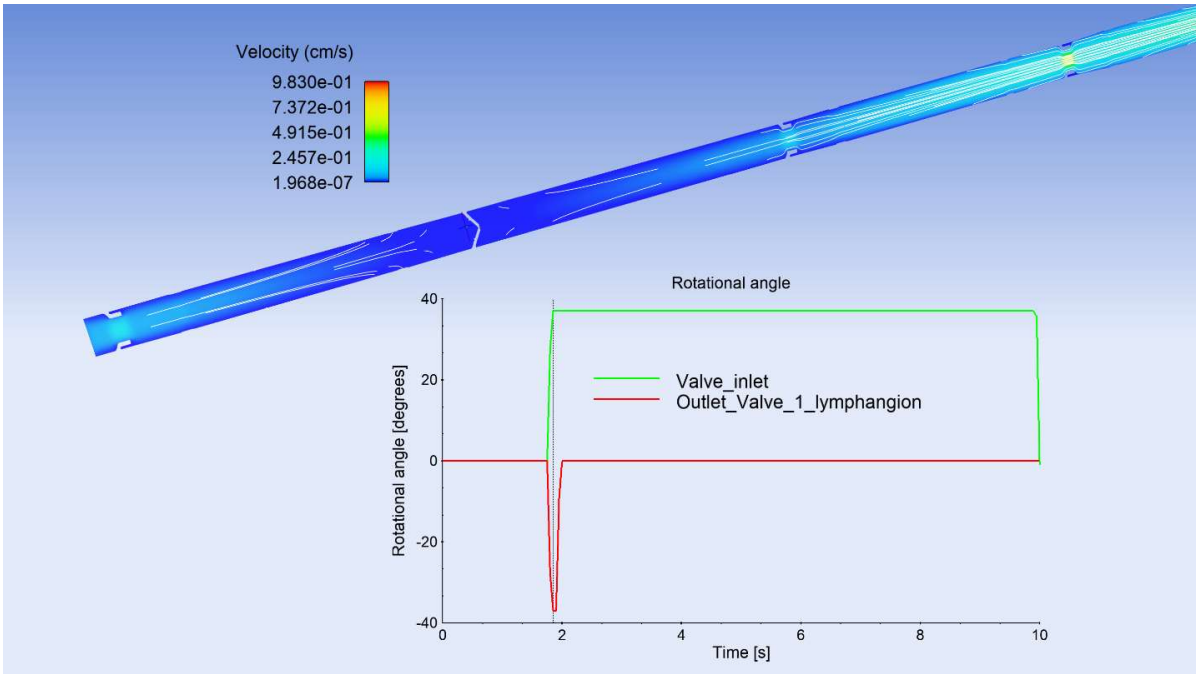

Figure 6. 23: boundary condition dynamic corresponding to the minimum diameter of the first lymphangion

T1 – t5

As time goes by subsequent lymphangions ends the contraction and there is the progressive closure and following opening movement of valves.

For instance, at t2 the second lymphangions will reach the minimum diameter condition and it will be exposed to the change of boundary condition (it will perceive the inlet one).In this moment, both the volume of the first and second chambers of the lymphangions feels the initial condition and, accordingly, this volume will be isolated by the other chambers thanks to the closed outflow valve of the second lymphangion.

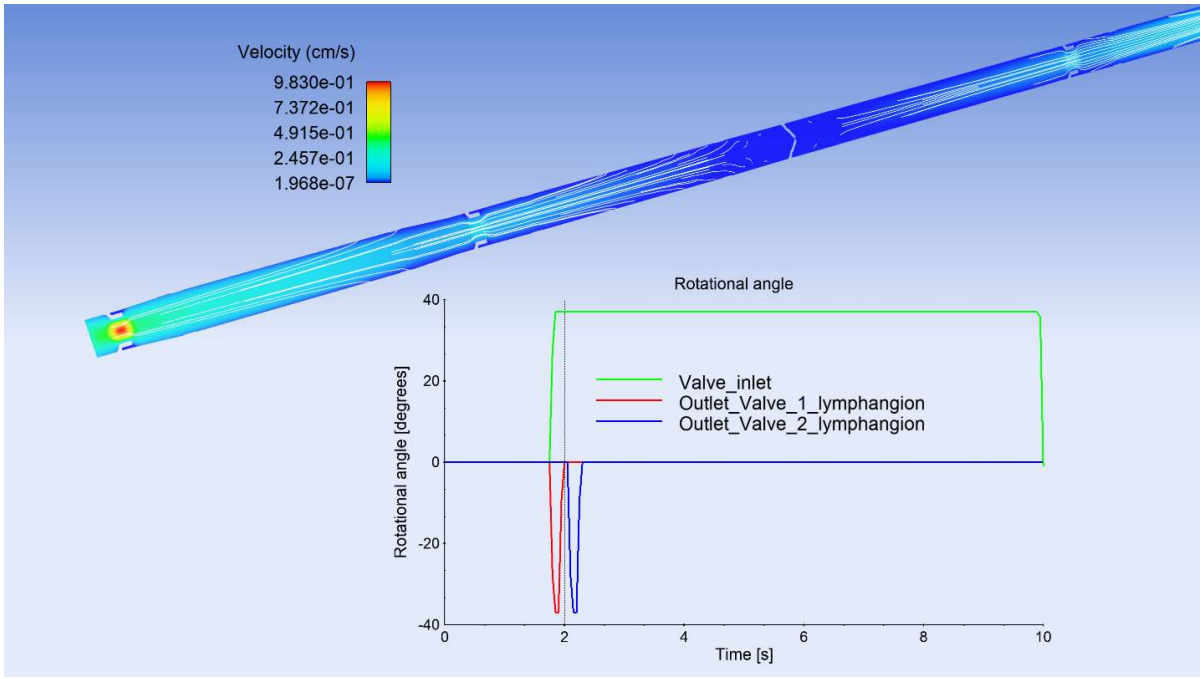

Figure 6.24: boundary condition dynamic corresponding to the minimum diameter of the second lymphangion

Progressively, this mechanism will apply to all the lymphangion chain until t5.

T5-10 s

In this moment, we have the opposite situation compared to the initial condition.

Now, all the valves are open except the last one and the entire chain feels the inlet boundary condition leading to the previous observed pressure and volume flow rate dynamic.

For instance, let us consider t=2.45 s.

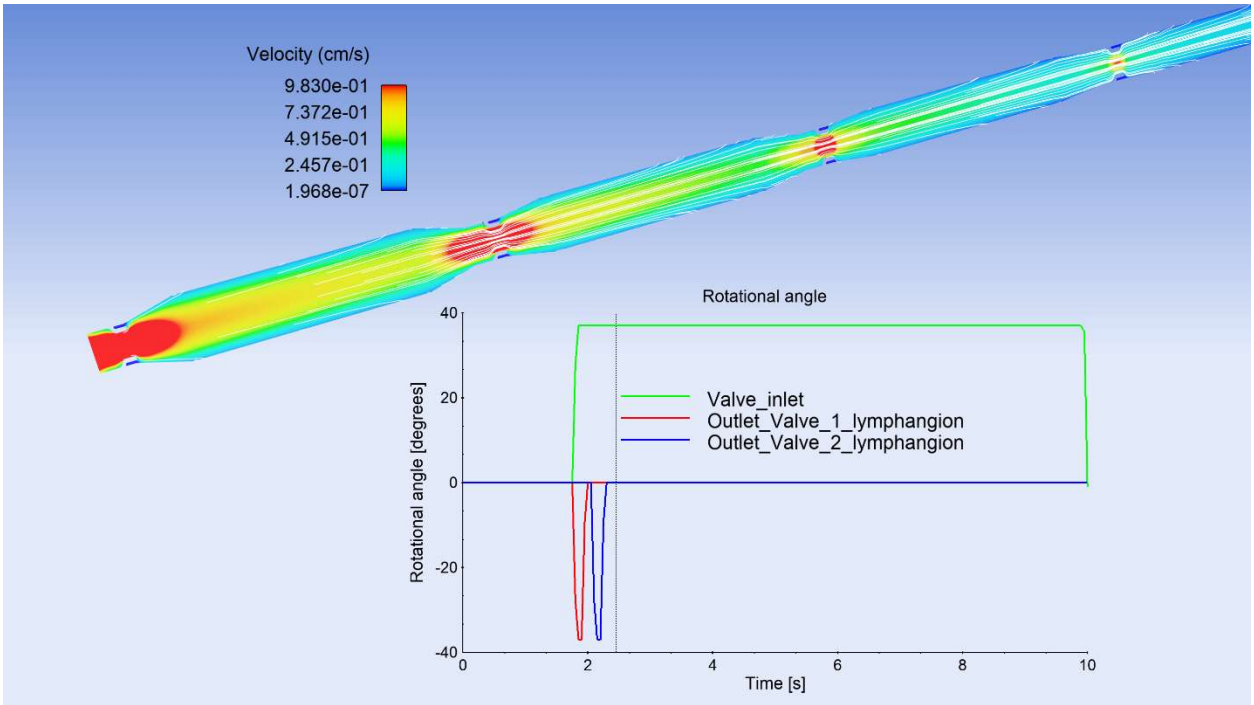

Figure 6.25: boundary condition dynamic at t=2.45 s.

Finally, we can summarize these concepts highlighting how the chain of lymphangions perceives one boundary condition at a time, either the inlet or the outlet. This condition defines the volume flow rate and the pressure gradient experienced by the whole chain. Moreover, within a contraction cycle, the lymphangion chain is exposed to both these conditions. According to what we have seen, it is reasonable to expect a dependency from the downstream boundary condition during contraction phase and a dependency from upstream during diastole.

This isolation of one of the two boundary conditions takes place also within each lymphangions of the chain. Specifically, it happens thanks to valve dynamic of one lymphangions which synchronously moves guaranteeing the respect of this condition.

Hence, we can subdivide the contraction cycle in two time intervals:

- Systole (contraction phase) when the outlet boundary condition defines pressure and volume flow rate behaviour
- Diastole (relaxation phase) when the inlet boundary condition defines pressure and volume flow rate behaviour

Between these two intervals there is a transition phase where each lymphangion, from the inlet to the outlet, progressively adequate to the new condition. This phase is characterized by a duration equal to the sum of the time-delay of each *i*-lymphangion inside the chain. Throughout this time frame, we have a gradual change of the boundary condition perceived by internal lymphangions of the chain. Interestingly, this mechanism leads to a progressive isolation of volume within the lymphangions chain similar to the behaviour of an hydraulic pump.

This dynamic of boundary condition it is intrinsically connected with the problem of lymph formation, i.e. how lymph enters into the lymphatic vessels from the interstitial space, where, in a physiological condition

a negative pressure takes place. According to our results, we can conclude that the explained boundary condition dynamic and pressure drop behaviour play a crucial for the presence of a negative pressure gradient during the contraction cycle of a lymphangion, which is the element allowing the fluid to move and to be transmitted along the lymphatic system.

CHAPTER 7
CONCLUSIONS AND FUTURE PERSPECTIVES

In this thesis we have developed two modeling approaches to study the fluid dynamic behavior of the lymphatic system. This system plays a vital role in human health and is involved in numerous diseases. Our work investigates the role of the lymphatic system in regulating overall fluid balance in the human body. Since a complete description of the problem at hand using partial differential equation is computationally unaffordable, we performed a model reduction developing a lumped parameter approach based on the fluid-electric analogy. The proposed model describes fluid balance at the scale of the human body and includes the cardiovascular system, the lymphatic system, and the interstitial space. In this systemic computational environment, we have analyzed fluid flow through the lymphatic network from the formation in the interstitial space to return to the venous side as depicted in Figure 7.1.

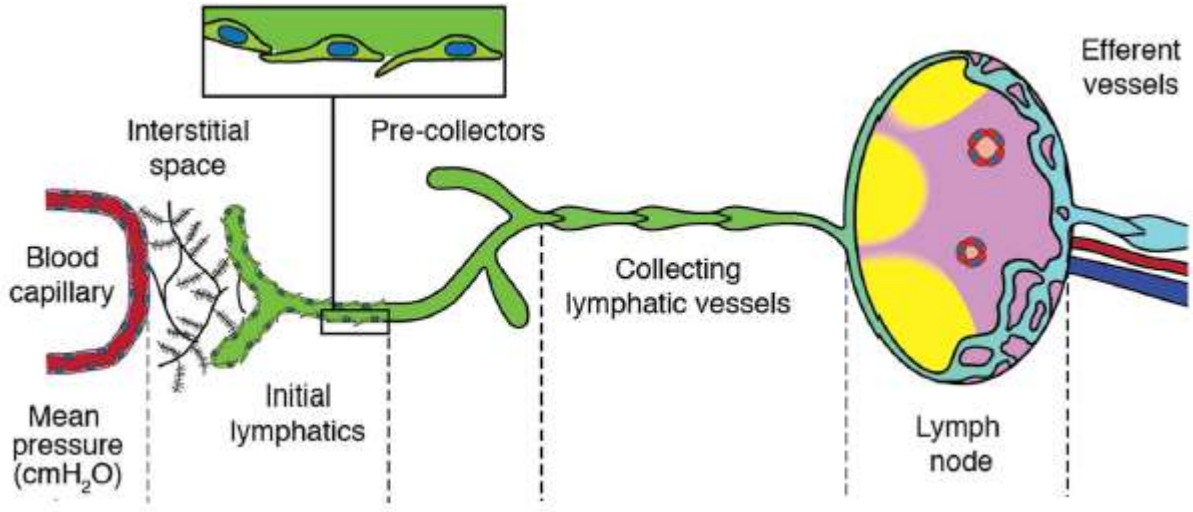

Figure 7.1: lymph flow pathways

Firstly, we modeled the component of the lymphatic system which provides the driving force for fluid motion, known as a lymphangion. To simulate its contractility, we introduced a lumped description based on the use of a time-varying elastance. Then, we tested different configurations to connect this compartment with the cardiovascular system through the interstitial space. By a physiological standpoint, this connection represents the long-standing physiological problem known as lymph formation.

We have shown how a combination of passive elements does not result in the expected physiological behavior. Specifically, we could not observe the subatmospheric pressure in the interstitial space. In contrast, introducing an electrical current source resulted in a subatmospheric pressure in the interstitial space. In this electric configuration, our simulation results are in agreement with the physiological expectation of the cardiovascular system. Concerning the lymphatic system, the simulated values agree with the few available pressure measurements obtained on the human lymphatic system. The proposed model suggests a tight relationship between interstitial fluid and initial lymphatic in the maintenance of a subatmospheric pressure in the interstitium. This observation was conjectured by a famous physiologist, Arthur Guyton. However, there is not, to the best of our knowledge, any quantitative demonstration of this physiological mechanism in the literature.

Based on the conclusions of the lumped parameter model, we hypothesized that a functional collaboration exists between the interstitial space and the contractile element of the lymphatic system, called lymphangion, in the overall fluid balance. To be able to quantitatively test this hypothesis, a deeper understanding of the mechanism of the lymphangion was needed, but its mechanisms still need to be elucidated. Hence, in the second part of the thesis, we investigated the fluid-dynamic behavior of the lymphangion, which is reported in Figure 7.2

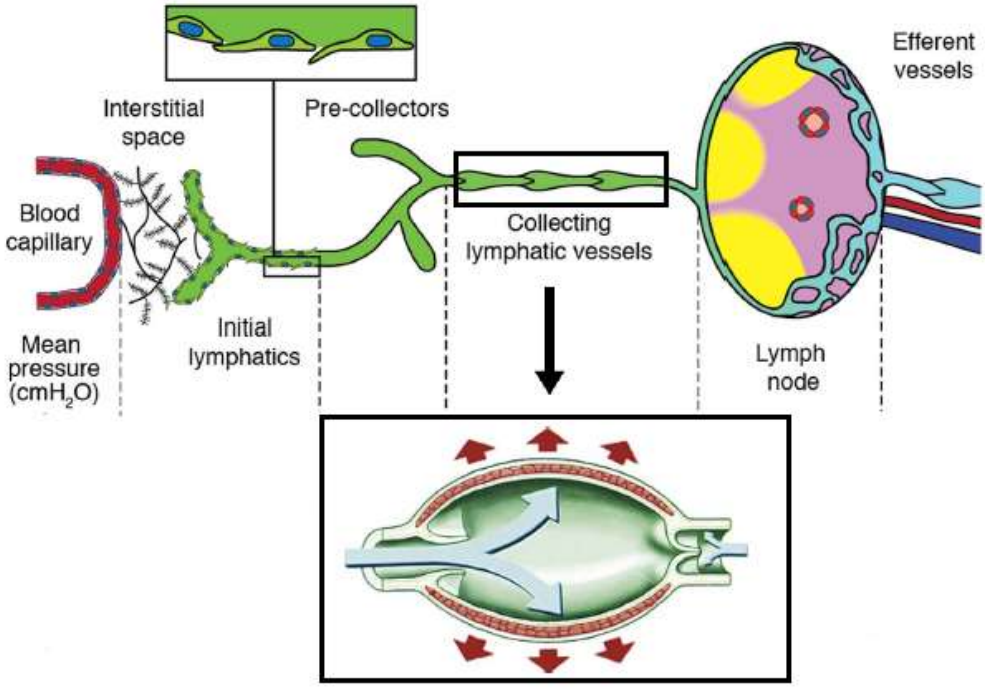

Figure 7.2:Lymphangion

Specifically, we developed a CFD simulation with the commercial software ***FLOW-3D.*** Our goal was to study the fluid-dynamic behavior of a lymphatic vessel at the local scale within a three-dimensional computational environment. To the best of our knowledge, the proposed distributed approach represents a novelty in the investigation of the lymphatic system. As a matter of fact, due to the lack of data and the complexity of the simulation, the lymphangion has been primarily studied with a lumped model.

Our CFD model was inspired and calibrated against the experimental results reported in the work of Jamalian and Davis [7]. Initially, we modeled a scenario comprising a single lymphangion. The proposed simulation enabled us to observe the spatial and temporal evolution of quantities of interests such as pressure and flow rate. The main finding of our model is how the time rate of change of pressure stems almost entirely from the pressure drop caused by valve. Based on the fluid-dynamic analysis, we further demonstrated how the dynamics of the valve is completely passive and depends on the motion of the lymphangions.

Then, we studied a more complex scenario characterized by five lymphangions connected in series. Based on the results from the first simulation, we formulated a modeling assumption describing valve dynamics. This assumption allowed us to optimize the simulation time without affecting the physiological behavior of the problem.

Once calibrated, our simulation proved to be able to reproduce the measured quantity in [7]. Moreover, our analysis allowed us to observe the interaction of a chain of lymphangions. Our model has demonstrated the presence of a favorable pressure gradient in the lymphangion chain throughout the entire contraction cycle. This favorable pressure gradient has a crucial importance not only regarding lymphangions dynamics but also in a systemic perspective. As a matter of fact, this gradient can be considered a quantitative demonstration of the so called “suction effect”, which is a possible mechanism explaining the way in which fluid could be drawn into the initial lymphatic from the interstitial space. Due to the fact that we coupled our modeling observation with a theoretical explanation, our results can be considered the first quantitative step towards understanding the mechanism of lymph formation.

The two modeling approaches developed in this thesis are a first step towards a deeper investigation of physiological mechanisms of the lymphatic system. The next step includes the definition of a constitutive equation of the electric elements of the lymphangions based on the fluid-dynamic behavior observed in the CFD simulations. Moreover, another interesting perspective is the coupling of the two computational approaches within a unique virtual laboratory. Another future direction of research involving the CFD model is the simulation of the transport of proteins in the lymphangions. The objective may be to verify how these element modify the fluid-dynamic regime of the lymphangion. In conclusion, the long term goal of this modeling project is to develop a virtual laboratory which can increase the overall knowledge of factors contributing to diseases of the lymphatic system. This task may result in more effective medical treatments to prevent the occurrence of these pathological conditions and to optimize their therapeutical treatment.

References

[1] Choi, I., Lee, S., "The New Era of the Lymphatic System: no Longer Secondary to the Blood Vascular System", *Cold Spring Harb Perspect Med 2012*.

[2] Cueni, L. N., Detmar, M., "The lymphatic System in Health and Disease" *Lymphatic Research and Biology, 2008*.

[3] Swartz, M. A., "The physiology of the lymphatic system", *Advanced Drug Delivery Reviews 50 (2001) 3 –20*.

[4] Scallan, J. P. *et al*, "Lymphatic pumping: mechanics, mechanisms and malfunction", *J Physiol 594.20 (2016) pp 5749–5768*.

[5] Unno, N. *et al.*, "A novel method of measuring human lymphatic pumping using indocyanine green fluorescence lymphography", *Journal of vascular surgery, Volume 52, number 4, 2010*.

[6] Bertram, C. D., "Contraction of collecting lymphatics: organization of pressure-dependent rate for multiple lymphangions", *Biomechanics and Modeling in Mechanobiology,2018*.

[7] Jamalian, S. *et al, "*Demonstration and analysis of the Suction Effect for Pumping Lymph from Tissue Beds at Subatmospheric Pressure*", Nature Scientific Reports, 7: 12080, 2017*.

[8] Zawieja, D. C., "Contractile Physiology of Lymphatics", *Lymphatic Research and Biology, Volume 7, Number 2, 2009*.

[9] Guyton, A. C., Hall J. E., " The microcirculation and the Lymphatic System: Capillary Fluid Exchange, Interstitial Fluid, and Lymph Flow" in *Textbook of Medical Physiology, 11th ed., 2006*.

[10] Scallan, J., Huxley V. H., Korthuis, R. J., "Fluid Movement Across the Endothelial Barrier" in: *Capillary Fluid Exchange, Morgan & Claypool life science, 2010*.

[11] Moore Jr, J. E., Bertram, C. D., " Lymphatic system Flows", *Annual Review of Fluid Mechanics, 2018*.

[12] Randolph, G. J., *et al* "The lymphatic System: Integral Roles in Immunity", *Annu. Rev. Immunol, 2017*.

[13] Hughes, T. J. R., " Derivation of the one-dimensional equations" in: *A study of the one-dimensional theory of arterial pulse propagation*, Report Number 74-13, 1974.

[14] Hughes, T, J, R., Lublinier, J., "On the One-Dimensional Theory of Blood Flow in the Larger Vessels", *Mathematical Biosciences 18, 161-170, 1973*.

[15] Formaggia, L., Quarteroni, A., Veneziani, "*Reduced models of the cardiovascular system*", in: Cardiovascular mathematics Modeling and simulation of the circulatory system, pp 347-394.

[16] Peterson, K., *et al* "Numerical Simulation of the influence of Gravity and Psture on Cardiac Performance", *Annals of Biomedical Engineering, 2002.*

[17] Avanzolini, P. *et al*, "Time-Varying Mechanical Properties of the Left Ventricle- A computer Simulation", *IEEE Transactions on biomedical Engineering, Volume 10, 1985.*

[18] Quick, C. M., *et al* "First-order approximation for the pressure-flow relationship of spontaneously contracting lymphangions", *American Journal of Physiology-Heart and Circulatory Physiology, 2008.*

[19] Westerhof, N., *et al* "The arterial Windkessel*", Medical & Biological Engineering & Computing, Springer*, 2008.

[20] Koarakianitis, T., Shi, Y., " A concentrated parameter model for the human cardiovascular system including heart valve and atrioventricular interaction", Medical Engineering & Physics,2006.

[21] Shi, Y. *et al,* "Review of Zero-D and 1-D Models of Blood Flow in the Cardiovascular system", *BioMedical Engineering OnLine,* 2011.

[22] Avanzolini, P. *et al*, "CADS Simulation of the closed-loop cardiovascular System", *Int J Biomedical Computation, 1988.*

[23] Margaris, K. N., Black, R. A., "Modelling the lymphatic system: challenges and opportunities", *J.R. Soc. Interface,* 2012.

[24] Braakman, R. *et al*, "A dynamic nonlinear lumped model for skeletal muscle circulation", *Annual Biomedical Engineering, 1989.*

[25] Fogliardi, R. *et al*, "Comparison of linear and nonlinear formulations of the three-element Windkessel model", *American Journal of Physiology, 1996.*

[26] Guyton, A. C., Hall J. E., "Vascular Distensibility and Functions of the Arterial and Venous Systems" in: *Textbook of Medical Physiology, 11th ed., 2006.*

[27] Lakin, W. D. *et al*, "A whole-body mathematical model for intracranial pressure dynamics", *J. Mathematical Biology, 2003.*

[28] Suga, H. *et al* "Load independence of the instantaneous pressure-volume ratio of the canine left ventricle and effects of epinephrine and heart rate on the ratio", *Circulation Research*, 1973.

[29] Segers, P. *et al*, " Systemic and pulmonary hemodynamics assessed with a lumped-parameter heart-arterial interaction model", *Journal of Engineering Mathematics, 2003.*

[30] Grodins, F. S., "Integrative Cardiovascular Physiology: A mathematical Synthesis of Cardiac and Biological Hemodynamics", *The Quarterly Review of Biology, Volume 34, Number 2, 1959.*

[31]Venugopal, A. M. *et al*, "Nonlinear lymphangion pressure–volume relationship minimizes edema", *American Journal of Physiology and Heart Circulatory Physiology, 2010*.

[32]Gajani, G. S. *et al,* "A lumped model of lymphatic system suitable for large scale simulations", *European Conference on Circuit Theory and Design (ECCTD), 2015*.

[33]Drake, R. E. *et al*, "Equivalent circuit technique for lymph flow studies", *American Journal of Physiology and Heart Circulatory Physiology, 1986*.

[34]Quick, C. M., "Intrinsic pump-conduit behavior of lymphatic vessels", *Am J Physiol Regul-Integr Comp Physiology*, 2007

[35] Scallan, J. P. *et al*, "Independent and interactive effects of preload and afterload on the pump function of the isolated lymphangion", *American Journal of Physiology-Heart and Circulatory Physiology* ,2012.

[36]Li, B. *et al*, "Pressure-volume relationships in sheep mesenteric lymphatic vessels in situ: response to hypovolemia",*Microvascular Research, Elsevier, 1998*.

[37]Venugopal, A. M. *et al*, "Nonlinear lymphangion pressure–volume relationship minimizes edema", *American Journal of Physiology-Heart and Circulatory Physiology* ,2010.

[38]Rajagopalan, S. *et al*, "Evaluating the time-varying elastance concept for lymphangions", *Engineering in Medicine and Biology Society, Proceedings of the 25th Annual International Conference of the IEEE, Volume:* 1*, 2003*.

[39]Davis, M. J. *et al*, "Intrinsic increase in lymphangion muscle contractility in response to elevated afterload", *American Journal of Physiology-Heart and Circulatory Physiology* ,2012.

[40]Aukland, K., Reed, R. K.," Interstitial-Lymphatic Mechanisms in the control of Extracellular Fluid Volume", *Physiological Reviews, American Physiological Society*, ,Volume 73, No. 1, 1993.

[41]Wiig, H., Swartz, M. A.,"Interstitial fluid and lymph formation and transport: Physiological regulation and roles in inflammation and cancer", *Physiological Reviews ,American Physiological Society, 2012*.

[42]Grodins, F. S., "Integrative Cardiovascular Physiology: A mathematical Synthesis of Cardiac and Biological Hemodynamics", *The Quarterly Review of Biology, Volume 34, Number 2, 1959*.

[43]Jamalian, S. et al,"Network Scale modeling of Lymph Transport and its effective Pumping Parameters", *PlosONE, 2016*.

[44]Bertram, C. D. *et al*, "Simulation of a Chain of Collapsible contracting Lymphangions with progressive valve closure", *Journal of Biomechanical Engineering, 2011*.

[45]Bertram, C. D. *et al*, "Consequences of intravascular lymphatic valve properties:a study of contraction timing in a multi-lymphangion model", *American Journal of Physiology-Heart and Circulatory Physiology* ,2010.

[46]Bertram, C. D. *et al*, "Contraction of collecting lymphatics: organization of pressure dependent rate for multiple lymphangions", *Biomechanics and Modeling in Mechanobiology* ,2018.

[46]Perfetti, R, "Circuiti del secondo ordine" in: *Circuiti elettrici , Zanichelli, 2012*.

[47]Arnold, D.N. *et al*, "Unified Analysis of Discontinuous Galerkin Methods for Elliptic Problems*" J. Numer. Anal, 2002*.

[48] ***FLOW-3D,*** User Manual, Version 11.

[49] Savin, V.J. et al, "Measurement of Albumin Reflection Coefficient with Isolated Rat Glomeruli", *J. Am. Soc. Nephrol*, 1992.